Effect of Red Blood Cell Morphology and Suspension Heterogeneity on Microcirculation Dynamics

Bendaoud Mohammed

Fachrichtung Physik
Universität des Saarlandes

Dissertation zur Erlangung des Grades des
Doktors der Naturwissenschaften der Naturwissenschaftlich-Technischen Fakultät der Universität des Saarlandes von

Universität des Saarlandes November 2025

Tag des Kolloquiums:	5. November 2025
Dekan:	Prof. Dr.-Ing. Dirk Bähre
Berichterstatter:	Prof. Dr. Christian Wagner
	Prof. Dr. Jochen Hub
Akad. Mitglied:	Dr. Carsten Alexander Baltes
Vorsitz:	Prof. Dr. Ralf Seemann

Science cannot solve the ultimate mystery of nature. And that is because, in the last analysis, we ourselves are a part of the mystery that we are trying to solve.

— **Max Planck**

To my beloved family—my mother, father, and sisters—whose unwavering support and love have been my guiding light through both the challenges and triumphs of this journey, and to Mr. Thami Elouzzani for his invaluable and unforgettable support, I express my deepest gratitude. And to my God, whose grace and guidance have been my stronghold in times of doubt and my beacon in moments of darkness. This thesis not only symbolizes my academic endeavors but also bears witness to the sacrifices, encouragement, faith, and boundless support you have all placed in me. To all those who have cared for me, believed in me, and stood by me, your presence in my life has been a source of strength and inspiration. May this work be a reflection of our collective hopes, dreams, aspirations, and the divine guidance that has led us here. Thank you for being my constant in a sea of change.

Declaration

I hereby declare that except where specific reference is made to the work of others, the contents of this dissertation are original and have not been submitted in whole or in part for consideration for any other degree or qualification in this, or any other university. This dissertation is my own work and contains nothing which is the outcome of work done in collaboration with others, except as specified in the text and Acknowledgements. This dissertation contains fewer than 18,000 words including bibliography, tables, and equations, and has fewer than 110 figures.

Erklärung

Hiermit erkläre ich, dass, soweit nicht ausdrücklich auf die Arbeiten anderer hingewiesen wird, der Inhalt dieser Dissertation eigenständig von mir verfasst wurde und weder vollständig noch teilweise für eine andere akademische Prüfung oder einen anderen Abschluss an dieser oder einer anderen Universität eingereicht wurde. Diese Dissertation ist meine eigene Arbeit und enthält nichts, was das Ergebnis einer Zusammenarbeit mit anderen ist, außer wie im Text und in den Danksagungen angegeben. Diese Dissertation umfasst weniger als 18.000 Wörter, einschließlich Bibliografie, Tabellen und Gleichungen, und enthält weniger als 110 Abbildungen.

Bendaoud Mohammed
November 2025

Acknowledgements

This thesis stands as a testament not only to my efforts but significantly to the invaluable contributions, support, and guidance of several key individuals and groups who have been integral to my journey and the completion of this work.

Foremost, I extend my deepest gratitude to my supervisor, **Prof. Dr. Christian Wagner**, for offering me the opportunity to be a part of his research group. His unwavering support, constant presence, and insightful feedback have been pivotal throughout my PhD journey, providing me with the encouragement and scientific rigor needed to navigate the complexities of my research. I am immensely grateful for his help and for the invaluable guidance he has always provided.

I am equally thankful to my supervisor, **Prof. Dr. Chaoqui Misbah**, whose expertise and guidance have been indispensable. His perspectives and advice have greatly enriched my understanding and approach to our shared field of study, enhancing the quality and depth of my work.

A special acknowledgment goes to **Prof. Dr. Hamid Zahraoui**, who was instrumental in initiating my scientific journey. His belief in my potential and his support at the outset of this path have been fundamental to where I stand today. He opened the door to this world of inquiry and discovery, for which I am forever grateful.

I am also deeply grateful to **Dr. Alexis Darras** for his constant willingness to engage in scientific discussions and for his invaluable guidance and support.

Also wish to express my sincere appreciation to all my colleagues in the **AG Wagner** group at Saarland University, Germany, and the **Eccel team** at LIPhy in Grenoble, France. The collaborative environment, the exchange of ideas, and the camaraderie we shared have been a source of motivation and joy. This journey would have been markedly different without your support, friendship, and the many moments of shared scientific passion.

The path to completing this thesis has been one of growth, challenge, and discovery. To everyone who has been a part of this journey—thank you. Your contributions, in myriad forms, have been the scaffolding that supported the construction of this work.

Abstract

The morphology and microcirculatory behavior of the red blood cell represent a dynamic interplay that essentially underlies the pathophysiology of various blood disorders. The abnormal shapes, as seen in spherocytosis and ellipsocytosis, affect RBC deformability significantly and, hence, the capacity to pass through narrow capillaries. This can lead to reduced blood flow and subsequent tissue ischemia, culminating in organ dysfunction. Numerical simulations using the Lattice-Boltzmann Method are conducted in the present work to explore how changes in RBC shapes-from healthy bi-concave shapes to spherocytes-affect the flow properties, such as flow rate, cell-free layer dynamics, and hydrodynamic diffusion. Non-trivial non-monotonic behaviors in flow rate versus asphericity are unveiled, which depend on channel width and point out optimal shapes for given geometries. We further discuss the consequences of heterogeneity within RBC suspension and show that the variation in concentration of abnormal shapes is crucially important to determine blood viscosity and flow dynamics. Interestingly, as few as 15% to 20% of spherocytes can reduce RBC flux by about 50% while doubling blood viscosity, whereas other abnormal shapes have relatively weaker effects. We also discuss the phenomenon of the "memory" of RBCs, proposing that their previous mechanical interactions determine their subsequent behavior and distribution, particularly at points of bifurcation, where lingering and partitioning happen.

Zusammenfassung

Die Morphologie und das mikrozirkulatorische Verhalten der roten Blutkörperchen stellen ein dynamisches Zusammenspiel dar, das im Wesentlichen der Pathophysiologie verschiedener Bluterkrankungen zugrunde liegt. Die abnormen Zellformen, wie sie bei Sphärozytose und Elliptozytose auftreten, beeinträchtigen die Verformbarkeit der roten Blutkörperchen erheblich und damit auch ihre Fähigkeit, enge Kapillaren zu passieren. Dies kann zu einer verminderten Durchblutung und nachfolgender Gewebeischämie führen, was schließlich eine Organfunktionsstörung zur Folge haben kann. In der vorliegenden Arbeit werden numerische Simulationen unter Verwendung der Lattice-Boltzmann-Methode durchgeführt, um zu untersuchen, wie Formveränderungen der roten Blutkörperchen – von gesunden bikonkaven Formen hin zu Sphärozyten – die Strömungseigenschaften wie Durchflussrate, Dynamik der zellfreien Schicht und hydrodynamische Diffusion beeinflussen. Dabei werden nicht-triviale, nicht-monotone Verhaltensweisen der Durchflussrate in Abhängigkeit von der Asphärizität aufgedeckt, die von der Kanalbreite abhängen und auf optimale Zellformen für bestimmte Geometrien hinweisen. Darüber hinaus werden die Auswirkungen von Heterogenität innerhalb einer Suspension roter Blutkörperchen diskutiert und gezeigt, dass die Konzentrationsvariation abnormaler Zellformen entscheidend für die Bestimmung der Blutviskosität und der Strömungsdynamik ist. Interessanterweise können bereits 15% bis 20% Sphärozyten den Fluss roter Blutkörperchen um etwa 50% reduzieren und gleichzeitig die Blutviskosität verdoppeln, während andere abnorme Zellformen vergleichsweise schwächere Effekte aufweisen. Zudem wird das Phänomen des „Gedächtnisses“ roter Blutkörperchen diskutiert: Frühere mechanische Wechselwirkungen bestimmen ihr späteres Verhalten und ihre Verteilung, insbesondere an Verzweigungspunkten, an denen Verweilen und Aufteilung auftreten.

Liste of publications

- **M. Bendaoud, M. Abbasi, A. Darras, H. Ez-Zahraouy, C. Wagner, and C. Misbah**
  Blood flow efficiency in response to red blood cell sphericity. *Physical Review Fluids*, **9**(5), 053603 (2024).

- **Y. Rashidi, G. Simionato, Q. Zhou, T. John, A. Kihm, M. Bendaoud, T. Krüger, M. O. Bernabeu, L. Kaestner, M. W. Laschke, M. D. Menger, C. Wagner, and A. Darras**
  Red blood cell lingering modulates hematocrit distribution in the microcirculation. *Biophysical Journal*, **122**(8), 1526–1537.

- **M. Bendaoud, A. Darras, H. Ez-Zahraouy, C. Wagner, and C. Misbah**
  The Effect of Heterogeneous Red Blood Cell Suspension on Blood Flow in Spherocytosis. *Submitted to Physical Review Fluids.*

- **M. Bendaoud, A. Darras, Y. Rashidi, C. Wagner, and C. Misbah**
  Red Blood Cells sphericity and network architecture influence lingering and partitioning. *Submitted to Biophysical Journal.*

- **M. Bendaoud, A. Darras, H. Ez-Zahraouy, C. Wagner, and C. Misbah**
  Red Blood Cell Adhesion and Its Influence on Capillary Flow in the In Vivo Microvasculature. *In preparation.*

Table of contents

List of figures

List of tables

Chapter 1

Introduction

Erythrocytes or red blood cells (RBCs) are a vital element in the realization of oxygen supply to tissues, carbon dioxide withdrawal, and play an important role in the implementation of some biochemical signaling. The microcirculation system facilitates the exchange of gases, nutrients, and waste through a small, complex network of blood vessels. This ability depends on the distinctive morphology of RBCs. The shape, elasticity, and deformability of red cells are important determinants of blood flow and oxygen distribution throughout the body. These physical characteristics do not allow an immediate return to their steady state upon alteration. An imbalance within the system can easily be set off. A proper form of red blood cells enables normal blood flow to the small blood vessels in the body organs; consequently, such diseases as anemia result from improper shapes of these cell types. Red blood cells with altered shape, from common diseases such as anemia to complex pathological states like sickle cell disease, all have significant burdens and affect millions of people worldwide.

1.1 Red blood cell in Microcirculation

1.1.1 A Brief introduction about Blood

Blood is among the most significant fluids in the human body and helps to keep the survival of life itself. Blood comprises about 7-8% of total body weight, and sustains life by keeping homeostasis [39].

Composition of Blood: Blood is highly specialized bodily fluid having characteristic composition. The structure consists of plasma and blood cells. Figure 1.1 shows a general view of how blood looks after centrifuging. Plasma is the liquid part of blood,

constituting circa 55% of volume of blood. It mostly comprises 90% of water in which various dissolved substances are found, like proteins, glucose, mineral ions, hormones, carbon dioxide, and the blood cells themselves [5]. The cellular elements of blood, constituting around 45% of the blood volume, include erythrocytes (red blood cells), leukocytes (white blood cells), and thrombocytes (platelets).

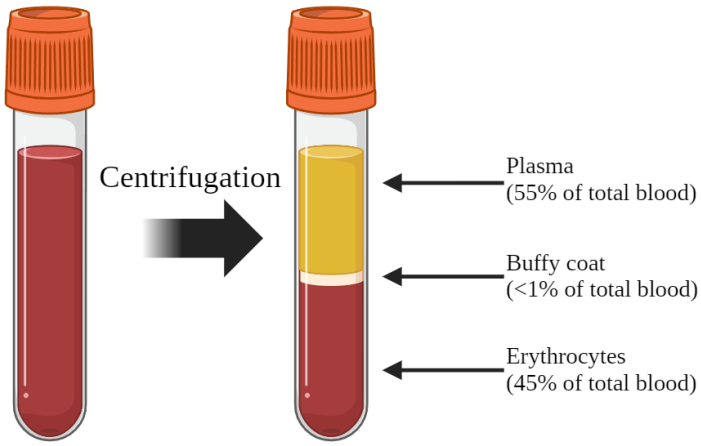

Fig. 1.1 Human blood composition after centrifugation.

- **Erythrocytes (Red Blood Cells):** The cells are biconcave in shape that increases surface area for the exchange of gases oxygen and carbon dioxide. A protein in the erythrocyte cells called Hemoglobin bonds with oxygen and makes the blood red in color [79].
- **Leukocytes (White Blood Cells):** These cells are part of the immune system and are divided into two main types (Fig 1.2): granulocytes (neutrophils, eosinophils, and basophils) and agranulocytes (lymphocytes and monocytes). Each type plays a specific role in protecting the body against infections and diseases [73].
- **Thrombocytes (Platelets):** Tiny blood platelets of disc-shaped cell fragments that play a vital role in blood clotting. They stick together at the injury site of a blood vessel, allowing blood to clot and stop flowing out from the body.

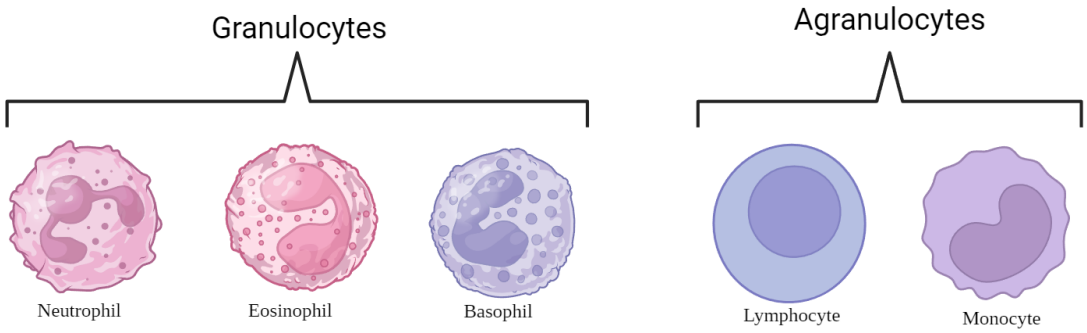

Fig. 1.2 Human white blood cell types.

1.1.2 A Brief Introduction about Red blood cells

The discovery and understanding of RBCs have developed dramatically over time. The very first noted observation of RBCs is attributed to the Dutch scientist Antonie van Leeuwenhoek in the late 17th century, as a result of him using his newly constructed microscope (Fig. 1.3). However, the crucial nature of RBCs in oxygen transport was not known until the circulatory system theory was developed by William Harvey in the 17th century and when hemoglobin was discovered by Felix Hoppe-Seyler in the 19th century.

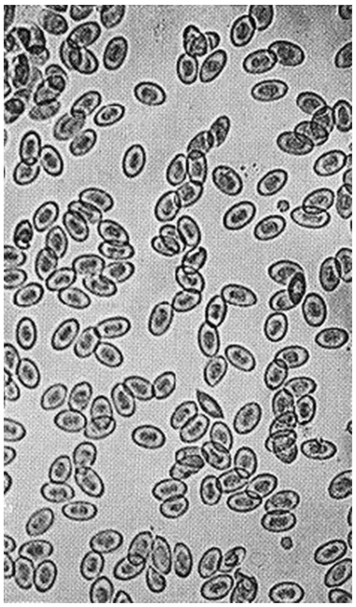

Fig. 1.3 First recorded observation of Erythrocytes in a fish's blood by Van Leeuwenhoek [118].

The chief function of RBCs is to transport oxygen from the lungs to the body tissues and carbon dioxide back from the tissues to the lungs. They can do this because of the presence of hemoglobin, which will bind oxygen in the lungs and will release it in the peripheral tissue capillaries. Hemoglobin's affinity with oxygen is affected by things like pH and levels of carbon dioxide, which leads to the efficient delivery of oxygen and removal of carbon dioxide. In addition to gas exchange, RBCs function in contributing to the body's acid-base balance and as indicators in some diseases. Abnormalities in the number, morphology, or function of RBCs reflect a large group of disorders, from anemia to sickle cell disease [43].

Lifecycle and Erythropoiesis: The primary site of RBC production is the bone marrow. Erythrocytes are produced by a process known as erythropoiesis. Stem cells in the bone marrow differentiate into erythroblasts, which then mature into erythrocytes. During this process, the nucleus and organelles are expelled, which is an adaptive design allowing more room for hemoglobin within the cell [102]. Mature RBCs live about 120 days before they undergo phagocytosis and breakdown by macrophages in the spleen, liver, and bone marrow. Hemoglobin iron is recycled and heme group is converted to bilirubin, which excretes in the bile and participates in the determination of fecal color [59].

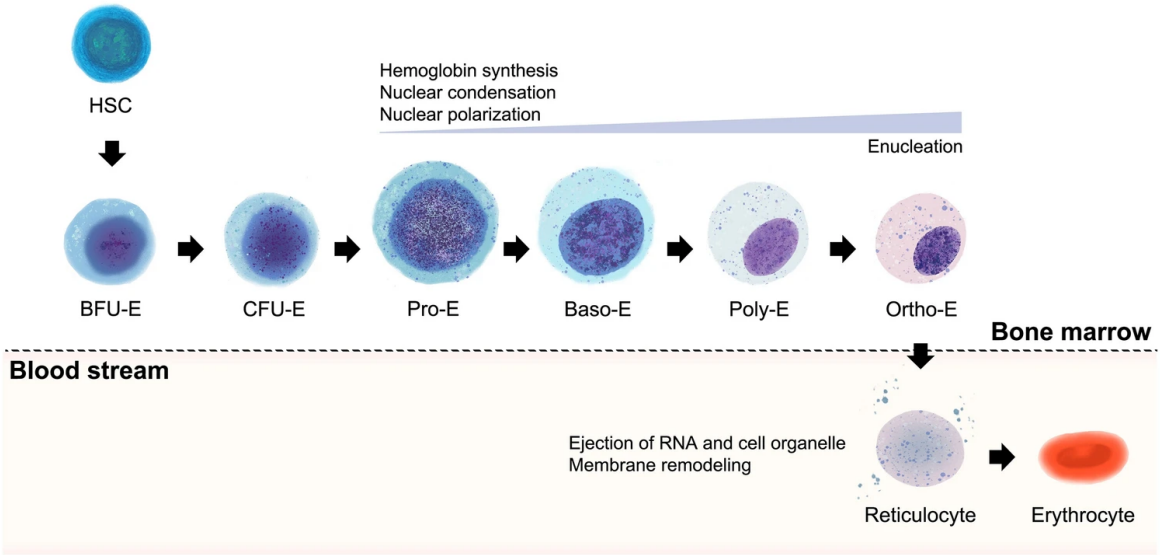

Fig. 1.4 An overview of erythropoiesis, starting from the hematopoietic stem cell (HSC) and ending with the red blood cell [41].

Gas Exchange and Regulation: Gas exchange is the primary function of RBCs and is controlled in an extremely tight way to meet the fluctuating oxygen demands of the body. Hemoglobin's affinity for oxygen is modulated by several factors including pH, CO_2 partial pressure, temperature, and 2,3-BPG (2,3-bisphosphoglycerate). The Bohr effect describes the phenomenon in which a decrease in pH (or increase in CO_2) reduces hemoglobin's affinity for oxygen, thus facilitating oxygen release in highly metabolically active tissues. This is opposed in the lungs, wherein pH is higher and concentration of CO_2 is much lower; hence hemoglobin's oxygen affinity increases to bind oxygen.

RBC membrane : The RBC membrane is composed mainly of a lipid bilayer with integral and peripheral proteins (see figure 1.5), demonstrating remarkable flexibility and durability [84]. Important proteins in the membrane, such as spectrin, band 3, and glycophorins, contribute to the cell's shape and its stability and proper function in terms of oxygen transport [33]. The other important determinant of fluidity and permeability properties is the lipid composition of the membrane: its phospholipids and cholesterol [7].

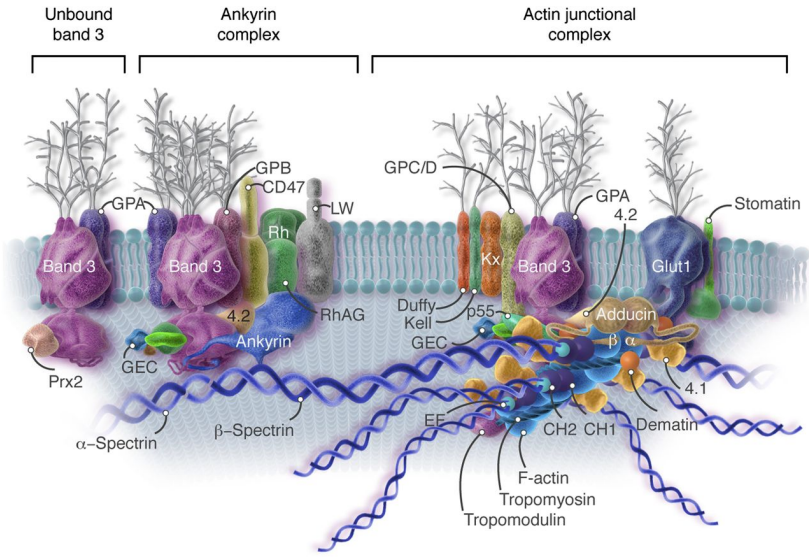

Fig. 1.5 Red blood cell membrane skeleton[76].

1.1.3 A Brief Introduction about Microcirculation

Microcirculation is blood circulation in the smallest blood vessels of organ systems and includes the arterioles, capillaries, and venules. The microcirculatory network is very intricate and created to have the most efficient exchange. It is through arterioles, small

branches of arteries, which lead into the beds of capillaries where the exchange with tissue fluid occurs; blood is then collected by venules coalescing into veins. Capillaries are the most numerous and thinnest of the blood vessels; each consists of a single layer of endothelial cells to allow for rapid diffusion of oxygen, carbon dioxide, nutrients, and metabolic wastes [35]. Otherwise, the start of any knowledge of circulation of blood and microcirculation was from the ancient Greeks through the existence of Alcmaeon of Croton, who postulated that blood vessels are part of the vascular system. This notion was, in fact, the very basis of curiosity and led to many new breakthroughs over the following centuries. By far, his works have been exemplary, with the work on pulmonary circulation in the 13th century by the Arab physician Ibn al-Nafis being a pioneer one [56]. The great shift occurred with the work of William Harvey in the 17th century: "Exercitatio Anatomica de Motu Cordis et Sanguinis in Animalibus," in which he described for the first time the fact that the heart worked like a pump for the circulation of the blood and was part of the enclosed system [42]. Later advances in 1661, particularly by Marcello Malpighi, who microscopically studied capillaries, arterioles, and venules in the broadest sense [77], set the stage for the contemporary era where research would be carried out to understand how exchange of nutrient supply and blood flow control within the microcirculation, among other functions, contribute to health and diseases. Subsequent improvements over methods of microscopy and imaging techniques, during the 19th and 20th centuries, have again expanded our knowledge about microcirculation (Fig. 1.6). It was a period that was characterized by elaborations on the dynamics of blood flow, the governing regulatory mechanisms of the microcirculation, and finally, the functions of the endothelium were found.

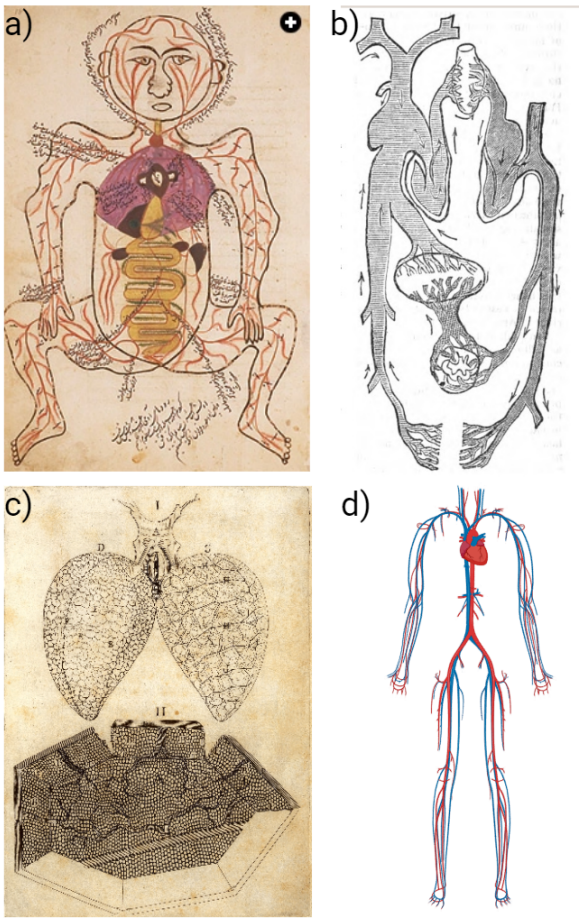

Fig. 1.6 Evolution of Blood Circulation Through Time. a) The Pulmonary Circulation by Ibn al-Nafis (13th-century). b) The blood circulation as demonstrated by Harvey (1600s). c) Microanatomy and the capillary circulation of the frog's lungs by Malpighi (1661), d) Modern approach of the human circulatory system (20th-century).

1.2 Importance of red blood cell morphology in blood flow dynamics

Shape and size in RBCs are important for their function [18]. RBCs, in a normal or healthy individual, are usually biconcave disks that help them to carry oxygen around the body. Meanwhile, many of the studies deal with certain abnormalities in the morphology of RBCs, such as spherocytes, elliptocytosis, schistocytes, and stomatocytes.

Spherocytosis is a hereditary condition in which spherocytes are found in the blood. These are RBCs of more spherical shape than normal RBCs. Owing to their abnormal

shape, they are more predisposed to destruction in the spleen, leading to hemolysis and anemia. Typically, spherocytes are associated with hereditary spherocytosis, an inherited hemolytic disorder, as a result of membrane protein defects such as spectrin or ankyrin.

Another hereditary condition, elliptocytosis, produces the same general effect on RBCs but results in the cells being flattened and ovoid instead of spherical. Elliptocytosis is considered to be rarer than spherocytosis. Abnormalities that distort the shape of erythrocytes typically result from genetic mutations. Known mutations affect proteins such as spectrin or band 4.1 [21].

Schistocytes are RBCs that possess irregular or rough outlines, as shown in Figure 1.7. The presence of schistocytes can be due to a number of causes, including microangiopathic hemolytic anemia, disseminated intravascular coagulation, and thrombotic thrombocytopenic purpura [103].

Stomatocytes (Fig. 1.7) possess a mouth-shaped central pallor and are related to hereditary stomatocytosis, a disorder in membrane lipid composition, and alterations in ion channel activity. These changes affect erythrocyte hydration and deformability [32].

Knizocytes are seen in spur cells, which are the presence of spicules or projections in their surface. They are considered the hallmark of spur cell hemolytic anemia and usually are associated with liver disease and abnormalities in membrane lipid composition [69].

Mushroom-shaped cells are an unusual morphological abnormality characterized by a central protrusion or bulge, reminiscent of a mushroom cap. These cells have typically been associated with other disarray in erythrocytes: congenital dyserthropoietic anemias, hereditary spherocytosis with Band-3 protein deficiency, disseminated intravascular coagulation, hemolytic-uremic syndrome, thrombotic thrombocytopenic purpura, renal disease, microangiopathic hemolytic anemia, erythroleukemia, and occasionally oxidative drug-induced hemolysis [23].

Acanthocytes (Fig. 1.7) which are sometimes also called spur cells, do have irregularly spaced, short, and blunt projections on the surface. This morphology is typical in the context of different diseases, such as neuroacanthocytosis syndromes and abetalipoproteinemia [45].

Dacrocytes (teardrop cells) are abnormal, teardrop-shaped erythrocytes typically observed in myelofibrosis—one of the diseases characterized by a fibrous substitution of bone marrow [101].

Echinocytes (Fig. 1.7) are red cells with many small, regularly spaced projections that give the cell a sea-urchin appearance. Many conditions and exposures, such as uremia, as well as some drugs, will lead to this morphology [31].

Heinz bodies (Fig. 1.7) are abnormal inclusions in erythrocytes and are formed by denatured hemoglobin that has precipitated on the inside surface of the cell membrane. They are often formed due to oxidative stress or during exposure to certain drugs, chemicals, or unstable hemoglobin variants. A common factor leading to Heinz body formation is G6PD deficiency [108].

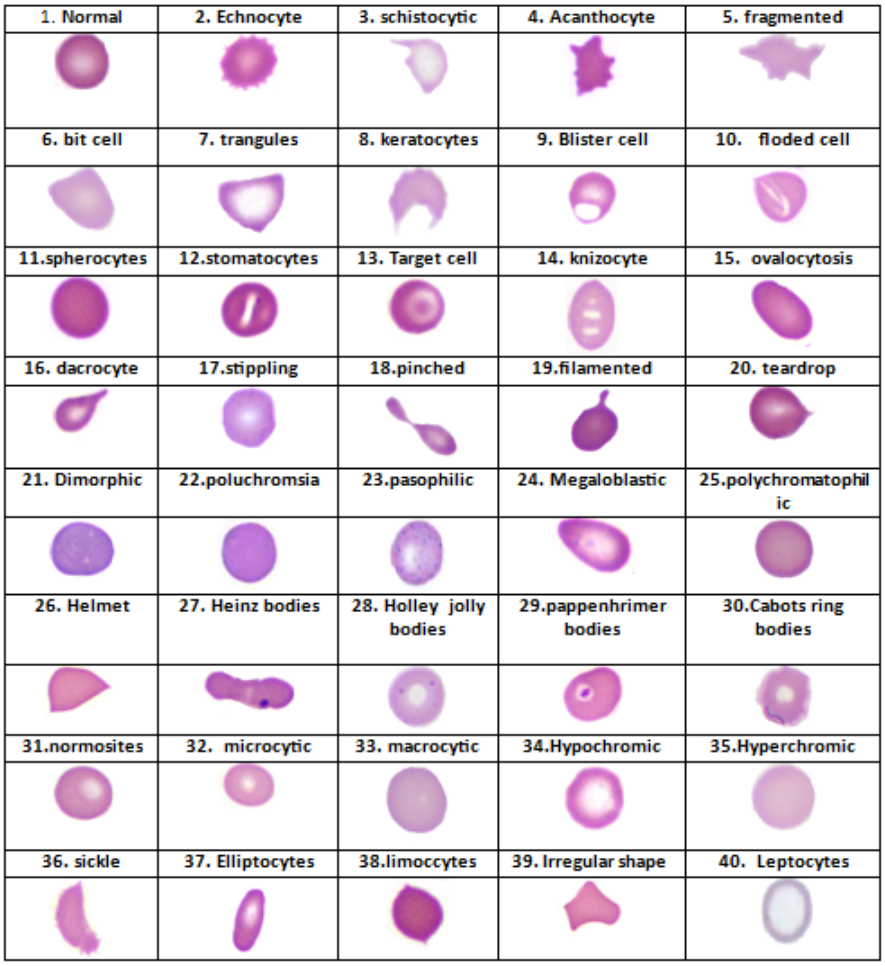

Fig. 1.7 Common abnormal shapes of erythrocytes [3]

Other than morphological abnormalities, other RBC abnormalities that can also be related to the oxygen carrying capability [13] include crenation. This is when the RBCs are exposed in an environment in which they experience a hypotonic kind of solution, which is normally a sign of dehydration or kidney disease. At that point, water gets

into the RBCs, which will make them swell and become more spherical. Apart from crenation, which is caused by exposure to hypotonic environments, RBCs can also be affected by exposure to hypertonic environments [36]. Hypertonicity is when the concentration of solutes of the extracellular fluid is higher than the concentration of the cell's intracellular. This can have the effect of causing the RBCs to lose water and thus shrink; the process is termed plasmolysis [6]. As such, in a hypertonic solution, RBCs may lose water and become dehydrated, taking a more flattened shape.

A large number of pathological conditions—acquired and inherited in nature, such as hemolytic anemias, infections, autoimmune or genetic disorders, and even intoxications of drug or chemical origin—stand responsible for these abnormalities in RBC morphology. In fact, the observed morphological changes in RBC can serve not only for detecting certain pathological conditions but also as a tool for recognizing the underlying mechanisms of a specific disease [117].

The RBCs are generally highly deformable, thereby essentially contributing to blood flow, especially in microcirculation [85, 18, 104, 81]. In fact, researchers studying binary suspensions have observed segregation very similar to blood flow in confined shear flow. Smaller and stiffer particles tend to localize towards the walls, whereas larger and flexible ones exhibit antimargination - that is, localization of particles near the center. Such effects are driven by size-dependent migration and rigidity-dependent collisions [67]. There exists to date a large body of literature on the experimental and numerical studies of the shapes of healthy RBCs[19, 20, 4, 122, 89, 119, 47, 46, 25, 110, 98, 37, 86, 62, 97, 27, 28, 80, 82, 2, 88, 99]. However, the effect of cell shape (e.g. like in spherocytosis and ellipsocytosis) on blood flow rheology remains a largely unexplored research area.

One of the aims of the thesis is to establish the effect of aberrations in RBCs morphologies on the flow properties. We will take a look at quite a few channel widths, and shapes and we will analyze systematically the flow properties for different hematocrits. This indicates quite a subtle behavior of flow rate as a function of the asphericity. For example, it is observed that for certain values of channel width, a biconcave shape ensures the maximum transport of RBCs, while for some other channel width, the considerably larger proportion of inflated cells prevails—or at least flows at a similar rate compared with the usual biconcave shape. We shall present in a systematic way this sort of behavior and then provide some basic key elements to understand its origin. In this sense, our study reveals some very fundamental aspects of the flow of suspension soft deformable objects in confinement.

1.3 Heterogeneous suspension in blood

Blood is a heterogeneous suspension of mainly RBCs, white blood cells, platelets, and plasma. The physiological function of RBCs critically depends on their morphology with respect to shape and size. Under usual conditions, RBCs assume a biconcave discoid shape, which optimizes its large deformation in the transportation of oxygen throughout the body. However, their shape can deviate from this normal morphology, which is critical for this type of cell [76].

Among all disorders of the red blood cells, there is one that is in the center of our attention: spherocytosis. In this disorder, the cells are deformed and look like a sphere. Sometimes, 15-20% of all red blood cells can be of the spherocyte type in the peripheral blood smear of the spherocytosis patients [40]. The values for the number of irregularly contracted RBCs, the so-called pyknocytes and schistocytes, in the studies of Marsh[38] turned out to be very different when comparing healthy adults and infants. For the former, their corresponding values are no more than 0.1%, while in normal full-term infants, the corresponding percentage values vary between 0.3% and 1.9%. More importantly, these values are even higher in premature infants; up to 5.6% of blood cells are represented as pyknocytes or schistocytes. Irregularly contracted cells like these mimic spherocytes by area loss, but are of variable shape and many have characteristic protrusions, in part related to the presence of Heinz bodies [8].

In addition to the normal forms of variation in RBC morphology, important considerations are hereditary spherocytosis (HS). Based on these, HS has been reported to occur in approximately 1 in 5,000 neonates in North Europe and 1 in 2,000 in North America [75], whereas HS is the most common hereditary hemolytic anemia in Japan [120]. Although few epidemiologic reports have been obtained from China on HS, many related reports are available. For instance, the condition reportedly accounts for 31.5% of the 356 cases of hereditary hemolytic disease that have occurred [71].

Spherocytes are particularly vulnerable to destruction compared to their normally shaped counterpart. As a result, spherocytosis can lead to complications such as splenomegaly and anemia. Splenectomy, which can be described as the surgical removal of the spleen, is a common therapeutic intervention in cases of excessive destruction of spherocytic RBCs, ultimately aiming to improve anemia and related symptoms [16]. There is a found proportion of about 20% spherocytes, which affects the flow properties. The flux of RBCs declines by about 50%. Effective viscosity increases also by about 50%, with oxygen transport being considerably more impeded.

Our study deals with fluid-structure interactions of the RBCs, elucidating the impact of their morphological diversity on blood suspensions. We quantify the RBC

morphologies with numerical simulations of spherical RBCs to describe the details of these irregularities that affect blood flux, viscosity, and cellular interactions.

1.4 Contribution of the thesis

1.4.1 Blood Flow Efficiency in Response to Red Blood Cell Sphericity

The morphological properties of red blood cells, such as size and shape, play a crucial role in determining their flow properties. A typical abnormal shape can be found in the blood disorders, such as spherocytosis, ellipsocytosis, etc., where the cells have a sphere-like or ellipse-like appearance, instead of being bi-concave. These shape anomalies can affect the ability of RBCs to deform and squeeze through narrow capillaries, leading to reduced blood flow and oxygen supply to tissues. This can cause tissue ischemia, which can lead to organ damage and dysfunction. We conduct numerical simulations in order to study the flow properties (such as flow rate, cell-free-layer, and RBCs hydrodynamic diffusion) by varying the shapes of the cells in a wide range of shapes, from a bi-concave one (healthy RBCs) to a spherical one, representing RBCs suffering from spherocytosis disease. Our study highlights nontrivial effects, such as a non monotonic behaviors of the flow rate as a function of asphericity, depending on the channel width. For example, for some channel width the usual bi-concave shape is revealed to be optimal with respect to flow rate, whereas for other widths more inflated shapes are more efficient. This offers an interesting basis for the understanding of the mechanisms underlying blood flow deficiencies associated with shape anomalies, and may help evaluating the potential therapeutic strategies that might be used to alleviate the symptoms. As RBCs also serve as a classical model system for very deformable objects, our study reveals also some fundamental aspects of the flow of soft suspensions.

1.4.2 Effects of Heterogeneous Red Blood Cell Suspension on flow dynamics

In several diseases (like spherocytosis and ellipsocytosis) a more or less large proportion of red blood cells have an abnormal form (a sphere-like or ellipse-like shape), instead of having a biconcave shape. These shape anomalies can impair blood flow, and thus oxygen transport. This study investigates the impact of heterogeneous RBCs morphologies (cells having different shapes) in a blood suspension on blood flow

transport. A two dimensional model is adopted, and the evolution equations are solved by means of a Lattice-Boltzmann method. When circular cells were introduced (with a certain proportion) into the mixture, a significant reduction in blood flux was observed, indicating diminished oxygen transport capacity, particularly relevant to spherocytosis. A remarkable finding, and a priori counter-intuitive, is the non monotonic behavior of the RBC flux as a function of spherocytes proportion. A systematic analysis is undertaken by exploring several relevant parameters (like hematocrit, channel width, flow strength...). The analysis of viscosity in heterogeneous RBC mixtures revealed significantly heightened effective viscosity, notably intensified in the presence of spherical RBCs. The results are interpreted in terms of cell-free layer, margination of spherocytes by discocytes, and of cell-cell interactions. These findings advance our understanding of RBC morphology's role in blood flow dynamics and its relevance to conditions such as spherocytosis and elliptocytosis.

1.4.3 Decoding Red Blood Cell Dynamics: How Sphericity and Network Architecture Drive Microvascular Partitioning and Lingering

The transport and distribution of red blood cells through microvascular networks is central to diverse applications in drug delivery, tissue engineering, and the study of pathological mechanisms. Recent findings highlight two critical, yet often overlooked, phenomena: (*i*) a "memory effect," wherein the RBC partitioning at each bifurcation is influenced by events at previous bifurcations, and (*ii*) RBC lingering at the bifurcation apex, which strongly affects downstream flow distribution. However, the interplay between network geometry, RBC sphericity, and these emergent behaviors remains insufficiently explored. Here, we perform two-dimensional Lattice Boltzmann simulations coupled with an immersed boundary model to systematically investigate RBC dynamics in both asymmetric and fully symmetric network designs. Our results show that RBC "memory" grows progressively with each bifurcation, leading to increasing deviations from classical partitioning laws regardless of the network's geometric complexity. We further demonstrate that even near-spherical RBCs can experience substantial lingering due to cumulative apex interactions—challenging the notion that only elongated or pathologically deformed cells are prone to these effects. Collectively, these findings underscore how RBC deformability and prior apex encounters conspire to shape microcirculatory flow, providing a unified framework that explains why pathological RBC shapes may exacerbate transport inefficiencies in the microvasculature.

1.4.4 Hysteresis of a Single vesicle in a confined Poiseuille flow

This study examines the dynamics of a single RBC in confined Poiseuille flow, driven by a pressure gradient between two parallel plates, enabling analysis of factors like capillary number (reflecting the balance between viscous forces and membrane elasticity) and channel width, which impacts confinement. Previous research has shown varied RBC shapes and migrations based on flow parameters. Through numerical simulations, we explore how these factors affect RBC shape, position, and blood viscosity, investigating bifurcation phenomena, initial conditions, and hysteresis in RBC stability and behavior.

Chapter 2

The numerical method and the Red blood cell modeling

The mathematical model [54, 83, 105, 53] and numerical method of the code which we used in our study that was developed in our research group, have been described and validated in prior works, the validation involved also a comparison with the boundary integral method [48, 107, 64, 106, 65, 50]. For the sake of completeness, we present a summary in this chapter.

2.1 Background of The Lattice Boltzmann Method and The Immersed Boundary Method

The Lattice Boltzmann Method (LBM) has proven, over the last decade or so, a very powerful numerical tool for the simulations of fluid flows, including Stokes flow, mostly because it is easily implemented and quite efficient, even for complex systems and geometries. Basic microscopic models and mesoscopic kinetic equations facilitate an approach with which microscopic interactions can be included in macroscopic flow behavior [111].

The fundamental equation of LBM, the discrete Boltzmann equation, in the context of the Bhatnagar-Gross-Krook (BGK) [60] approximation for collisional processes, is given by:

$$f_i(\mathbf{x} + \mathbf{c}_i\Delta t, t + \Delta t) - f_i(\mathbf{x}, t) = -\frac{\Delta t}{\tau}\left[f_i(\mathbf{x}, t) - f_i^{eq}(\mathbf{x}, t)\right] \tag{2.1}$$

Here, $f_i(\mathbf{x}, t)$ is the distribution function of particles moving with velocity $\mathbf{c}_i$ at position $\mathbf{x}$ and time t, f_i^{eq} is the equilibrium distribution function, τ is the relaxation time,

and Δt is the time step. The equilibrium distribution function for Stokes flow can be approximated as:

$$f_i^{eq} = w_i \rho \left[1 + \frac{\mathbf{c}_i \cdot \mathbf{u}}{c_s^2} + \frac{(\mathbf{c}_i \cdot \mathbf{u})^2}{2c_s^4} - \frac{\mathbf{u}^2}{2c_s^2} \right] \tag{2.2}$$

where w_i are the weights associated with each velocity direction in the lattice model, and c_s is the speed of sound in the lattice, typically $c_s = \frac{1}{\sqrt{3}}$ in lattice units.

In 2D simulations, the D2Q9 and D2Q5 lattice models are commonly employed [72]. For example, the D2Q9 model considers nine discrete velocity directions, including rest, four cardinal, and four diagonal directions (Fig. 2.1). The discrete velocities $\mathbf{c}_i$, and weights,w_i , are specifically chosen to ensure isotropy and to match the macroscopic equations through Chapman-Enskog expansion [72].

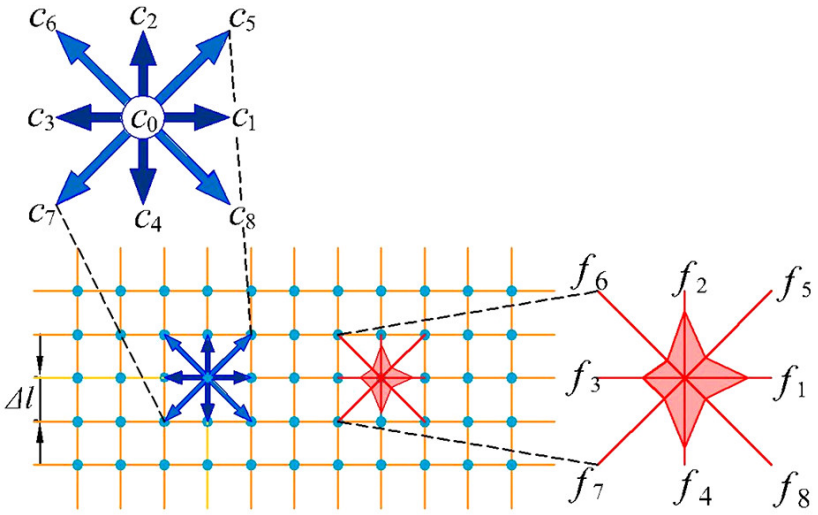

Fig. 2.1 Schematics of Space and velocity discretization in D2Q9 model [17].

In the other hand, The immersed boundary method (IBM) is also a computational approach used to simulate fluid-structure interactions, particularly in complex geometries. Developed initially by Charles Peskin in the 1970s to model blood flow in the heart [90], the method has since been applied to a wide range of problems in fluid dynamics and beyond. The immersed boundary method treats the fluid and immersed structures within it in a unified computational framework. The fluid dynamics are described by the Navier-Stokes equations, while the deformations and motions of the immersed boundaries (RBCs in our case) are captured by additional force terms. Our models equations are solved using the Lattice Boltzmann Method, combined with the immersed boundary method[65, 107, 61].

2.2 The Vesicle model

Fig. 2.2 depicts RBCs immersed in a straight tube filled with a fluid mimicking plasma. We employ a 2D model for computational efficiency while maintaining the effectiveness of our model. Indeed, despite the reductionist nature of the 2D vesicle model, several analyses utilizing more sophisticated 3D models that incorporate the membrane cytoskeleton suggest that the simplified 2D vesicle model successfully captures several pivotal erythrocyte shapes and flow behaviors (like RBCs flow as a function of hematocrit)[115, 26, 95, 24, 1].

In Fig. 2.2, L and W are the channel length and width. The cell membranes are represented by symbol G, while the fluid domain is separated into Ω_{in} (inside the cells) and Ω_{ex} (outside the cells designating the "plasmic" domain). Red blood cells coordinates are given by $\mathbf{X}(s)$, where s is the curvilinear coordinate (in 2D) along the cell membrane, with $s \in [0,\ P]$, where P is the cell perimeter.

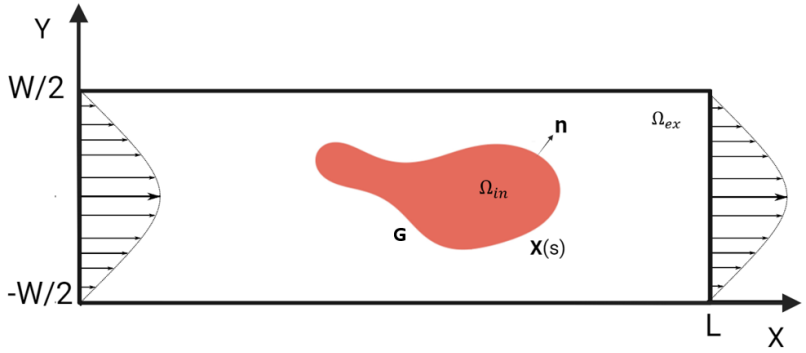

Fig. 2.2 A schematic representation of the straight channel configuration is presented, wherein Red Blood Cell is suspended in a straight channel filled with plasma. The channel dimensions are denoted by L and W, which correspond to the length and width, respectively. The fluid domains within and outside the channel are referred to as Ω_{in} and Ω_{ex}, respectively. The normal vector, denoted by $\mathbf{n}$, is directed outward, and the cell membrane is represented by the symbol G.

Under flow, the cell resists against deformation due to its membrane rigidity and inextensibility (in 2D). The corresponding bending energy (known as the Helfrich energy [44]) is given by:

$$\mathbf{H}(\mathbf{X}(s)) = \frac{\kappa}{2}\int_G c^2\, ds + \int_G \zeta\, ds, \tag{2.3}$$

where κ is the bending rigidity modulus, c is the local curvature and ζ is a Lagrange multiplier which enforces local membrane inextensibility. This energy leads to a

restoring force (its expression is given below) on the membrane that is function of local curvature c and its derivatives.

2.3 Flow Model

The flow is considered as a Stokes flow, which is often referred to creeping flow, occurs in fluid dynamics when inertial forces are negligible compared to viscous forces. This scenario is typical at very low Reynolds numbers, $Re \ll 1$ (Table2.1), where $Re = \frac{\rho U L}{\mu}$, with ρ representing the fluid density, U the characteristic velocity, L the characteristic length, and μ the dynamic viscosity of the fluid.

Table 2.1 Diameter, mean velocity, and the corresponding Reynolds number in arterioles, venules, and capillaries [92].

Arterioles		
Diameter (μm)	Mean velocity (mm/s)	Re
60	12	0.2
15	7	0.03
Venules		
Diameter (μm)	Mean velocity (mm/s)	Re
72	2.4	0.05
18	0.2	0.001
Capillaries		
Diameter (μm)	Mean velocity (mm/s)	Re
5	0.2	0.0003

The fluid inside and outside the cells obey the Navier-Stokes:

$$\begin{aligned} &\rho\left(\frac{\partial \mathbf{u}}{\partial t} + \mathbf{u}\cdot\nabla\mathbf{u}\right) = -\nabla p + \nabla\cdot\left[\mu\left(\nabla\mathbf{u} + \nabla\mathbf{u}^T\right)\right] + \mathbf{f}, \\ &\nabla\cdot\mathbf{u} = 0, \end{aligned} \tag{2.4}$$

Here, μ is the dynamic viscosity, and $\mathbf{f}$ is the force applied by the cell to the fluid. This force is obtained upon a functional derivative of the Helfrich energy and is given by [51]:

$$\mathbf{f} = \kappa\left(\frac{\partial^2 c}{\partial s^2} + \frac{1}{2}c^3 - \zeta c\right)\mathbf{n} + \frac{\partial \zeta}{\partial s}\mathbf{t}, \tag{2.5}$$

Here $\mathbf{n}$ and $\mathbf{t}$ are the normal and tangential unit vectors respectively to the membrane, while $\mu(x)$ is the dynamic viscosity and has two unique values within and outside the vesicle:

$$\mu(\mathbf{x}) = \begin{cases} \mu_{\text{in}} & \text{if } \mathbf{x} \in \Omega_{in} \\ \mu_{ex} & \text{if } \mathbf{x} \in \Omega_{ex} \end{cases} \tag{2.6}$$

The suspension is subjected to a pressure gradient. This pressure gradient results in an undisturbed (i.e. in the absence of RBCs) Poiseuille flow $\mathbf{u}(u,\ v)$,and is given by

$$\begin{aligned} u &= u_{\max}\left(1 - \frac{4y^2}{W^2}\right), \\ v &= 0, \end{aligned} \tag{2.7}$$

where u_{max} is the maximal velocity at the center of the channel at $y = 0$.

The LBM introduces naturally an inertial effect. However, the value of Reynolds number is typitally 10^{-4} (see typical velocity in microcirculation in Table 2.1), corresponding to a Stokes regime. This value is numerically too prohibitive (due to excessive computational time). Fortunately, several benchmarks have been established in the literature to identify a maximum value of Re below which the lattice-Boltzmann approach reproduces the Stokes regime with high precision. For the Stokes regime, there is general agreement that a value $Re = 0.1$ is a suitable balance between numerical efficiency and precision[121, 107, 113, 63, 48]. As a result, the Reynolds number in our simulation is set at a maximum of 0.1.

2.4 Dimensionless numbers

The dimensionless numbers are the key in characterizing vesicle behavior in flow and the interaction of these vesicles with the surrounding fluid. They yield insight into relative magnitudes of various physical forces and properties, and thus allow the comparison of different systems and conditions. Specifically for the simulation of RBCs in the context of microfluidic and microvascular environments, several important dimensionless numbers include the Capillary number, Viscosity ratio, Reduced area, and Confinement.

- The capillary number is defined as the ratio of shear force to bending force, we use it to characterize the deformation and dynamics of vesicles under flow:

$$Ca = \frac{\mu_{ex}\dot{\gamma_w}}{\kappa} R_0^3, \tag{2.8}$$

where $\dot{\gamma_w} = \partial u_x/\partial y|_{y=-W/2}$ is the shear rate at the wall, $y = -W/2$, and R_0 is a characteristic radius of RBC.

- The degree of confinement represents the ratio of the characteristic diameter of the vesicle to the characteristic width of the channel or vessel through which it is flowing, it helps to see the effects of narrow geometries on vesicle behavior and is defined as:

$$Cn = \frac{2R_0}{W} \tag{2.9}$$

- The viscosity contrast is the ratio between the viscosities of the internal and external fluids, the Viscosity contrast affects the tank-treading, tumbling, and swinging modes of vesicle motion under shear flow [86]. High viscosity contrast can lead to more rigid vesicle behavior, while low viscosity contrast favors fluid-like behavior and deformation.

$$\lambda = \frac{\mu_{int}}{\mu_{ext}} \tag{2.10}$$

- The reduced area (in 2D) is corresponding to the degree of cell inflation (or asphericity, see figure 2.3) . It influences the vesicle's buckling and transition between different dynamical states underflow.

$$\tau = \frac{4\pi A}{P^2} \tag{2.11}$$

where P is the perimeter and A is the enclosed area of the cell. A healthy RBC has a reduced volume lying in the range 0.6 to 0.64. A RBC with a reduced volume of 1 corresponds to a sphere, close to a spherocyte. We will consider various reduced areas representative of several abnormal shapes such as those found, for example, in spherocytosis and elliptocytosis.

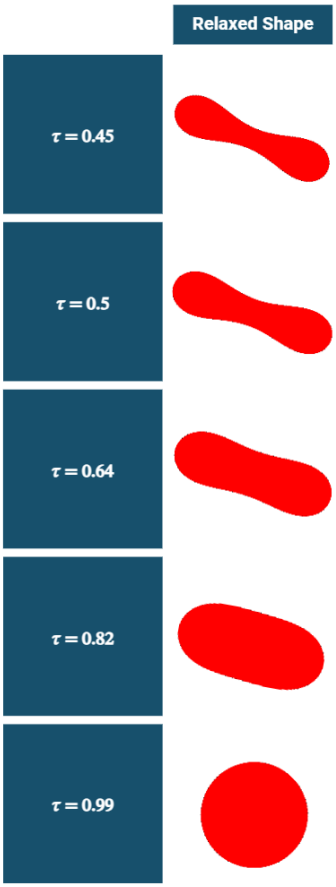

Fig. 2.3 2D visualization of the relaxed shape of RBC for different reduced area values.

All typical values of physical parameters used in this study and the values of dimensionless parameters are given in table 2.2.

Table 2.2 The simulation's physical and dimensionless parameters.

Physical Parameters	
Cell Radius R_0 (μm)	2.7 - 3
Bending modulus κ (J)	3×10^{-19}
Density ρ (Kg/m^3)	10^3
Plasma viscosity μ_{ex} $(Pa.s)$	10^{-3}
Dimensionless parameters	
Reynolds Number Re	0.1
Capillary number Ca	From 0.2 to 25
Viscosity contrast λ	From 1 to 20
Reduced Area τ	From 0.45 to 0.99

From the full suspension flux (flux of cells and the fluid) we can also extract the effective viscosity. It is defined as

$$\mu_{eff} = \frac{\mu_{ex} Q}{Q_{ssp}}, \tag{2.12}$$

where Q_{ssp} is the average flux of cell suspension, and Q is the flux of the pure plasma (with viscosity μ_{ex}) when subjected to the same pressure gradient.

More precisely the blood volumetric flow rate ratio Q is calculated directly from the velocity:

$$Q(t) = \int_{\Gamma} (\mathbf{u}, \mathbf{n}) dy \tag{2.13}$$

Where: Γ is a segment having length W and is perpendicular to the flow direction.

The flow rate in the absence of cells is calculated as :

$$Q_0 = \frac{2}{3} W u_{\max} \tag{2.14}$$

The RBCs flow is calculated using the following equation:

$$Q_c = \frac{N_{\mathrm{RBC}}}{T} A, \tag{2.15}$$

where N_{RBC} is the number of RBCs that cross the chosen section and T is the total time of the simulation.

Chapter 3

Blood Flow Efficiency in Response to Red Blood Cell Sphericity

Parts of this work are published in the *Physical Review Fluids* journal under DOI: https://doi.org/10.1103/PhysRevFluids.9.053603.

3.1 Introduction

The morphological properties of red blood cells, such as size and shape, play a crucial role in determining their flow properties. A typical abnormal shape can be found in the blood disorders, such as spherocytosis, ellipsocytosis, etc., where the cells have a sphere-like or ellipse-like appearance, instead of being bi-concave. These shape anomalies can affect the ability of RBCs to deform and squeeze through narrow capillaries, leading to reduced blood flow and oxygen supply to tissues. This can cause tissue ischemia, which can lead to organ damage and dysfunction. We conduct numerical simulations in order to study the flow properties (such as flow rate, cell-free-layer, and RBCs hydrodynamic diffusion) by varying the shapes of the cells in a wide range of shapes, from a bi-concave one (healthy RBCs) to a spherical one, representing RBCs suffering from spherocytosis disease. In this section, we will highlight nontrivial effects, such as a non monotonic behaviors of the flow rate as a function of asphericity, depending on the channel width. For example, for some channel width, the usual bi-concave shape is revealed to be optimal with respect to flow rate, whereas for other widths more inflated shapes are more efficient. This offers an interesting basis for the understanding of the mechanisms underlying blood flow deficiencies associated with shape anomalies, and may help evaluating the potential therapeutic strategies that might be used to alleviate

the symptoms. As RBCs also serve as a classical model system for very deformable objects, our study reveals also some fundamental aspects of the flow of soft suspensions.

3.2 Results and discussion

In the current study, we will explore values from 0.45 to 0.99 for the reduced area, the latter range corresponds to that found for red blood cells suffering spherocytosis. we explored different channel widths from 10μm to 40μm (Where table 3.1 shows the maximum flow velocity, in the absence of cells for different channel widths, i.e. different confinement Cn), and we will analyse the cell flux across the flow direction as a function of (i) hematocrit, (ii) channel width, and (iii) reduced area. We will consider homogeneous suspensions, where each cell has the same given reduced area.

Table 3.1 Maximum flow velocity in the absence of cells in the channel center for different widths for $Ca = 18$ and its corresponding confinement.

Width	$W = 10\mu$m	$W = 20\mu$m	$W = 40\mu$m
Maximum Velocity (mm/s)	0.68	1.37	2.74
Confinement Cn	0.54	0.27	0.14

3.2.1 Red blood cells with fixed area

The change in area or volume of RBCs, due to diseases discussed above, will impact the reduced volume (in 3D) or reduced area (in 2D). Since our simulations concern 2D, we will explore different reduced areas, by first modifying the perimeter and fixing the enclosed area, and exploring the reverse situation in the next section.

RBCs flux for different channel widths and different reduced area

In this section, our primary objective is to examine the impact of reduced area (by exploring different channel widths and hematocrits) on the flow properties of RBCs. We will first focus on the flux of RBCs.

Our findings, as illustrated in Figs.3.1-3.4, show the intricate interplay between channel width and reduced area on blood flux optimization. Notably, those figures reveal that the attainment of the maximum blood flux is dependent on both the width of the channel and the specific reduced area value of the RBCs in question. For instance, our simulation data indicates that the highest blood flux is achieved at a reduced area of 0.82 when the channel width is maintained at 10 µm as shown in Fig.3.1. A reduced

area of 0.64 is associated with optimal blood flux in channels with a width of 20 µm as shown in Fig.3.2, while a reduced area of 0.45 is found to be optimal in channels with a width of 40 µm as shown in Fig.3.3. These observations highlight the nuanced relationship between channel dimensions and RBC morphology.

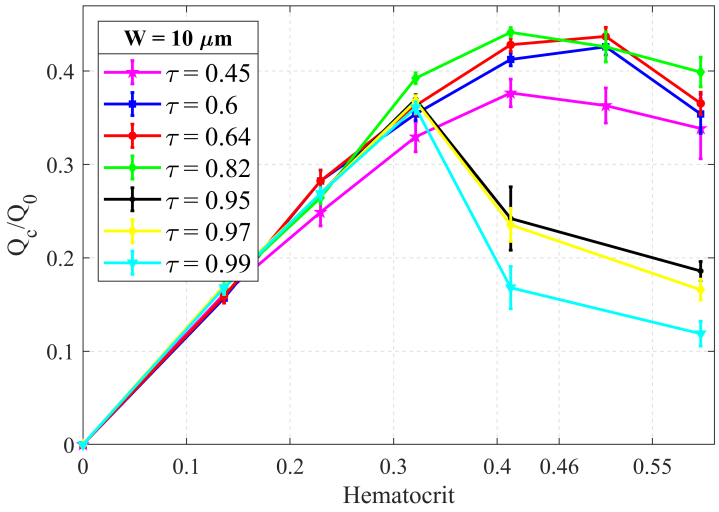

Fig. 3.1 Flux versus hematocrit for different reduced areas in a 10 µm ($Cn = 0.54$) channel width (RBCs with fixed area): A graphical representation of the relationship between flux and hematocrit for five distinct reduced areas (0.45 - 0.99). The total volume fraction ranges from 0 to 0.55, with a constant $Ca = 18$.

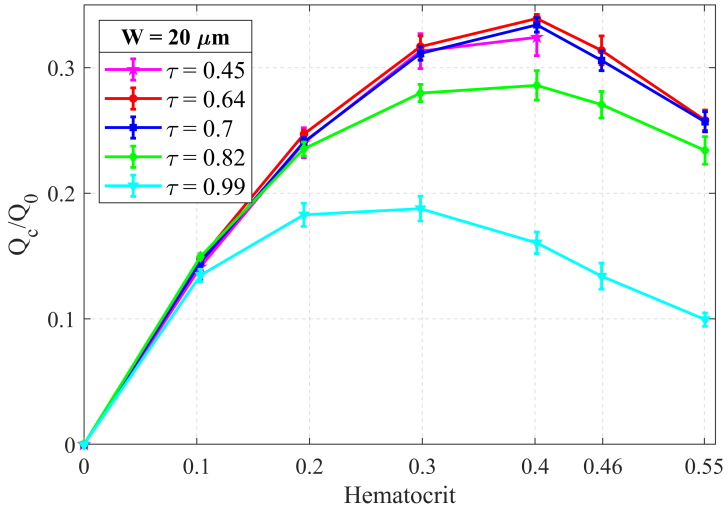

Fig. 3.2 Flux versus hematocrit for different reduced areas in a 20 µm ($Cn = 0.27$) channel width (RBCs with fixed area): A graphical representation of the relationship between flux and hematocrit for five distinct reduced areas (0.45, 0.64, 0.7, 0.82, and 0.99). The total volume fraction ranges from 0 to 0.55, with a constant $Ca = 18$.

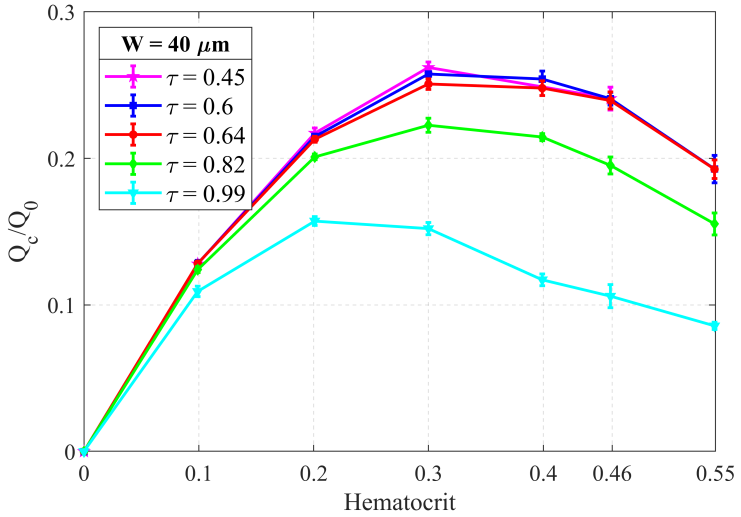

Fig. 3.3 Flux versus hematocrit for different reduced areas in a 40 µm ($Cn = 0.14$) channel width (RBCs with fixed area): A graphical representation of the relationship between flux and hematocrit for five distinct reduced areas (0.45, 0.6, 0.64, 0.82, and 0.99). The total volume fraction ranges from 0 to 0.55, with a constant $Ca = 18$.

Some remarks are in order. As shown, for example, in Fig. 3.1, while the reduced area 0.82 seems to provide a higher flux than other reduced area, the differences in

fluxes for reduced area 0.82, 0.64 and 0.6 are relatively small. We have repeated the simulation several times in order to rule out numerical errors, but the flux for reduced area 0.82 was always larger. Our results clearly show that in the case of spherocytosis (reduce area close to one; light blue line in Fig.3.1, Fig3.2, Fig3.3) there is an important collapse of RBCs flux: the RBC flux is reduced by 25% up to about 50% in comparison to the flux in healthy conditions. When the reduced area is very high, indicating that RBCs are nearly spherical, they may not deform adequately to navigate narrow channels efficiently (As an example in Fig.3.1 we see the same trend for the higher reduced areas 0.95, 0.97 and 0.99). This results in increased resistance and a decrease in blood flux. Indeed, a key message of this work is to elucidate the reasons behind the reduced blood flux in the case of spherical cells. We have explained this phenomenon in the next two subsections by illustrating the considerable thinning of the cell-free layer and the significantly higher dispersion of spherical cells. These factors contribute to heightened resistance in the plasma flow, consequently leading to a lower cellular flux.

The interplay between reduced area (τ) and channel width (see Fig.3.4) can be seen as follows. RBCs traversing channels of varying widths have different abilities to deform. For example, for a channel width of 10 µm, even if a RBC with reduced area 0.64 (or smaller) can deform more amply than a more inflated cell, its parachute (or slipper) shape confers to it a large enough transverse section, comparable (or even larger) to that of a RBC with reduced area 0.82, so that its resistance to flow is significant (see top 3 panels in Fig.3.5). This makes the cell with a large enough reduced area slightly more efficient (Fig.3.1). Conversely, for a larger width (say W=40 µm) cells with a small reduced area can elongate along the flow, reducing thus the flow resistance (see 3 bottom panels in Fig.3.5). This is why a cell with a small enough reduced area becomes favorable (see Fig.3.3).

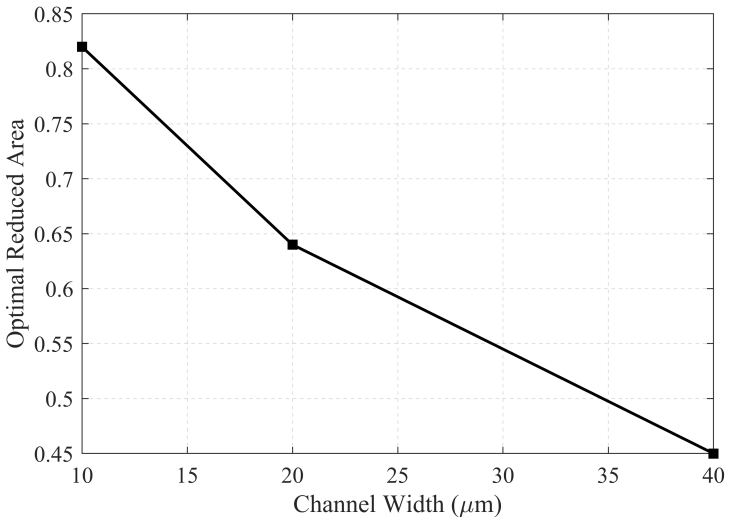

Fig. 3.4 Optimal reduced area of RBCs for maximum flow rate versus channel Width: This figure illustrates the optimal reduced area of red blood cells (RBCs) where the highest flow rate is achieved (see corresponding figures of flux, Figs.3.1,3.2 and 3.3) a function of the channel width (RBCs with fixed area).

When RBCs flow through narrow channels, they must deform to fit within the confines of the channel. This deformation is influenced by the cell's reduced area. The correlation between reduced area and blood flux emerges because there is an optimal degree of RBC deformation for efficient flow. This optimal deformation depends on the channel width. When the reduced area is too high (i.e., RBCs are nearly spherical), they may not deform enough to navigate narrow channels efficiently, leading to increased resistance and reduced blood flux. Conversely, when the reduced area is too low (i.e., RBCs are highly irregular in shape), they may experience excessive deformation in wider channels, also increasing resistance. There exists thus an optimal reduced area value for efficient flow, varying with channel width, whereby RBCs balance deformation and resistance.

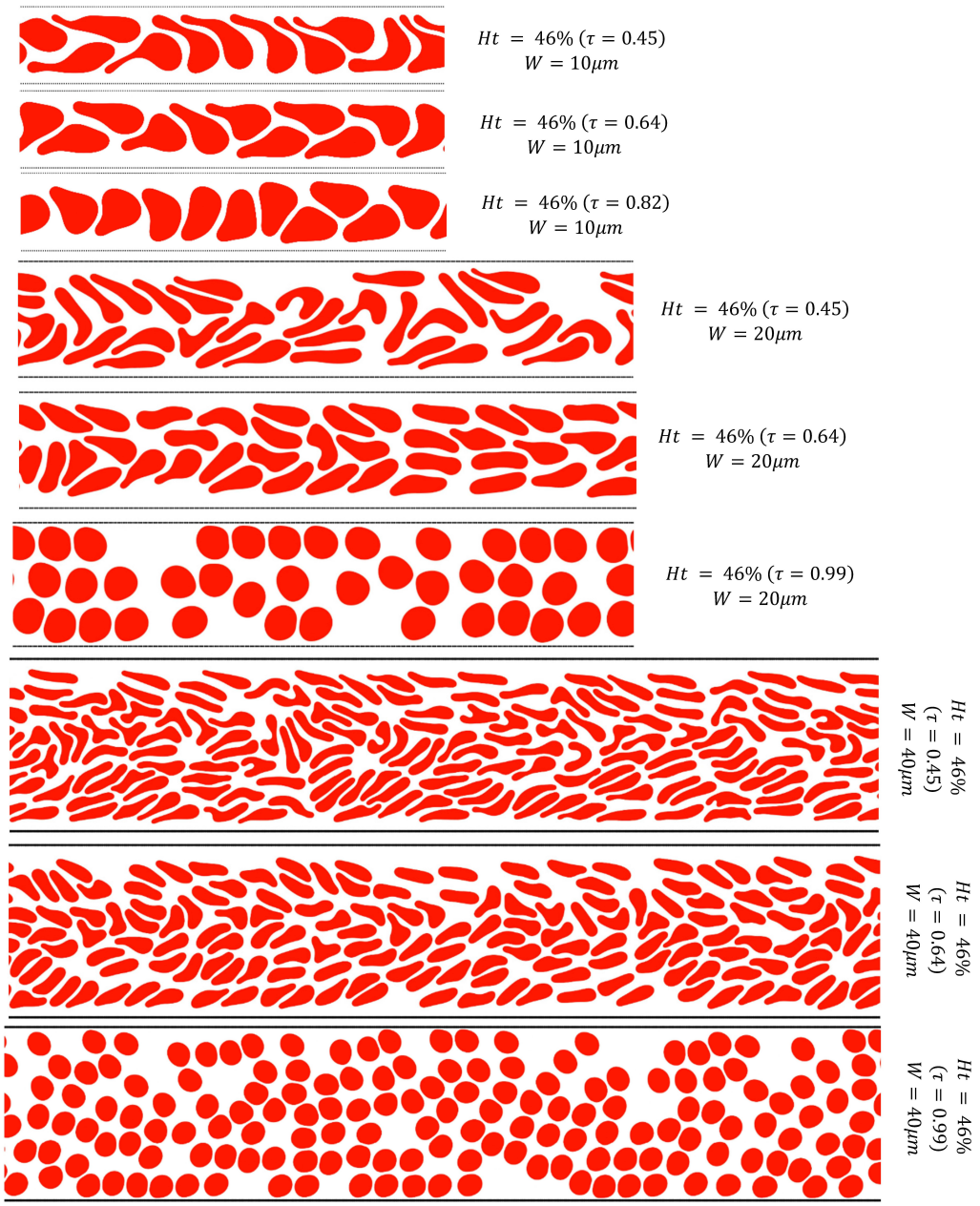

Fig. 3.5 Cells configurations for different selected channel widths and for different reduced areas.

Cell Free Layer (CFL)

The cell-free layer, often referred to as the "plasma layer" or "cell-depleted layer", is a crucial component in the microcirculation of blood vessels. This narrow, clear zone that lines the interior of blood vessels, particularly in small capillaries and arterioles, is devoid of blood cells and primarily consists of plasma. The presence of this cell-free

layer is a result of the hydrodynamic interactions between flowing blood cells and the hydrodyminc leift due to vessel wall. It plays a pivotal role in maintaining efficient blood flow by reducing frictional forces between the blood and the vessel wall[96, 100].

A thicker CFL appears to serve as a flow buffer, reducing resistance and allowing for more efficient blood flow. In this scenario, RBCs experience less impediment as they move through the vessel, leading to increased flow rates. Conversely, thinner CFL elevates flow resistance, impairing the fluid dynamics and causing a decrease in blood flow, which explains the dramatic decrease in blood flow for spherical cells for all studied channel widths [24].

In Fig.3.7, we present the probability density function (PDF) depicting the spatial distribution of RBCs for varying Reduced area values (we calculate the spatial distribution of red blood cells based on their entire cell body, rather than focusing solely on the cell center to be more accurate). To put things in perspective, we consider the case W=20 µm for which the maximum flux is obtained for $\tau = 0.64$ (see Fig.3.2). Our observations reveal a noteworthy trend: as the reduced area decreases, the size of CFL expands, leading to enhanced blood flux. This phenomenon stems from the principle that a larger CFL equates to reduced resistance within the microchannel, thereby facilitating a more efficient blood flow. In larger CFLs, RBCs experience less hindrance and are afforded greater freedom to migrate closer to the channel's center, particularly where there is the higher flow velocities. We present, in figure 3.6, the velocity profile in the presence of cells, revealing a flattened shape due to accumulation of cells in the channel center.

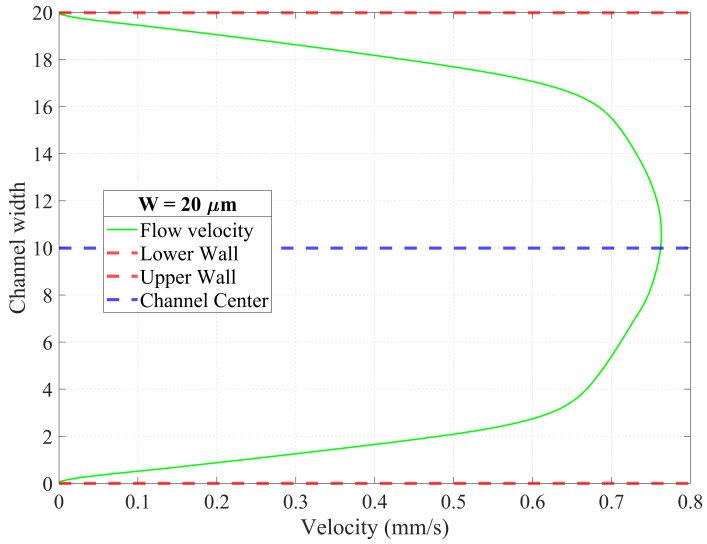

Fig. 3.6 Velocity profile in 20μm channel width, Capillary number 18, in presence of cells for a hematocrit of 40%

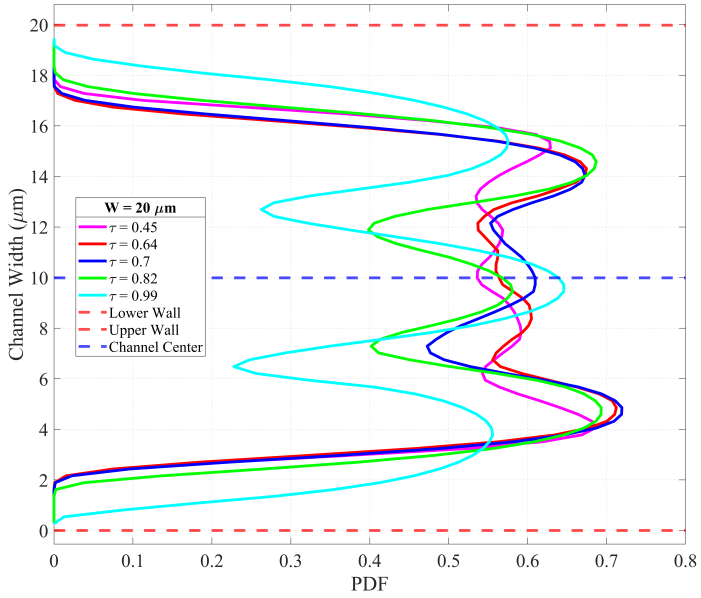

(a) Spatial Distribution of Red Blood Cells for different reduced area values

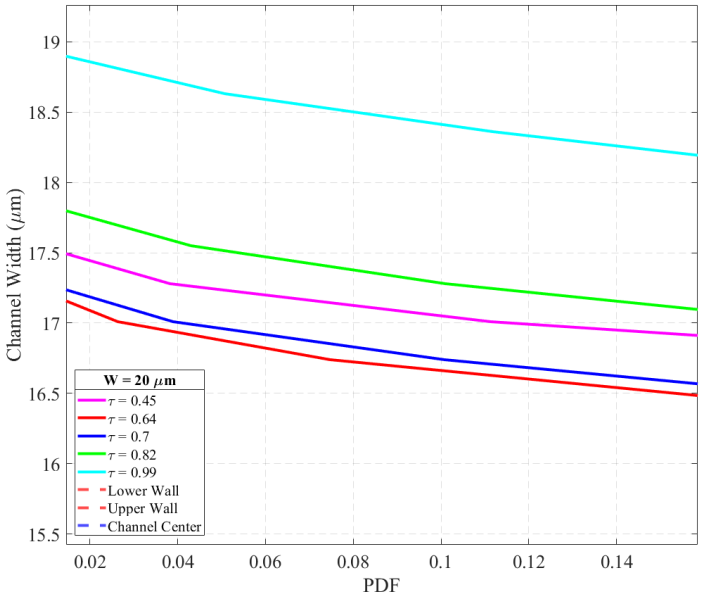

(b) A zoomed View

Fig. 3.7 Spatial distribution of red blood cells in a 20 µm channel (RBCs with fixed area): The influence of reduced area. (a) The Probability density function of RBCs for various reduced areas (0.45-0.99) in a 20 µm channel, with a fixed Hematocrit of 0.4 and $Ca = 18$. (b) A zoomed-in view showcasing the PDF of RBCs for different reduced areas.

We have analyzed the CFL for the other channel widths. In Fig.3.8, it becomes evident that the optimal reduced area value, associated with the highest flux (see Figs.3.1, 3.2 and 3.3) aligns with a thicker cell-free layer. Note that the trend, may appear small in some cases (for example, for $W = 10\ \mu m$, the difference between reduced areas of 0.82 and 0.64 is about 0.3 μm) has been checked with the highest resolution we could achieve. Note also that 0.3 μm corresponds to a relative difference of about $15 - 20$ %, since the CFL width is of about 1.5 μm . This observation sheds light on the correlation between channel width and the reduced area of RBCs:a maximal CFL is correlated with a maximal RBCs flux.

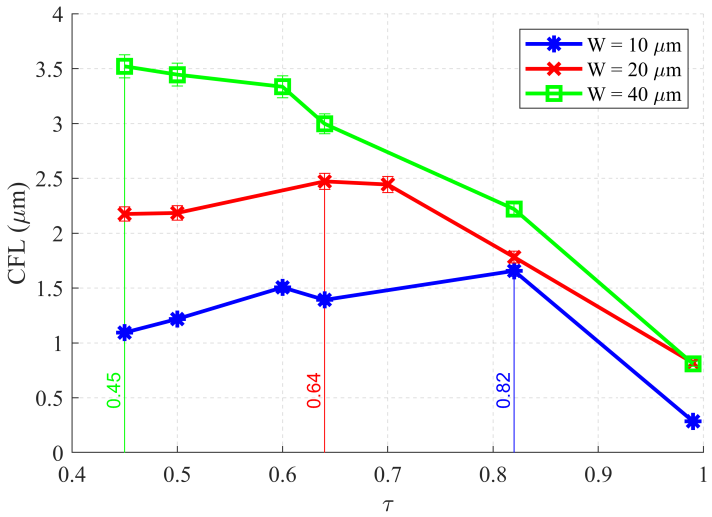

Fig. 3.8 CFL)versus reduced area in a 10 µm 20 µm and 40 µm channel widths (RBCs with fixed Area): This figure demonstrates the relationship between the CFL and reduced area in different channel widths, with a constant Ca of 18, The vertical lines indicate the maximum CFL for corresponding values of τ, 0.45 for W = 40 µm, 0.64 for W = 20 µm, and 0.82 for W = 10 µm ((Hematoctit corresponds to the higher flux: 41% for W = 10 µm, 40% for W = 20 µm and 30% for W = 40 µm))

RBCs diffusion

To quantify the spatial dispersion of a particle over time, we calculated the variance of the displacements as a measure of the distribution of individual cell displacements from the mean. The variance at time t was computed as $\mathrm{Var}(t) = \langle (d(t) - \langle d(t) \rangle)^2 \rangle$, where $d(t)$ is displacement of a particle after time t, and $\langle d(t) \rangle$ is the mean displacement at time t. The average in the variance is a sum over all particles.

Subsequently, we calculated the diffusion coefficient (D), a measure that characterizes the rate at which the cells spread from their initial positions over time.

Assuming a one-dimensional (in the y-direction; this is legitimate since over a long time the flow becomes quasi-translationally invariant along the flow direction) random walk, the diffusion coefficient for a given time lag was calculated using the formula $D(\text{lag}) = \text{Var}(\text{lag})/(\text{lag} \times dt)$,where lag $\times$ dt is the elapsed time between two consecutive time intervals (lag) for which the measurement is performed. Each time frame interval is large in comparison to the computational step time, but small in comparison to the full simulation time. Typically, the time frame interval choice is motivated by a the fact the cell configuration has changed by about few percents during that time.

A large diffusion coefficient signifies an elevated degree of cellular dispersion, indicative of increased cellular mobility within the microfluidic channel. This phenomenon results in the formation of a narrower cell-free layer (refer to Fig. 3.8), an essential characteristic impacting blood flow dynamics, as discussed above. Conversely, a small diffusion coefficient implies restricted cellular movement in the y-direction, constraining the cells closer to the central region of the channel and consequently leading to a wider CFL. This alteration in the CFL dimension contributes to variations in blood flow velocity, resulting in distinct flow profiles.

Our study reveals a clear relationship between the diffusion coefficient and blood flow, as elucidated in Fig.3.9. Specifically, lower values of D are intimately associated with heightened blood flow rates. This association coincides with a thicker CFL, as demonstrated in Fig.3.8, and is especially pronounced when the reduced area of red blood cells approaches the optimal value (see Fig.3.4), signifying a decreased cellular dispersion within the channel. High D values yield a thinner CFL, often correlated with a reduced area value of 0.99, resulting in a markedly reduced blood flow rate. Notably, the lower D values consistently yield maximum blood flux across the range of channel widths studied.

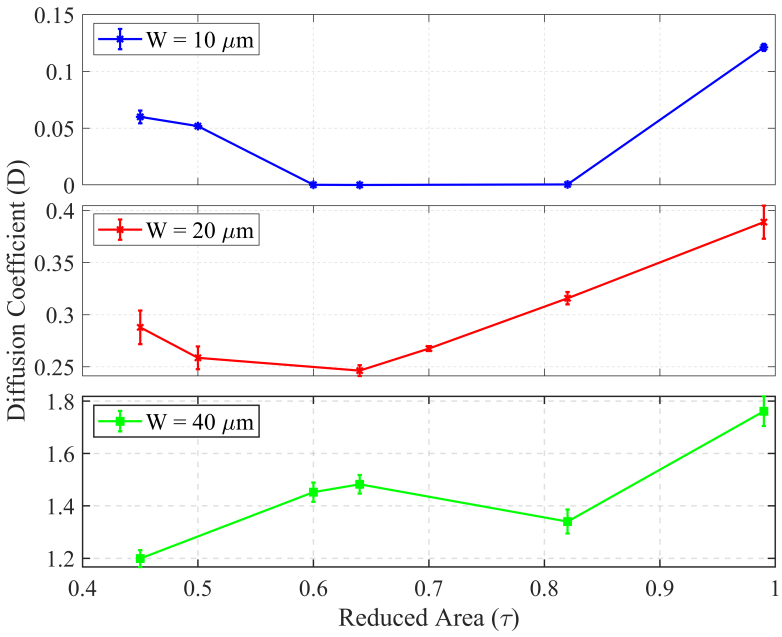

Fig. 3.9 Diffusion coefficient versus the reduced areas: The lower diffusion corresponds to the higher flux value (RBCs with Fixed Area): In a 10 µm ($Cn = 0.54$) channel, for a hematocrit of 0.4, where we have the higher flux,in a 20 µm ($Cn = 0.27$) Channel, for a hematocrit of 0.4, where we have the higher flux and in a 40 µm ($Cn = 0.14$) channel, for a hematocrit of 0.3, where we have the higher flux.

Optimal flux values

In this section, we present optimal values derived from our numerical investigation. Fig.3.10 presents the maximal flux as a function of the reduced area, discerning various studied channel widths. Notably, our analysis reveals that within a channel width of 40 µm, the maximum of blood flux is achieved at a reduced area value of 0.45. Conversely, when the channel width is reduced to 10 µm, the blood flux is optimal for a reduced area of about 0.82.

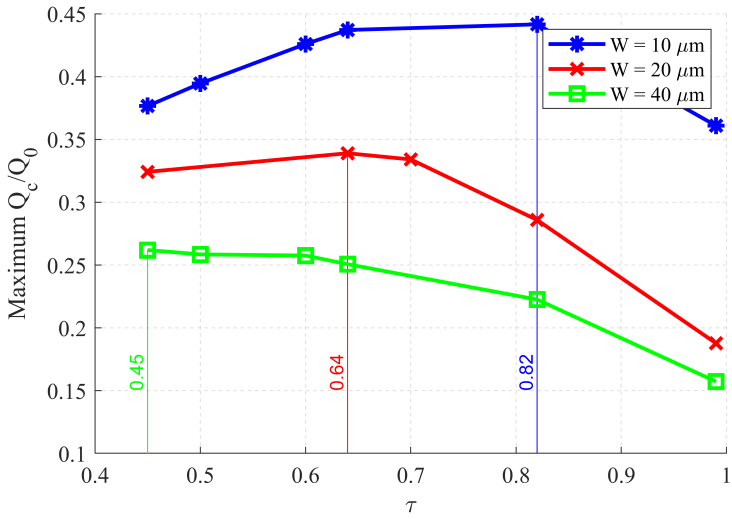

Fig. 3.10 Maximum flux for studied reduced areas in different channel widths: This figure displays the corresponding maximum flux for each of the reduced areas studied (Hematoctit of 41% for W = 10 µm, 40% for W = 20 µm and 30% for W = 40 µm), in channels with widths of 10 µm, 20 µm, and 40 µm (RBCs with fixed area).

Furthermore, Fig.3.11 shows the multifaceted dependency of maximum blood flux on both the reduced area and channel width. For instance, a reduced area of 0.99 yields a maximum blood flux (dimensionalized by Q_0) of approximately 0.36, whereas a channel width of 20 µm corresponds to a reduced blood flux of approximately 0.19.

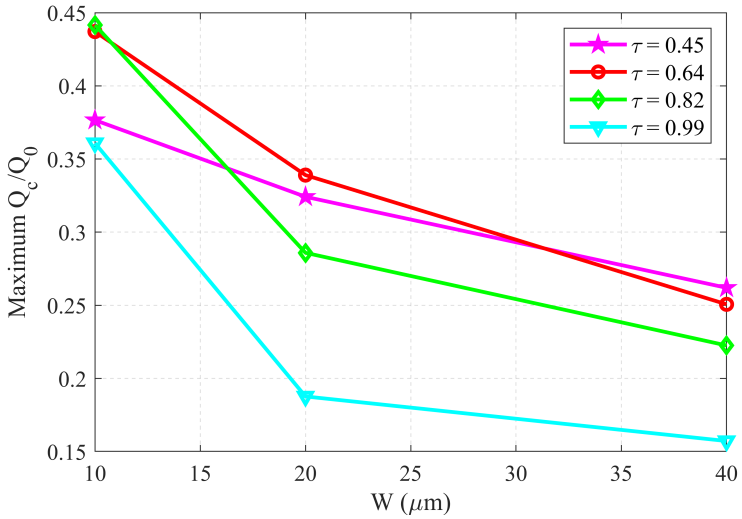

Fig. 3.11 Optimal flux versus Channel Width for different reduced areas: This figure shows the relationship between the optimal flux and channel width for various reduced areas of 0.45, 0.64, 0.82, and 0.99 (RBCs with fixed area).

Fig.3.12 supplements our analysis by shedding light on the optimal hematocrit levels that correlate with the highest attainable blood flux. In the context of a 40 µm channel width, our findings indicate that the optimal hematocrit concentration, which results in maximum blood flux, is 30% for all explored reduced area values, except for spherical cells where it decreases to 20%. Conversely, in the case of a 20 µm channel width, the optimal hematocrit level is approximately 40%, with the exception of spherical cells, which plateau at 30%.

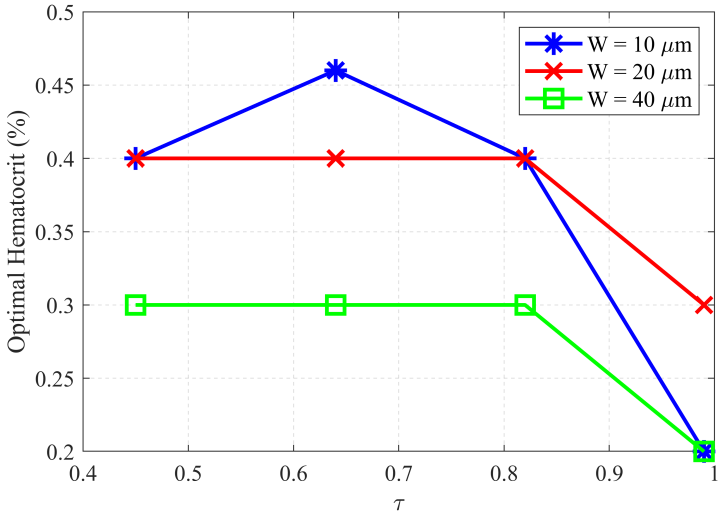

Fig. 3.12 Optimal volume fraction for maximum RBCs flux versus reduced area in different channel widths (10 µm ($Cn = 0.54$), 20 µm ($Cn = 0.27$), and 40 µm ($Cn = 0.14$)): This figure illustrates the optimal volume fraction where the highest RBCs flux is achieved, as a function of the reduced area for three distinct channel widths of 10 µm, 20 µm, and 40 µm (RBCs with fixed area).

3.2.2 Red blood cells with fixed perimeter

Abnormal shapes (like spherocytosis and ellipsocytosis) have different volumes and/or different areas as compared to healthy shapes [22, 34, 55, 117]. In the previous section, we have assumed that the analog of volume (enclosed area in 2D) is fixed and the perimeter is varied. Here we will fix the cell's perimeter, and vary the cell's area, in order to modify the reduced area. Our primary objective is to investigate whether alterations in either the cell's area or perimeter within the same confinement would yield distinct outcomes.

The main results are presented in Fig.3.13. When we compare these results with those obtained from our previous simulation in the previous section where the cell's area

was kept constant(Fig.3.10), a notable consistency emerges. It becomes evident that the optimal reduced area remains invariant across different channel widths, suggesting a consistent relation.

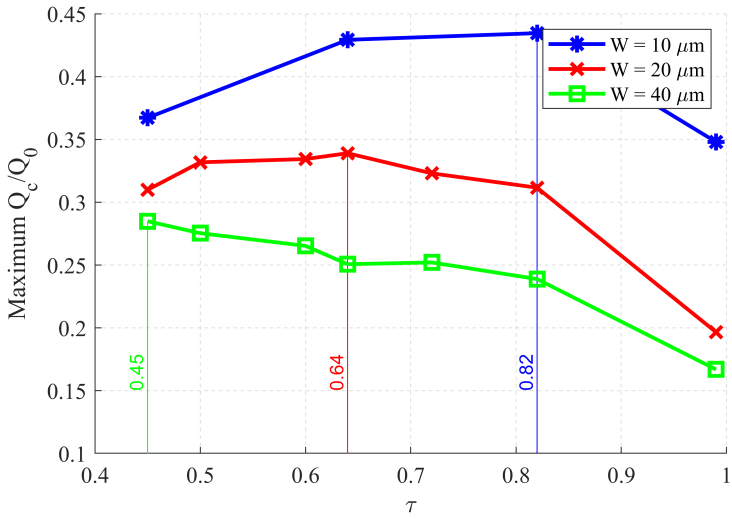

Fig. 3.13 Maximum flux for studied reduced areas in different channel widths (RBCs with fixed perimeter).

From our findings, it can be inferred that the RBC's shape and deformability are central to its interaction with the surrounding environment and, consequently, its ability to navigate through narrow channels. The consistency of optimal reduced areas across various channel widths implies that the cell's morphology and deformability might play a more critical role than its specific geometric parameters (area or perimeter) in influencing blood flow behavior.

3.2.3 The Viscosity contrast and capillary number effect on blood flow and CFL

The principal aim of this section is to investigate the effects of viscosity contrast and red blood cell rigidity on blood flux and the CFL. Our findings suggest that viscosity contrast does not exert a significant influence on blood flux, even when considering variations in cell sphericity. Moreover, the trend of blood flux remains consistent across changes in RBC rigidity. Similar observations hold true for the CFL trend. These results contribute supplementary insights to existing investigations, particularly concerning fixed capillary numbers and viscosity contrasts outlined previously in this chapter.

The Viscosity contrast effect on Blood Flux: Figure 3.14 illustrates the blood flux as a function of hematocrit for two distinct reduced areas (0.64 and 0.99) and two viscosity contrasts (1 and 6). Our simulations reveal that variations in viscosity contrast do not yield significant differences in blood flux.

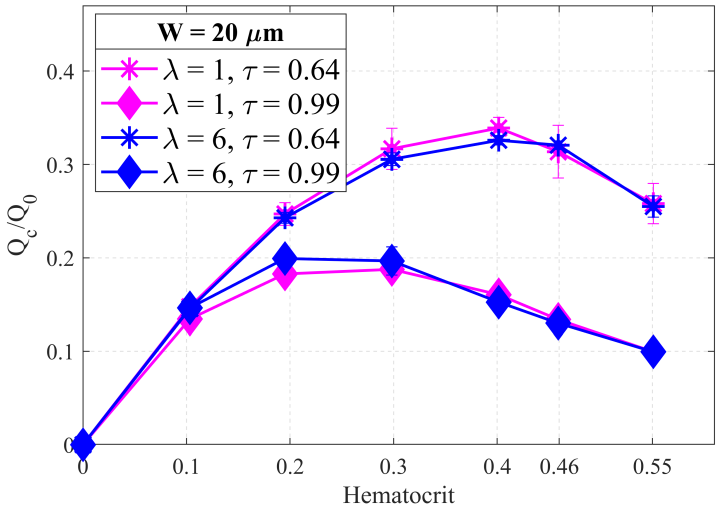

Fig. 3.14 Flux vs. Hematocrit: Viscosity Contrast Effects in a 20μm Channel ($Cn = 0.27$). Fixed-area RBCs across reduced areas 0.64 and 0.99 viscosity contrasts of 1 and 6, $Ca = 18$.

The capillary number effect on blood flux: The adjustment of cell rigidity by varying the capillary number from soft ($Ca = 18$) to rigid ($Ca = 0.2$) is demonstrated in Figure 3.15. Within a channel width of 10 microns, the trend persists: cells with a reduced area of 0.82 consistently exhibit higher flux, despite the overall decrease in blood flux by decreasing Ca.

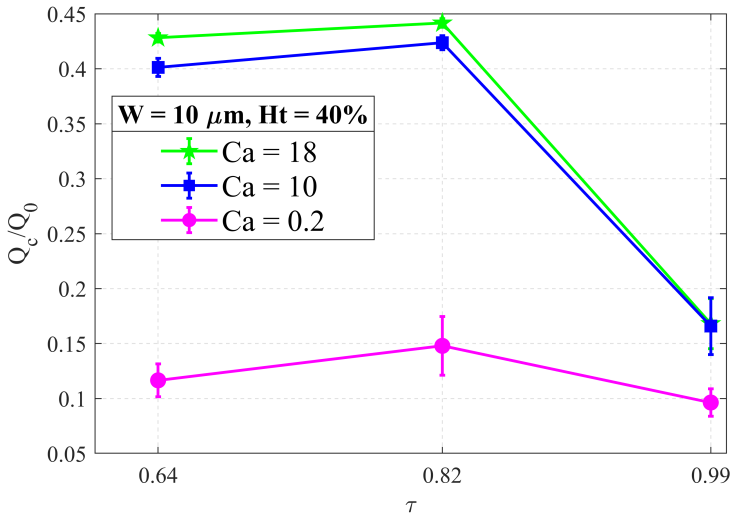

Fig. 3.15 Flux vs. Reduced Area in a 10μm ($Cn = 0.54$) Channel (Fixed-area RBCs) for Various Capillary Numbers (18, 10, and 0.2), Hematocrit of 41%(Maximum Blood Flux Value).

The capillary number effect on CFL: In Figures 3.16, 3.17, 3.18, and 3.19, we present the spatial distribution of red blood cells and cell-free layer for various degrees of RBC rigidity. Remarkably, even with higher cell rigidity, a consistent trend is observed across the range of examined reduced areas: the thicker CFL consistently corresponds to the reduced area of 0.82 for the channel width of 10 microns.

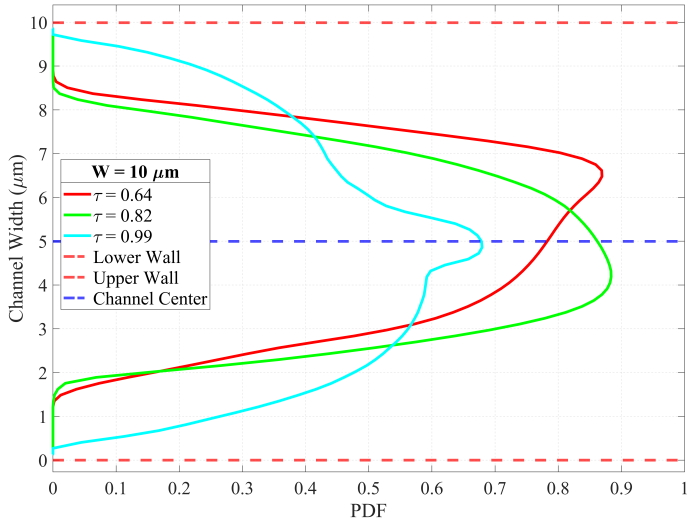

(a) Spatial Distribution of Red Blood Cells for different reduced area values

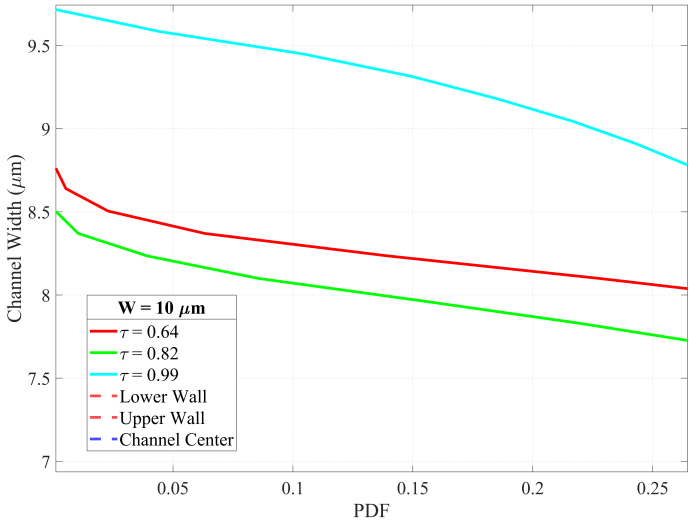

(b) A zoomed View

Fig. 3.16 Spatial distribution of red blood cells in a 10µm channel (RBCs with fixed area): The influence of reduced area. (a) The Probability density function of RBCs for various reduced areas (0.64-0.99) in a 10µm channel,a Hematocrit of 41% and Ca of 10. (b) A zoomed-in view showcasing the PDF of RBCs for different reduced areas.

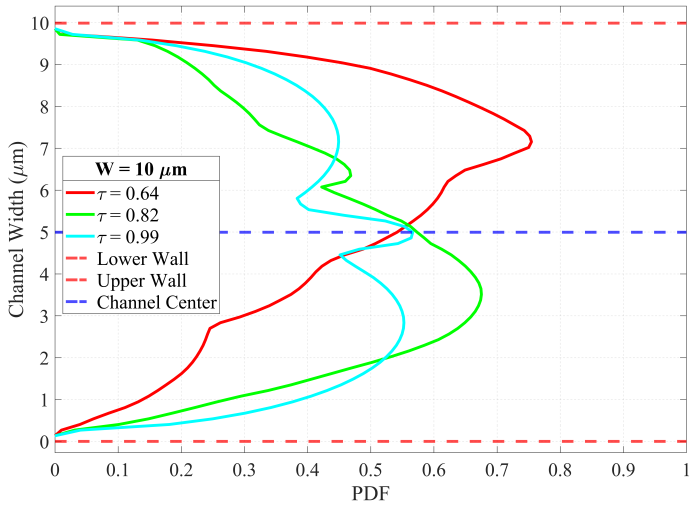

(a) Spatial Distribution of Red Blood Cells for different reduced area values

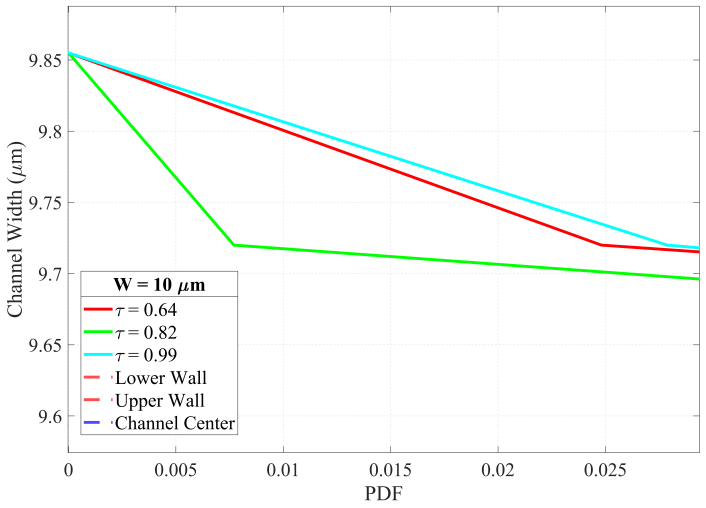

(b) A zoomed View

Fig. 3.17 Spatial distribution of red blood cells in a 10µm channel (RBCs with fixed area): The influence of reduced area. (a) The Probability density function of RBCs for various reduced areas (0.64-0.99) in a 10µm channel, a Hematocrit of 41% and Ca of 0.2. (b) A zoomed-in view showcasing the PDF of RBCs for different reduced areas.

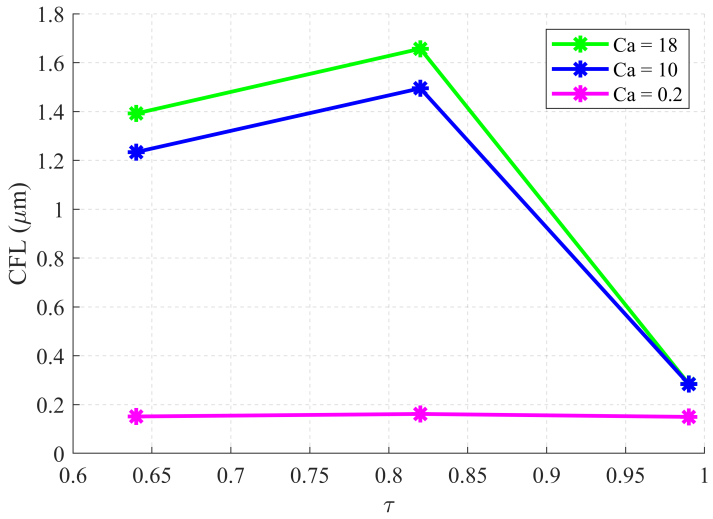

Fig. 3.18 CFL versus the reduced ares in a 10μm ($Cn = 0.54$) channel width (RBCs with fixed area) for different Capillary number (18, 10 and 0.2) a hematocrit of 41% (Value of the higher blood flux).

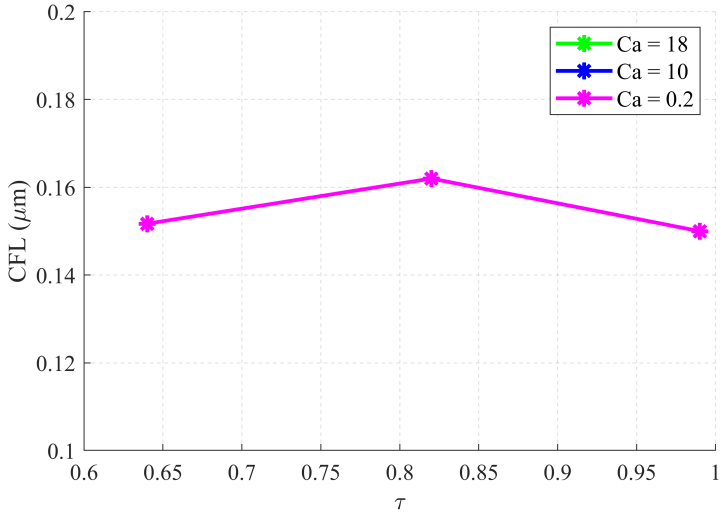

Fig. 3.19 Zoomed-in view from figure 3.18 showcasing the CFL as a function of the reduced area for Ca=0.2.

3.3 Conclusion

In summary, our investigation in this chapter has yielded some insights into the intricate relationship between channel dimensions and the optimal reduced area regarding the

RBCs flux. Additionally, our investigation led to the fact that the cell-free layer (CFL) and the diffusion coefficient are correlated with optimal flow.

These findings offer a deeper understanding of the hemodynamic implications of RBC morphological anomalies. We have shown, in particular, that for a reduced area close to one (the case of spherocytosis) leads to a collapse of RBCs flux, attaining up to 50 %. This should severely compromise oxygen and other metabolites transport in microcirculation.

Several questions deserve future consideration. Firstly, our study has a limitation since it is focused on a 2D situation. While several studies (including ours)[115, 26, 95, 24]had reported on similarities of behaviors in 2D and 3D, a systematic analysis of 3D flow is necessary. Secondly, we have found that the optimal reduced area depends on channel width. Since in real vascular networks, different vessels have different diameters, it is not yet clear how our findings can be translated to real microvasculatures. A systematic study of blood flow in complex geometry is necessary in order to build a clear conclusion about the impact of shape abnormalities on blood flow transport. It is hoped to investigate these questions in future work.

Chapter 4

The Effect of Heterogeneous Red Blood Cell Suspension on Blood Flow in Spherocytosis

Note: This work has already been submitted to Physical Review Fluids and is available as a preprint.

4.1 Introduction

The morphology of RBCs, characterized by their shape and size, is an essential factor to their physiological function. In health, RBCs typically exhibit a biconcave discoid shape, optimizing their capacity (due to their ample deformation) to deliver oxygen (and other metabolites, such as ATP) throughout the body. However, deviations from this norm, such as abnormalities in RBC morphology, can profoundly impact their function [76]. Notable deviations from the bi-concave shape include spherocytes, elliptocytosis, schistocytes, stomatocytes, knizocytes, and mushroom-shaped cells, each manifesting distinct alterations in RBC shape [84].

In the realm of RBC disorders, spherocytosis (RBC has a sphere-like shape) stands out as a condition of particular interest. Beyond the inherent variations in RBC morphology, hereditary spherocytosis (HS) emerges as a significant concern. In the regions of North Europe and North America, the prevalence of HS among neonates is estimated at approximately 1 in 5,000 and 1 in 2,000, respectively [75]. Furthermore, it stands as the most prevalent hereditary hemolytic anemia in Japan [120].

Spherocytes are more vulnerable to destruction by the spleen than their normally shaped counterparts. Consequently, spherocytosis may lead to complications, including splenomegaly (enlarged spleen) and anemia. In such cases, splenectomy, the surgical removal of the spleen, is a common therapeutic intervention aimed at mitigating the excessive destruction of spherocytic RBCs, ultimately improving anemia and related symptoms [16].

Recently, using numerical simulations, Bendaoud et al [11], analysed flow properties such as flow rate, cell-free-layer, and RBCs hydrodynamic diffusion, by varying RBC shapes from healthy biconcave to spherical representing diseased RBCs in a homogeneous suspension (e.g. all cells have the same shape and properties). Their findings revealed complex relationships, such as nonmonotonic behaviors of flow rate with asphericity, dependent on channel width.

In general, however, spherocytes typically constitute only 15% to 20% of the total RBCs [40] in patients suffering spherocytosis. The question naturally arises of how does this proportion of abnormal cells affect the flow properties. This led us to systematically analyse the behavior of heteregenous suspensions, not only including spherocytes, but also other shapes. For example, besides spherocytes, and in the spirit of research on artificial blood, it may be important to answer the question if more flexible cells than discoid shape would offer, or not, a better flow efficiency. Thus, our investigation includes the study of conditions similar to spherocytosis but also situations with more flexible cells, and we will systematically analyse the viscosity and RBCs flux.

We will explore different percentages of different cell shapes. We will perform numerical simulations based on the Lattice-Boltzmann Method (LBM) in 2D. The shape of RBC will be characterized by their reduced area, which is equal to about 0.64 for healthy RBCs and about 1 for spherocytes. We have observed that 15% and 20% of spherocytes lead (i) to a collapse of RBCs flux up to 50%, and (ii) that blood viscosity is enhanced by about a factor 2.

A notable discovery in this study is the non-monotonic behavior of RBC flux as a function of the spherocyte proportion. Specifically, we observed that a suspension composed entirely of spherocytes exhibits a lower RBC flux compared to a homogeneous suspension of discocytes. However, intriguingly, it demonstrates higher flow efficiency than suspensions containing an intermediate proportion of spherocytes (20–40%). In this paper, we will present a fundamental explanation for this behavior.

In order to highlight the important role of spherocytes, we will compare the resulting RBCs flux for heterogeneous suspensions containing spherocytes to the case of suspensions containing a proportion of other shapes (with reduced area smaller than

that of the normal shape). When introducing more deflated cells than discoid shapes in a certain proportion, we find a weaker RBCs flux as compared to the reference discocyte suspension, but the flux remains much higher than a heteregenous suspension of discocytes and spherocytes.

4.2 Numerical setup

The LBM method is built in order to mimic the Navier-Stokes equations. On the scale of a RBC the Reynolds number is very small (less than 10^{-3} in microcirculation), corresponding practically to the Stokes regime. However, the LMB inherently incorporates finite inertial effects. Using a real Reynolds number poses numerical challenges due to the prohibitive computational cost required for accurate simulation over relevant timescales. Extensive benchmarks within the scientific literature have delineated a threshold for the Reynolds number, below which the LBM accurately emulates flow conditions characteristic of the Stokes regime. Consensus suggests that a Reynolds number of 0.1 strikes an optimal balance, offering a pragmatic compromise between numerical efficiency and the fidelity of simulation outcomes [107, 113, 116, 121, 48]. . Consequently, our simulations cap the Reynolds number at a maximum value of 0.1, aligning with established guidelines to ensure both computational viability and the accuracy of our flow dynamics representations.

In this investigation, our focus is directed toward heterogeneous suspensions of blood, considering variability in the shapes's sphericity of RBCs. Periodic boundary conditions are employed in the flow direction. To prevent numerical artefacts caused by periodic boundary conditions, the channel length is taken equal to five times the width of the channel[114].

Within this investigation, we conducted a comprehensive analysis of cell flux and blood viscosity, scrutinizing their dependence on various key parameters: (i) hematocrit, (ii) the proportion of mixing, (iii) viscosity contrast (iv) confinement, and (v) capillary number.

4.3 Results and discussion

4.3.1 Heterogeneous Blood Flux in straight channels

Let us recall that in hereditary spherocytosis, spherocytes make up around 15% to 20% of the total RBCs population [40]. Our first investigation consisted in analyzing

how spherocytes impact blood flow. We explored a full spectrum of heteregenous suspensions, from cases of zero abnormal shapes up to 100 %. Besides spherocytes, we also explored shapes which are either more deflated or less deflated than the discocyte shape, in order to have a general view on the impact of abnormal shapes on blood flow. This was also motivated by the question of whether a more deflated cell (and thus more flexible) than ordinary biconcave shape can provide, or not, a better flow efficiency.

We observed a noticeable decline in flux when RBCs with different reduced areas were combined, as illustrated in Fig. 4.1. This effect was particularly pronounced when the suspension included spherical cells (indicated by black, purple, and blue curves). In contrast, when mixing non-spherical cells with different reduced areas ($\tau = 0.45$ and $\tau = 0.64$) or even with nearly spherical cells ($\tau = 0.82$), the decrease in flux was less pronounced compared to suspensions composed entirely of healthy cells ($\tau = 0.64$). This shows that spherocytes have much more impact on flux decline than other shapes.

A remarkable fact, and a priori counter-intuitive, is that the RBC flux of a suspension made of 100 % of spherocytes (black curve in Fig. 4.1) leads to better perfusion (higher flux) than when the suspension has 70% or 80% of healthy biconcave shapes and only 20% or 30% of spherocytes (purple and blue curve in Fig.4.1). We will provide a basic explanation on this behavior in section 4.3.5. Finally, the RBCs flux for healthy cells (orange curve in Fig. 4.1) declines by about a factor of 2 compared to the case where 20% of spherocytes are present (purple curve in Fig. 4.1). This a quite an ample decline, which should seriously compromise oxygen and other metabolites delivery to organs and tissues.

We have also examined the case when cells with other shapes (having reduced area 0.45, 0.82) are added to a healthy suspension (70% of RBCs that have $\tau = 0.64$ + 30% of RBCs that have $\tau = 0.45$ or 80% of RBCs that have $\tau = 0.64$ + 20% of RBCs that have $\tau = 0.45$). In this case the flux decline (as compared to a healthy situation) is modest, up to about 10%. Finally, in the case of 100% of cells with reduced area 0.45 (red curve in Fig. 4.1), the maximum flux remains below that of a biconcave shape suspension. That is, even if a cell with a reduced area of 0.45 has ampler deformation than a biconcave shape, there is no gain in RBCs flux. For more clarity we also report the maxima of Fig. 4.1 in Fig. 4.2, allowing to have a simpler reading of the effect of different reduced areas.

The reduction in flux due to shape evolution, as well as to heterogeneity, can be attributed to changes in the contact area between cells of varying shapes, an effect that becomes more significant in the presence of spherical cells. This can be explained

by the differences in drag forces encountered by cells of different shapes, which lead to variations in their velocities. Consequently, these velocity fluctuations increase the likelihood of intercellular collisions, thereby disrupting the flow dynamics. This will be further discussed in subsequent sections.

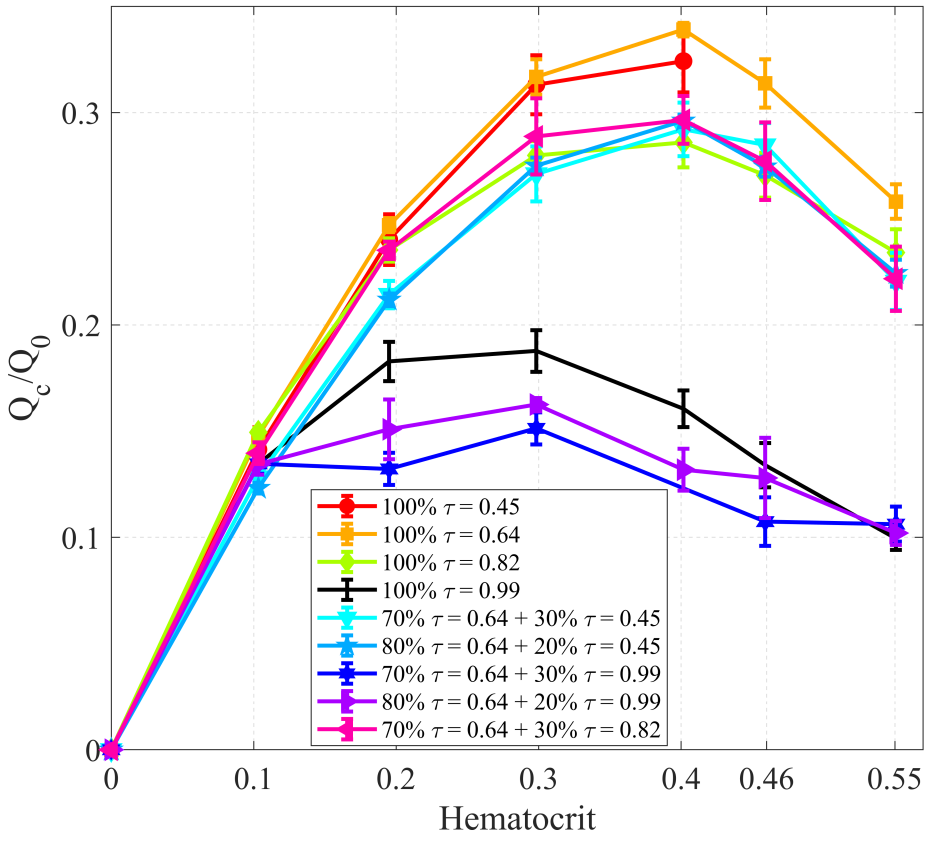

Fig. 4.1 Normalized RBCs flux versus hematocrit for four cases: Homogeneous suspension (RBCs with $\tau = 0.45$, $\tau = 0.64$, $\tau = 0.82$ and $\tau = 0.99$), heterogeneous suspension by mixing with non-spherical RBCs (mixture of RBCs with $\tau = 0.45$ and $\tau = 0.64$, with different proportions 20% - 80% and 30% - 70%), heterogeneous suspension by mixing with nearly spherical cells ($\tau = 0.82$) and heterogeneous suspension by mixing with spherical RBCs (mixture of RBCs having $\tau = 0.99$ with RBCs having $\tau = 0.64$). $Ca = 18$, W = 20 µm and $\lambda = 1$.

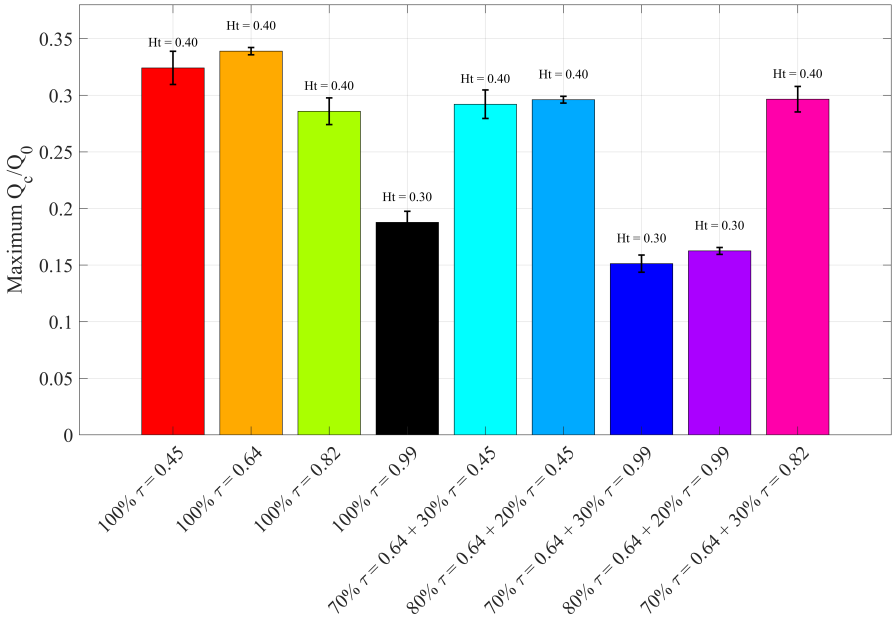

Fig. 4.2 Comparison of maximum normalized RBCs flux across different τ and different mixtures

4.3.2 Systematic analysis of the impact of spherocytes proportion

Our investigation will focus on examining the interplay between two specific reduced areas: $\tau = 0.64$, which represents the optimal reduced area in a channel width of 20 µm and corresponds to healthy cells [12], and $\tau = 0.99$, which indicates spherocytes with significantly reduced flow rates. We investigated three channel widths 10 µm, 20 µm, and 40 µm, and two hematocrit values around 20% and 50% with a capillary number of 18 (Fig. 4.3).

Let us first comment on Fig. 4.3a (for hematocrit of about 20%; note that since the number of cells is discrete, it is not possible to have exactly the same hematocrit for different channel widths). Curves have a non-monotonic behavior, with two maxima at 0 (homogeneous spherocyte suspension) and 100% (homogeneous biconcave shape suspension). For this hematocrit the maximum at 100% is slightly larger than that at 0%. Here again, we see that it's more beneficial to have a whole suspension of spherocytes than to have a heterogeneous suspension containing even a high enough proportion of healthy shapes. The same conclusion is reached for all three channel widths

The presence of spherical cells in the suspension has a more significant impact for a hematocrit of 50% (Fig. 4.3b). Firstly, the difference between the flux of a pure spherical cell suspension and a suspension containing healthy cells is much more pronounced (it is about 4 times higher for $W = 10\text{ţ}m$). Secondly, as soon as the proportion of spherocytes reaches about 20 % (a usual proportion in spherocytosis [40]) the slope of the decrease in RBC flux becomes significantly lower after reaching 20% spherocytes compared to the steeper decline observed between 0% and 20%. This effect is more pronounced under lower confinements (W = 20 µm and W = 40 µm) at higher hematocrit levels, where the flux approaches a near-plateau, This suggests that the presence of just 20% or lower of spherocytes has a substantial impact on the flow dynamics.

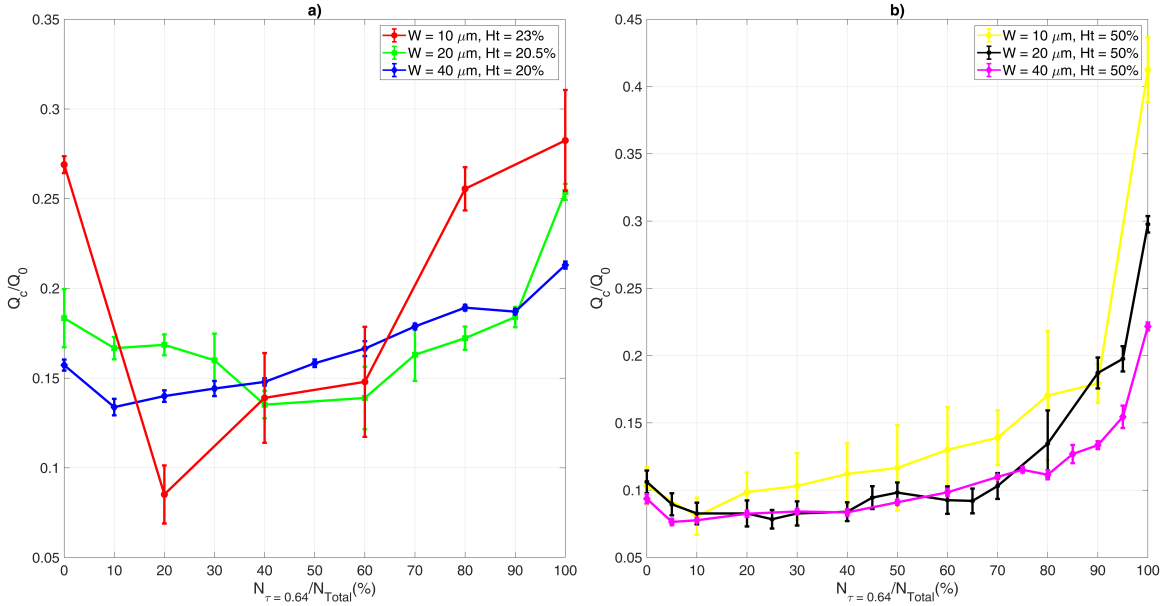

Fig. 4.3 Normalized RBCs flux of suspension containing discocytes ($\tau = 0.64$) and spherical cells ($\tau = 0.99$) as a function of the relative concentration of healthy cells $N_{0.64}/N_{Total}$ ($N_{Total} = N_{0.64} + N_{0.99}$). Channel widths 10 µm, 20 µm, and 40 µm, Ca = 18, $\lambda = 1$: a) Hematocrit around 20% b) hematocrit of 50%.

These observations highlight two essential factors. A notable decrease in flow occurs when spherical shapes are mixed with normal RBCs, when compared with both pure suspensions with all spherocytes and all discocytes, with a distinct inflection point at approximately 20% concentration, especially for the higher concentration of 50%. This finding is consistent with reports indicating that spherocytes typically make up to 20% of the total RBCs observed in the peripheral blood smear of patients with spherocytosis

[40]. The quite ample decline of RBCs flux reported for a such moderate proportion (20%) could explain symptoms such as shortness of breath and lack of energy.

4.3.3 Blood Rheology

Figure 4.4 illustrates a significant trend in the effective viscosity of blood within homogeneous and heterogeneous suspensions. The presence of spherical cells substantially increases effective viscosity, with this effect being also detected in suspensions composed entirely of spherocytes (100% $\tau = 0.99$). The effective viscosity becomes even higher in mixtures of spherical and healthy cells in a range of hematocrit values (around 20%, 30% and 46%). Conversely, the effective viscosity is considerably lower in homogeneous suspensions and when mixing with elongated cells ($\tau = 0.45$) or nearly-spherical cells ($\tau = 0.82$), such as those with 100% healthy cells ($\tau = 0.64$) or another condition (20% $\tau = 0.99$ + 80% $\tau = 0.64$). In the presence of spherocytes (al least with 20% proportion), the increase of viscosity lies between about 50% and 200% for hematocrit 20% and 40%, respectively. This is again a quite ample increase that seriously compromise blood perfusion.

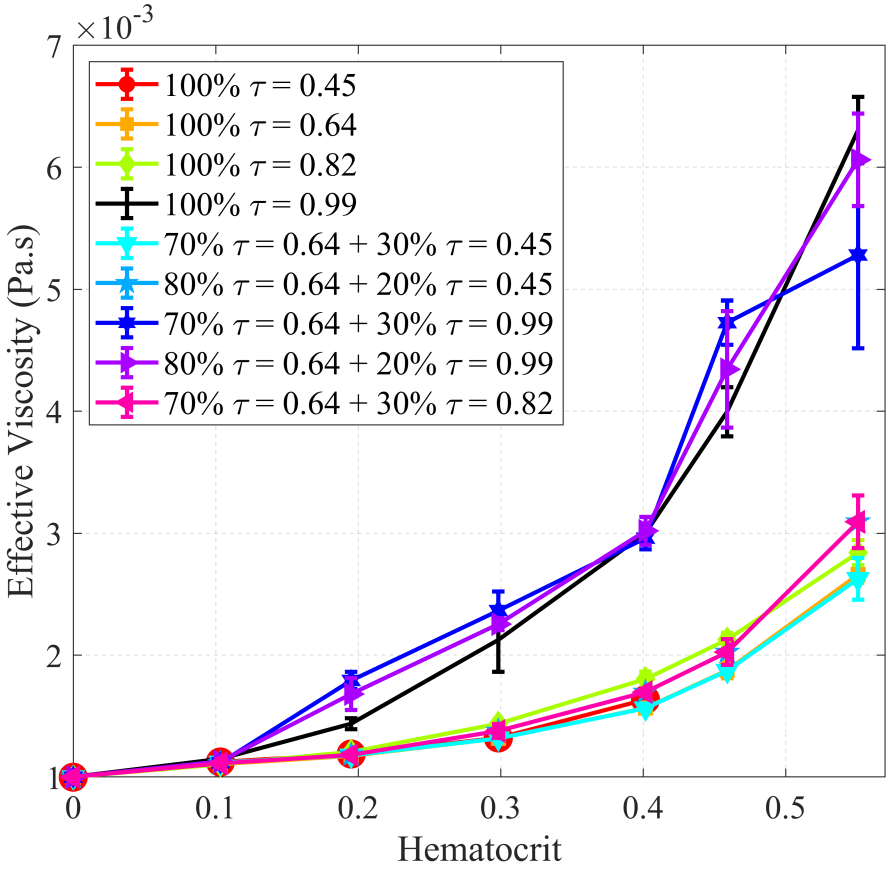

Fig. 4.4 Effective viscosity versus hematocrit for a homogeneous suspension and heterogeneous suspension (mixing with spherical cells, with elongated cells, and with nearly-spherical cells), $Ca = 18$, W = 20 µm and $\lambda = 1$.

Figure 4.5 explores the impact of varying the relative concentrations of spherocytes for two fixed hematocrits (20 % and 50 %).

The suspension exhibits a lower effective viscosity when predominantly composed of healthy cells, indicative of more efficient blood flow. Conversely, as the proportion of spherocytes increases, so does the suspension's viscosity. A significant increase is already obtained at the proportion of about 20% of spherocytes, attaining 40% and about 200% for hematocrits 20% and 50%, respectively.

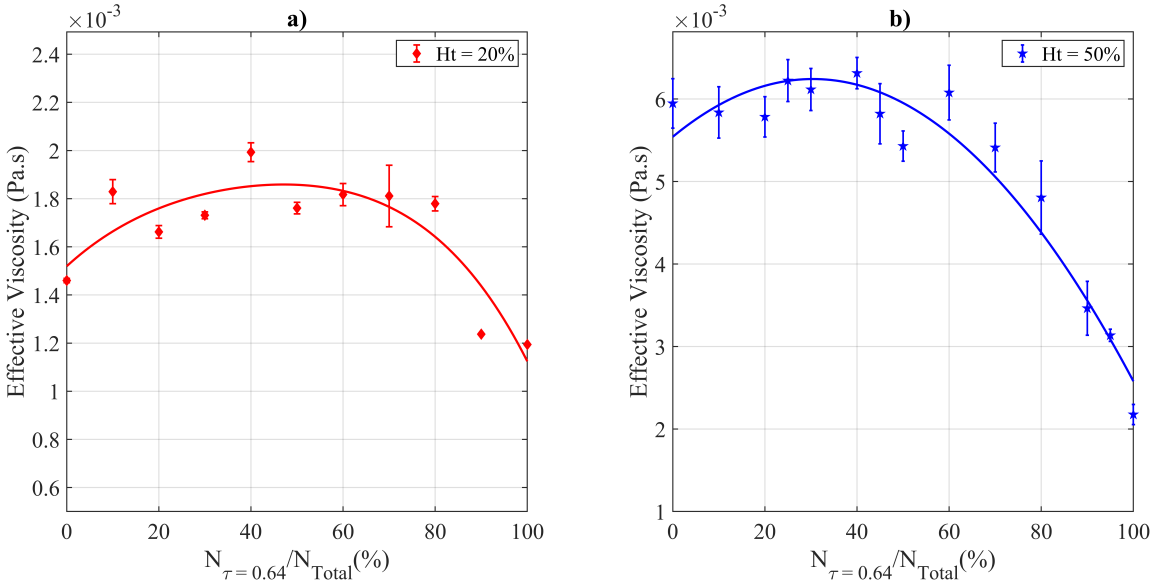

Fig. 4.5 Effective viscosity of suspension containing discocytes ($\tau = 0.64$) and spherical cells ($\tau = 0.99$) as a function of the relative concentration of healthy cells $N_{0.64}/N_{Total}$ ($N_{Total} = N_{0.64} + N_{0.99}$). Channel width is 20 µm and Ca = 18 (Full lines are a guide for the eyes): a) Hematocrit 20% b) Hematocrit 50%.

4.3.4 Cells rigidity effect

We conducted a study on the impact of red blood cell rigidity in spherocytosis conditions, specifically by modulating the capillary number and adjusting the viscosity contrast between the interior and exterior of the RBCs. In Fig. 4.6, we present the normalized RBCs flux of suspensions containing both healthy cells and spherocytes as a function of the relative concentration of healthy cells. Table 4.1 displays the maximum flow velocity in the absence of cells in the channel center for different capillary numbers considered in this study.

Table 4.1 Maximum flow velocity at the channel center in the absence of cells for different Capillary numbers.

Capillary Number (Ca)	0.5	1	18	90
Maximum Velocity (mm/s)	0.038	0.076	1.37	6.85

Figure 4.6 shows that the flux is higher for softer cells (red curves). This is expected since cell deformation enhances the flow trend. Another observation is that this effect is not quite ample for low hematocrit (20%, Fig. 4.6c,e). This is due to the fact that the system is not crowded so that even if a cell is rigidified, it can flow without encountering too many obstacles. The situation is quite different for higher hematocrit

(50%, Fig. 4.6d,f, where (at low proportion of spherocytes), the flux is boosted for $Ca = 18$ (soft cell) as compared to the case with $Ca = 0.5$ (rigid cell). This is due to the fact that soft discocytes can manage to go through interstices of the suspension, as compared to rigid discocytes. However, at high enough spherocyte proportion, the fluxes for rigid and soft cells are quite close to each other. This is due to the fact that a spherocyte has a quite low deformation (even for very high capillary numbers), and behaves as a rigid cell.

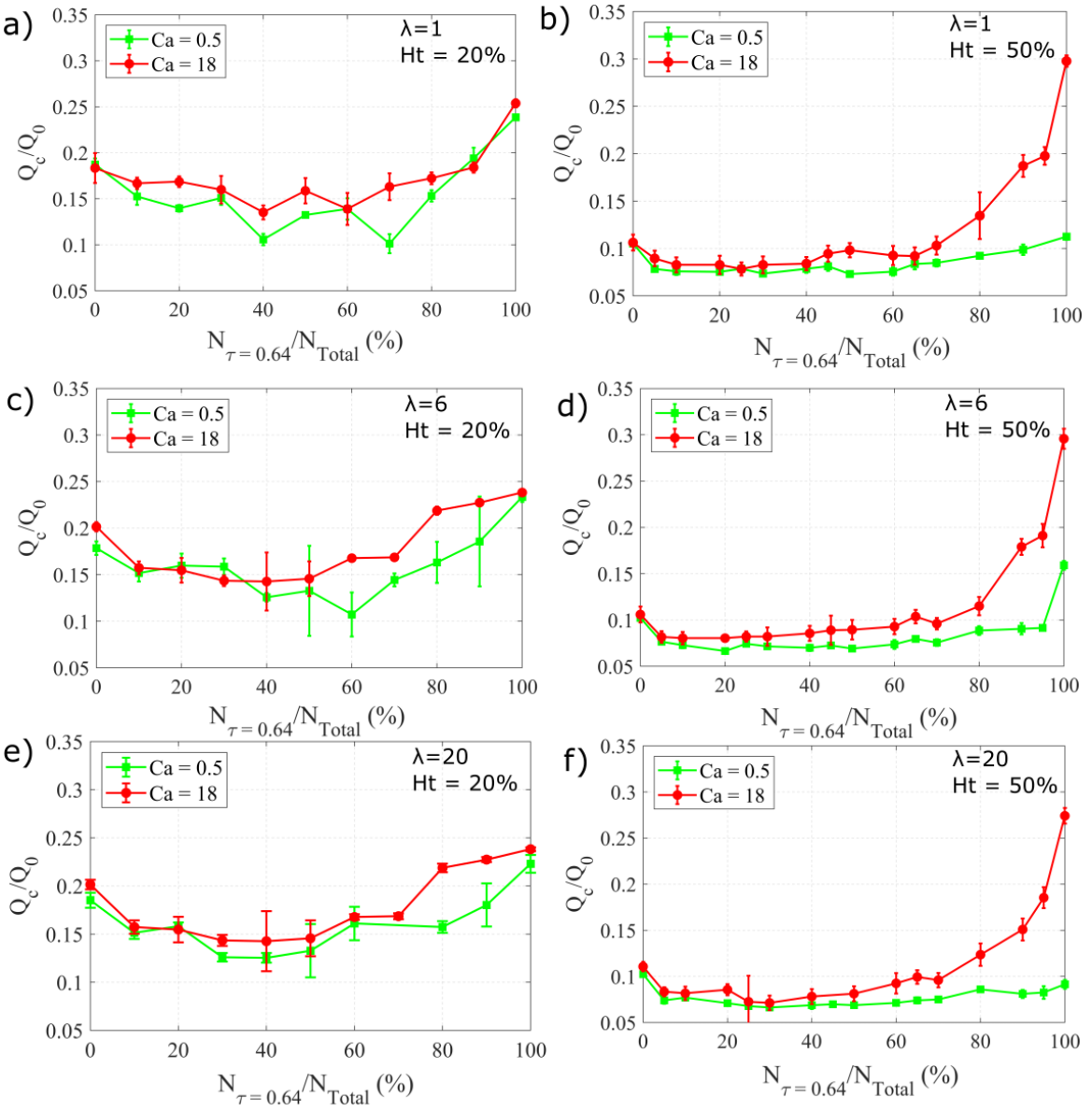

Fig. 4.6 Normalized RBCs Flux of suspension containing discocytes ($\tau = 0.64$) and spherical cells ($\tau = 0.99$) as a function of the relative concentration of healthy cells $N_{0.64}/N_{Total}$ ($N_{Total} = N_{0.64} + N_{0.99}$). W = 20µm: Subfigures a, c and e for $Ht = 20\%$. Subfigures b, d and f for $Ht = 50\%$, $Ca = 0.5$ and 18, $\lambda = 1$, 6 and 20.

4.3.5 Physical interpretations of major results

A. Flow pattern

We have discussed in the section devoted to the results (see Fig. 4.1) that 20% or 30% of spherocytes lower the blood flux more than a suspension of 100% of spherocytes. This may seem a bit counter-intuitive since spherocytes have a quite low deformation. We

have attempted to understand this effect by comparing the RBC pattern for three cases: discocytes, spherocytes, and a mixture of 30% of spehrocytes and 70 % of discocytes (Fig. 4.7a,b,c and corresponding videos in the supplementary materials). An interesting observation is that for a mixture of 30% of spehrocytes and 70 % of discocytes (Fig. 4.7c), spehrocytes constitute an obstacle for discocytes. Discocytes succeed, due to their ample deformation, to navigate between spherocytes by marginalizing them (see also next subsection). The accumulation of spehrocytes (pushed by discocytes) near the walls leads to a lower cell-free layer (CFL) than in the case of a homogeneous suspension of spherocytes (Fig. 4.7b).

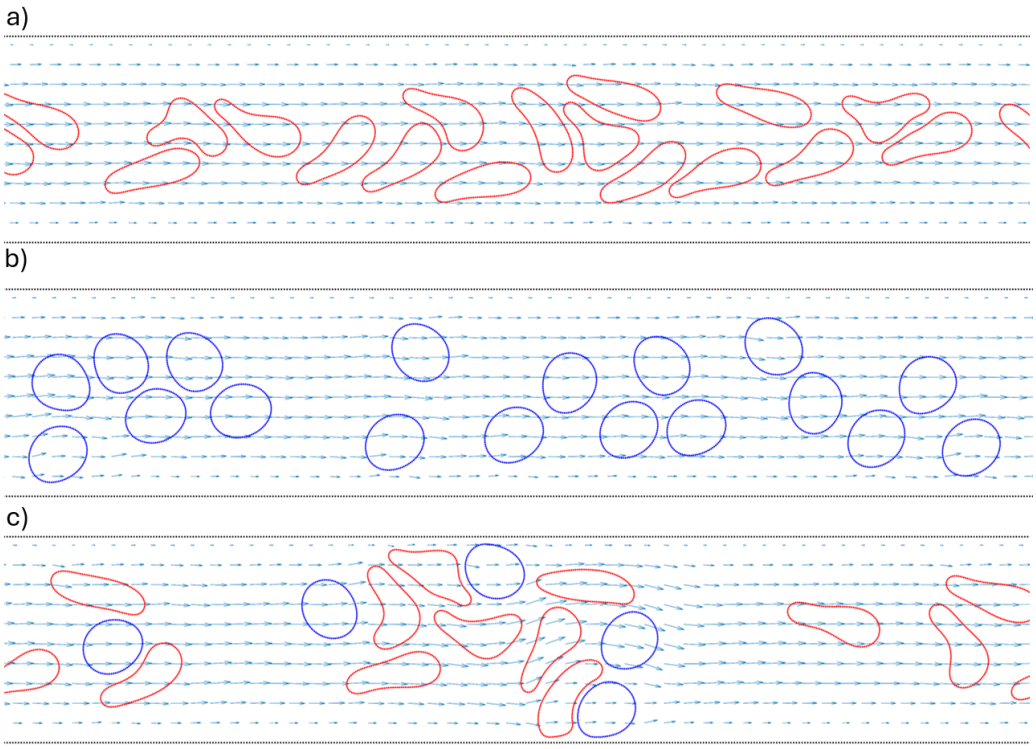

Fig. 4.7 RBCs distribution within the channel (Spherical cells ($\tau = 0.99$) in blue and healthy cells ($\tau = 0.64$) in red, $Ca = 18$, W = 20 µm, hematocrit = 20% and $\lambda = 1$.): a) 100% $\tau = 0.64$, b) 100% $\tau = 0.99$ and c) 30% $\tau = 0.99$ + 70% $\tau = 0.64$

.

B. Cell Free Layer (CFL)

The cell-free layer, also termed the plasma layer or cell-depleted layer, is vital in blood microcirculation, particularly within capillaries and arterioles. This layer, devoid of blood cells and rich in plasma, emerges from an interplay between the wall lift and hydrodynamic cell-wall interactions, facilitating reduced vascular friction and optimizing

flow efficiency [58]. A thicker Cell-Free Layer acts as a flow buffer, diminishing resistance and enhancing blood flow efficiency. In such conditions, RBCs encounter reduced obstruction, resulting in higher flow rates. On the contrary, a thinner CFL increases flow resistance, negatively affecting fluid dynamics and leading to reduced blood flow [24].

In Fig. 4.8, we present the probability density function (PDF) illustrating the spatial distribution of RBCs across different relative concentrations of healthy RBCs in the suspension (for hematoctits 20% and 50%), taking into account the entire cell body rather than just the cell center for greater accuracy in our calculations. Note that the PDF is not fully symmetric, as it should be statistically. This would require a much longer simulation time.

Our analysis of Figs. 4.8 and 4.9 indicate a significant trend. Let us first focus on hematocrit 20% (Figs. 4.8a and 4.9a). It is seen that the CFL is maximum for healthy cells, and goes through a minimum in the middle range of spherocytes proportion. This means that a finite proportion of spherocytes leads to a lower flow efficiency, as discussed in the last subsection. This explains the non monotonous behavior of the RBCs flux as a function of spherocytes proportion, as summarized in Fig. 4.5

Regarding the case of hematocrit 50% (Figs. 4.8b and 4.9b) we observe a monotonic behavior with an increase of spherocytes. As soon as the proportion of spherocytes reaches about 20%, there is a net decline of CFL before reaching a plateau. Due to the fact that in real spherocytosis the proportion is in the range of $15 - 20\%$, our results show that the impairment of flow is quite ample (the CFL declines by about a factor 3). Note that in microcirculations, and under healthy conditions, the hematocrit rarely exceeds 20% [14, 70, 74]. The study regarding a hematocrtit of 20% is more relevant to microcirculation.

Finally, let us note that discocytes cells ($\tau = 0.64$) migrate to the centre of the channel in microfluidic flows due to hydrodynamic lift forces that push deformable cells away from high-shear regions near the walls toward the center-line. However, spherocytes ($\tau = 0.99$), which are less deformable, are marginalized by discocytes, and are pushed against the walls, as shown in Fig. 4.10. This margination leads to a reduction of the CFL. However, when the entire suspension is made of spherocytes only, there is no margination. This explains why spherocytes flow more efficiently than a mixture of discocyes and spherocytes, leading to a minimal CFL in the range of $40 - 70\%$ of spherocytes (Fig. 4.9a). This provides a basic explanation of the non monotonic behavior of the RBC flux with the proportion of spherocytes (Fig. 4.2)

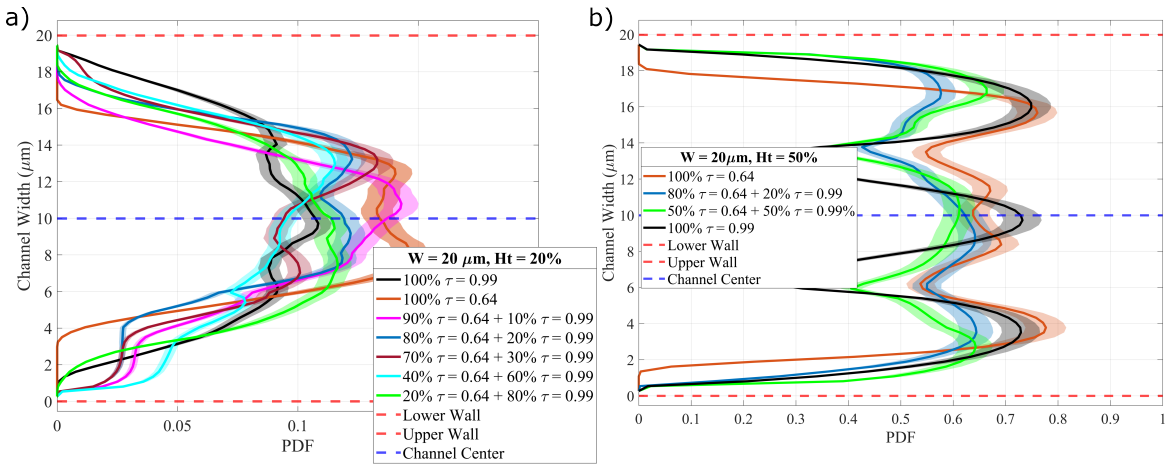

Fig. 4.8 Spatial Distribution of RBCs for different relative concentrations of healthy cells (Shaded areas represent error region), $Ca = 18$, W = 20 µm, and $\lambda = 1$. a) Ht = 20%, b) Ht = 50%.

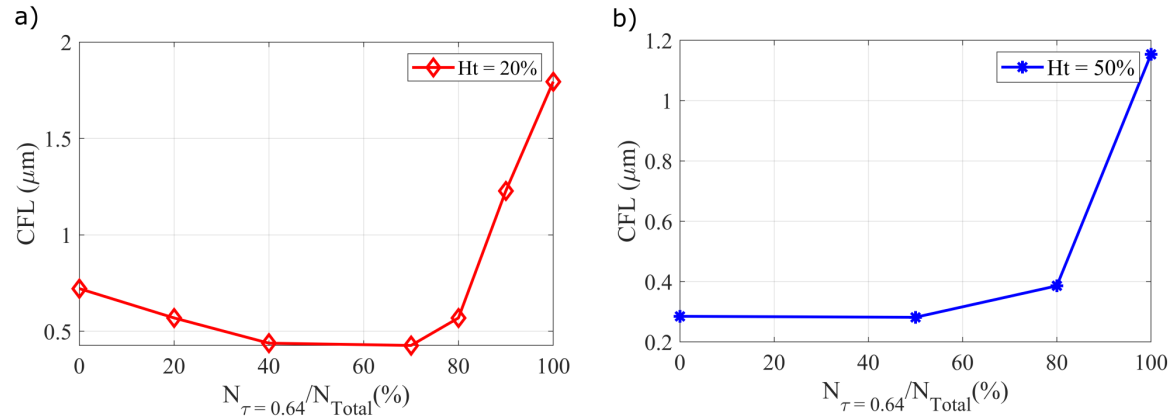

Fig. 4.9 CFL as a function of the relative concentration of healthy cells, $Ca = 18$, W = 20 µm, and $\lambda = 1$. a) Ht = 20%, b) Ht = 50%.

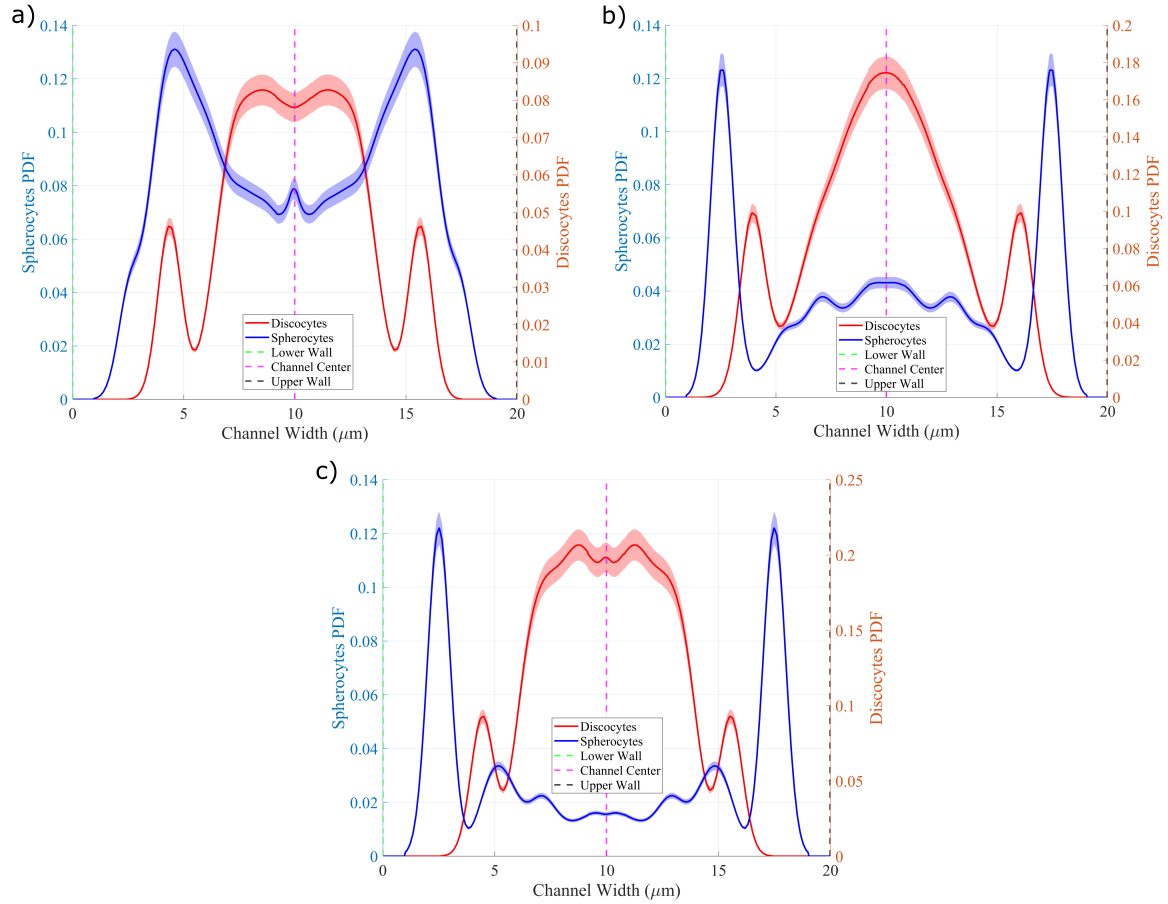

Fig. 4.10 Histogram of the probability density function of RBCs in heterogeneous case as a function of the channel width (Shaded areas represent error region), spherocytes ($\tau = 0.99$) in blue and discocytes ($\tau = 0.64$) in red, Ht = 20%, $Ca = 18$, W = 20 µm, and $\lambda = 1$. a) Mixture of 30% $\tau = 0.64$ and 70% $\tau = 0.99$, b) Mixture of 60% $\tau = 0.64$ and 40% $\tau = 0.99$ and c) Mixture of 90% $\tau = 0.64$ and 10% $\tau = 0.99$.

C. Cell-Cell Interactions

We also carried out an examination of the interactions between RBCs. The central aim of this investigation was to identify the presence of additional mechanisms (besides CFL) driving the increase of blood viscosity observed when spherocytes are added to a suspension.

Figure 4.11 presents 3D bar plots that illustrate the contact frequency observed between pairs of cells. The determination of cellular contact is predicated upon the establishment of a threshold distance that signifies the minimum proximity between cell membranes. This visualization serves as a valuable tool for examining cell-to-cell interactions and discerning patterns and trends in the frequency of contacts

between different pairs of cells. Specifically, when considering a homogeneous scenario where all cells possess identical morphological characteristics, it becomes evident that the frequency of interactions between cells is significantly lower. In contrast, when examining the case of the heterogenous case (as depicted in Fig. 4.11), it is apparent that the interaction frequency between cells is higher. This disparity in interaction frequency may provide an additional explanation for the observed rapid decline in blood flux (Fig. 4.3) and the subsequent increase in viscosity (Fig. 4.5).

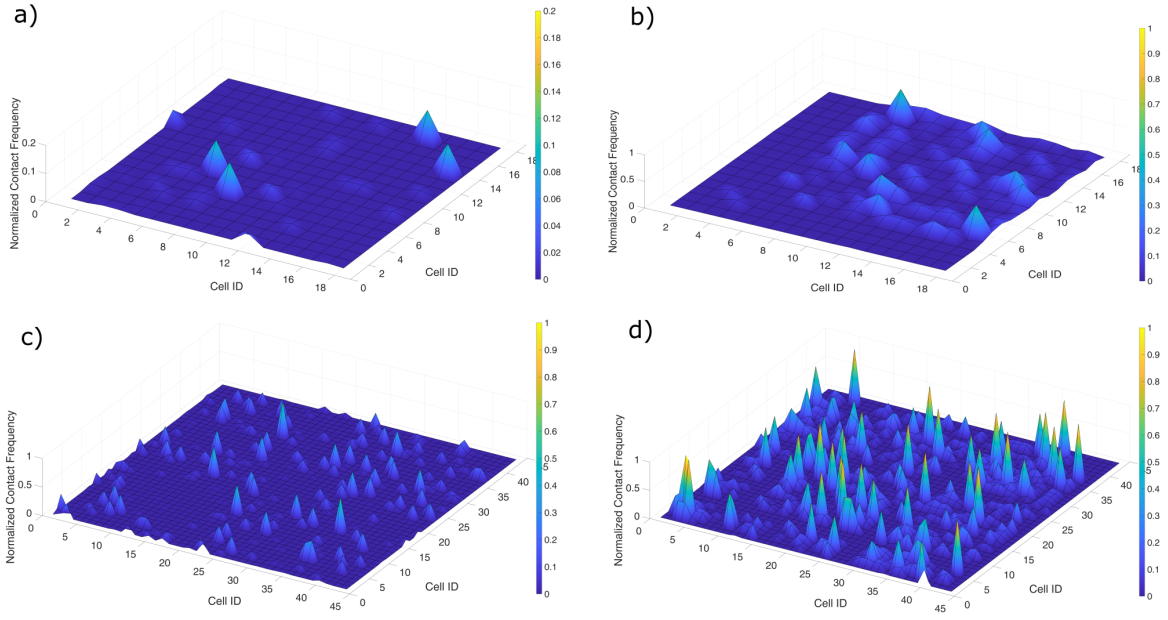

Fig. 4.11 3D bar plot depicting the contact frequency between cell pairs, $Ca = 18$, W = 20 µm and $\lambda = 1$. Subfigures a) and c) for the homogeneous case $N_{0.64}/N_{Total} = 100$, Ht = 20% and 50% respectively. Subfigures b) and d) for the heterogeneous case $N_{0.64}/N_{Total} = 20$; Ht = 20% and 50% respectively

The histogram plots displayed in Fig. 4.12 recapitulate the probability density function (PDF) for the average nearest distances between points on cell membranes, focusing on pairs of closely situated cells. These plots effectively illustrate how these average nearest distances are distributed across various ranges. A greater density of points along the y-axis at a specific distance on the x-axis signifies a higher prevalence of cell pairs with that average nearest distance. Shorter average nearest distances between cell pairs may indicate stronger or more frequent interactions, a pattern observed in cell mixtures with a specific example ratio of $N_{0.64}/N_{Total} = 20$. Conversely, larger average nearest distances might imply weaker or less frequent interactions, particularly noticeable when the ratio of $N_{0.64}/N_{Total}$ is 100.

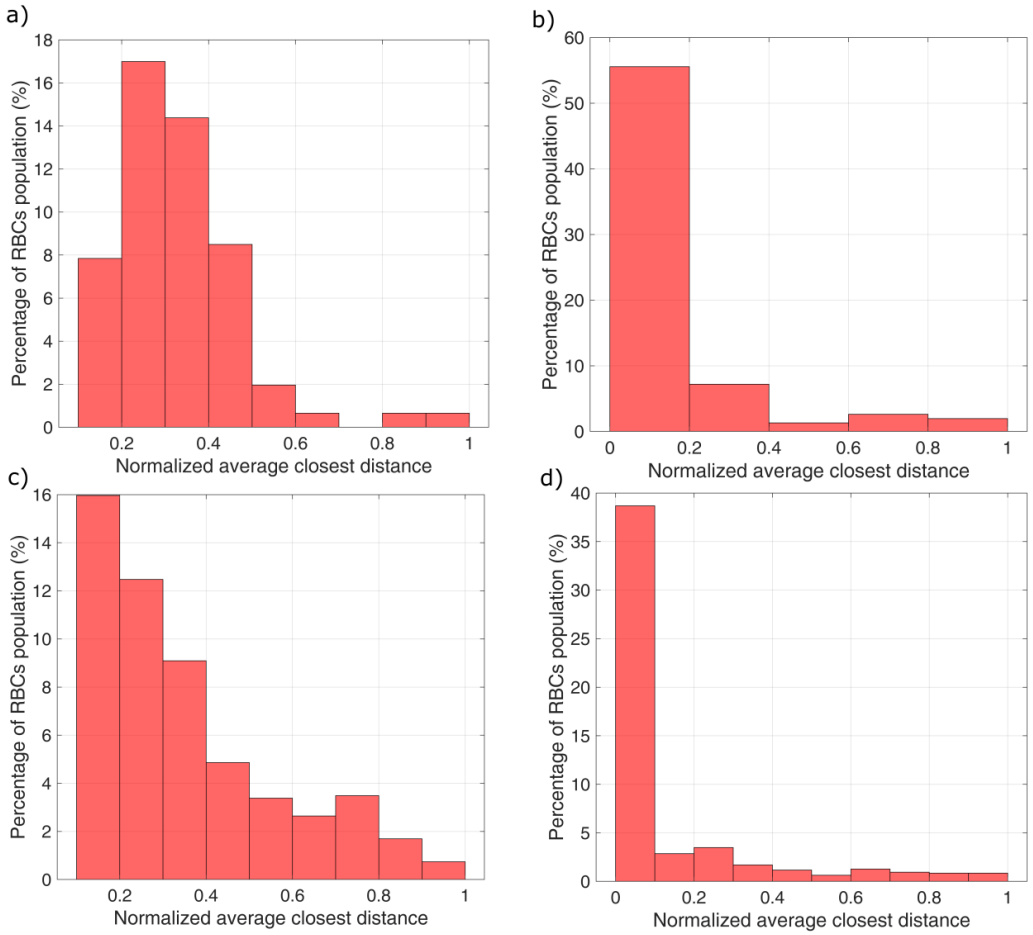

Fig. 4.12 Histogram plot displays the probability density function (PDF) of the average closest distances between each cell pair. Subfigures a) and c) for the homogeneous case, Ht = 20% and 50% respectively. Subfigures b) and d) for the heterogeneous case $N_{0.64}/N_{Total} = 20$; Ht = 20% and 50% respectively.

4.4 conclusion

This study comprehensively investigated the effects of spherocytosis on blood rheology and flow dynamics using numerical simulations. Our simulations covered a range of scenarios, from no spherocytosis to 100% prevalence within the blood flow. We investigated the interaction between spherocytic RBCs and healthy discoid RBCs, using a reduced area parameter ($\tau = 0.64$) to represent healthy cells.

The study yielded significant insights. The introduction of spherocytic RBCs resulted in a significant decrease in flux, particularly when spherical cells were present in the mixture. The decrease in flow dynamics was caused by enhanced cell-cell contact, leading to differences in cell shapes and velocities, as well as increased intercellular

collisions. This resulted in a smaller CFL, which, in turn, increased the effective blood viscosity, ultimately reducing the RBC flux.

Furthermore, our simulations identified a crucial concentration range (20% to 40%) at which the flow of RBCs reached its lowest point. This highlights the considerable impact of the diverse composition of blood, including cells of different shapes, on the dynamics of flow. This is also illustrated by the emergence of a minimal CFL for spherocytes concentration of about 20%-40%, showing that 100 % of spherocytes yields a larger flux than having just a proportion of about 20%-40% of spherocytes. This has further been illuminated by the fact that a hetergenous suspension leads to a margination of spherocytes.

Additionally, our study examined the impact of spherocytosis on effective viscosity. Our findings indicated that the presence of spherocytes resulted in elevated viscosity. The inflexibility and limited ability to change the shape of spherocytes were determined to be significant factors that contribute to increased frequency of collisions and heightened resistance to flow.

In summary, our study provides a thorough understanding of the intricate rheological properties of blood in spherocytosis. However, this work has at least two limitations: (i) it is focused on a 2D setup and a full 3D simulation is necessary to present a more realistic quantitative estimate of the impact of spherocytosis on blood flow. Nevertheless, we believe that the trend reported here should survive in 3D as well, albeit with different quantitative effects. (ii) These results are obtained in a simple geometry in order to decipher the basic phenomena, and a systematic study must be undertaken in realistic vascular networks with the aim to deliver a more relevant message for in-vivo blood flow.

Chapter 5

Red Blood Cells sphericity and network architecture influence lingering and partitioning

Note: This work is in the final stage to be submitted.

5.1 Introduction

The dynamics of red blood cells within the architecture of the circulatory system lead to the emergence of lingering red blood cells.

The circulatory system, with its hierarchical structure of vessels ranging from large arteries to capillaries, presents many caspects which challenge our current understandings. Among these, the behavior of RBCs within this complex network is highly important. RBCs are not simple carriers of oxygen; their behavior, flexibility, and aggregate formation significantly regulate vascular blood flow, and therefore the distribution of oxygen throughout the body [92]. It has been suggested from recent studies that RBCs possess a "memory effect"—that is, their past experiences within the vascular network, including shear exposure and passing through narrow capillaries or interacting with the endothelium, might influence their future behavior and distribution [68, 66].

The concept of cellular memory, traditionally associated with immunological responses or epigenetic modifications, is thus extended to the biomechanical realm, proposing that RBCs can "remember" their mechanical interactions and adjust their properties in response [109]. Our objective is to investigate if the memory of RBCs

could also influence their microcirculation and especially if it leads to increased lingering of RBCs in specific regions of the network (apex of the bifurcations), which could be affecting tissue oxygenation and the efficiency of metabolic waste removal. Furthermore, the partitioning of RBCs—how they are distributed and rerouted at vascular bifurcations—could also be influenced by this memory, with significant implications for the understanding of microcirculatory disorders, and which can also help the design of artificial blood substitutes or microfluidic devices for biomedical applications.

The partitioning law or the Zweifach-Fung effect, named after the first researchers who described it, addresses the non-uniform distribution of blood components at vascular bifurcations. According to this effect, the partitioning of RBCs in microvascular networks is not solely determined by flow rates but is also influenced by the diameter of the daughter vessels relative to the mother vessel (figure 5.1.a)) [30]. So here come two different types of partitioning: Classical partitioning which refers to the expected, or "normal," distribution of RBCs at a bifurcation, where the majority of RBCs follow the path of higher flow (figure 5.1.a)). In this scenario, RBCs tend to enter the daughter vessel that carries a greater fraction of the total flow emanating from the parent vessel (see table 5.2). This behavior is intuitive, given that the fluid dynamics at the bifurcation naturally guide more cells into the branch with higher flow velocity, assuming other factors such as vessel diameter and hematocrit levels are constant. The classical partitioning effectively ensures that areas of higher demand, indicated by higher blood flow, receive a proportionately greater supply of RBCs and, consequently, oxygen. Reversed partitioning, on the other hand, describes a less intuitive phenomenon where RBCs preferentially enter the daughter vessel with lower flow (see table 5.2), contrary to what classical partitioning would predict. This reversal can occur under certain conditions, such as when the diameter of the daughter vessel with lower flow is significantly larger than that of the vessel with higher flow, or when specific microcirculatory conditions alter the usual behavior of RBCs, leading them to distribute in a manner that deviates from the expected flow-based partitioning. Reversed partitioning is particularly interesting because it suggests a mechanism by which the circulatory system can redistribute RBCs to areas that might not be receiving adequate perfusion based solely on fluid dynamics. This phenomenon can play a crucial role in situations where tissue demands change rapidly, such as during exercise or in response to injury, ensuring that oxygen delivery is optimized across the vast and variable landscape of the body's microvascular networks.

Lingering of RBCs refers to the prolonged retention or slow transit of red blood cells within the bifurcation apex of the microvascular network (see figures 5.1.d). This

behavior contrasts with the expected swift passage of RBCs, driven by the pressure and flow dynamics typical of healthy circulation. Lingering can result from a variety of factors, including vascular architecture, RBC deformability, local hematocrit variations, and the presence of biochemical signals within the microenvironment [96, 57].

There are many factors Influencing RBC lingering, like vascular geometry and network complexity: where the design of the microvascular network, including vessel diameter, bifurcation angles, and network density, can significantly impact RBC transit times. Areas with high tortuosity or complex branching may promote lingering by creating regions of low shear stress or flow stagnation [94, 57]. For example, in the case of RBC deformability, their very flexible nature allows them to navigate the narrow capillaries and bifurcations. However, changes in RBC deformability, due to disease or aging, can hinder their ability to move efficiently through the microvasculature, leading to increased retention in certain areas. The variations in local hematocrit levels, also influenced by the partitioning behavior at bifurcations and the dynamic adjustment of blood flow, can lead to heterogeneous RBC distribution and contribute to lingering, particularly in regions with reduced flow [10, 96, 57]. The microvascular endothelium secretes numerous signals that could influence the behavior of RBCs by modulating the degree of vasodilation or vasoconstriction of a vessel and the adhesiveness of RBCs to the walls. These biochemical cues can change the characteristics of local flow and transit times of RBCs [121].

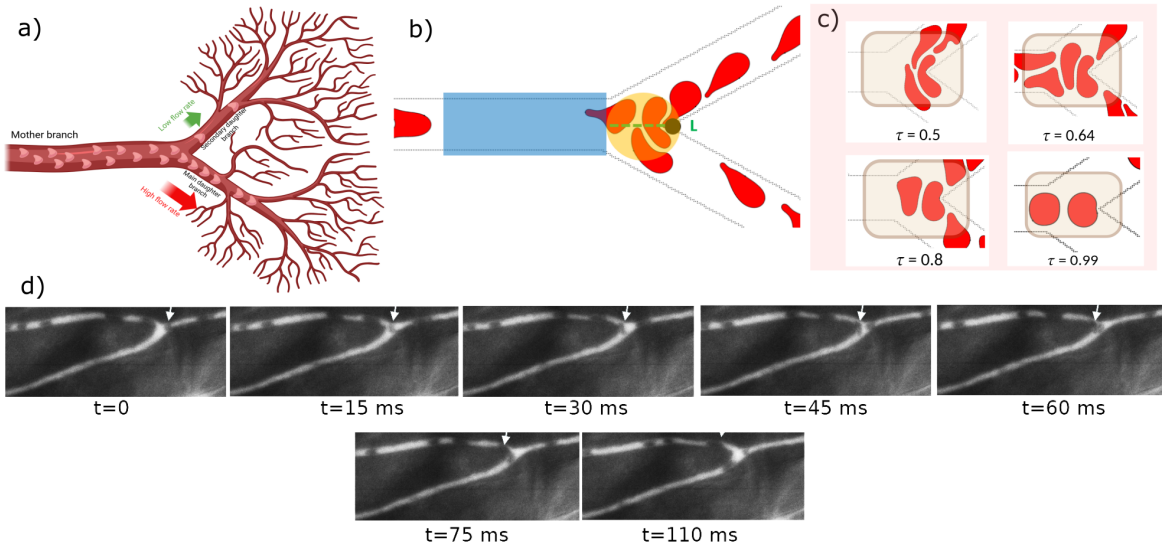

Fig. 5.1 a) A schematic of a bifurcation showing a classical partitioning, the Mother branch (M), the Main Daughter branch (MD) as the vessel collecting the highest number of RBCs and the Secondary Daughter branch (SD) as the other vessel. b) Schematic of a bifurcation example: the blue area represents the mother branch, while the intersection of this area with the daughter branches is highlighted in yellow. The reference length L is defined as the distance from the exit of the blue area to the apex of the bifurcation. c) Lingering snapshots near a given bifurcation for different reduced area. d) Lingering in a real microvascular network [97]

This chapter will consider in detail the mechanisms of the memory effect of RBCs and how it influences cell lingering and partitioning in complex vascular networks. It should be a critical analysis synthesizing recent experimental studies together with computational models on the ways red blood cells interact with the vascular environment and their behavior at the microscale. Also taken into consideration are the macroscopic consequences of such microscale behaviors with respect to the dynamics of blood flow. Therefore, this discussion would serve not only as an update of knowledge in hemorheology and vascular biology but also as a new starting point for therapeutic intervention efforts, biomimetic system development, and drug delivery and tissue engineering strategies.

5.2 Background and numerical setup

The simulation method is based on Lattice Boltzmann Method (LBM) by using a 2D geometry. The LBM is conbined with the immersed boundary method. The LBM has been described and validated in prior works [121, 61, 107, 64, 12]. For the sake of

completeness, we provide a description of the model in the supplementary materials. The validation involved also a comparison with the boundary integral method [49]. Several studies using 3D models, which include the membrane cytoskeleton, have demonstrated that the 2D model effectively replicates several shapes and flow behaviors of erythrocytes [115, 26, 95, 24].

All typical values of physical parameters used in this study and the values of dimensionless parameters are given in Table 5.1

Table 5.1 Physical and dimensionless parameters used in the simulations.

Physical Parameters	
Cell Radius R_0 (μm)	3
Membrane Bending Modulus κ (J)	3×10^{-19}
Fluid Density ρ (kg·m^{-3})	1×10^{3}
Plasma Viscosity μ_{ex} (Pa·s)	1×10^{-3}
Dimensionless Parameters	
Reynolds Number Re	0.1
Capillary Number Ca	25
Viscosity Contrast λ	6
Reduced Area τ	0.45 to 0.99

5.2.1 RBCs partitioning

To quantify the partitioning of RBCs we first calculate the fractional blood flow Q^* and the fractional RBCs flow N^* which are defined as:

$$\begin{aligned} N^* &= \frac{N_{\text{daughter1}}}{N_{\text{daughter 1}} + N_{\text{daughter 2}}} \\ Q^* &= \frac{Q_{\text{daughter 1}}}{Q_{\text{daughter 1}} + Q_{\text{daughter 2}}} \end{aligned} \tag{5.1}$$

Where $N_{\text{daughter1}}$ and $N_{\text{daughter2}}$ are the number of RBCs that cross a chosen section in the first and the second daughter branches respectively, and $Q_{\text{daughter1}}$ and $Q_{\text{daughter2}}$ are the plasma flow rates in the first and the second daughter branches respectively.

An empirical law developed by Pries [93] for this purpose of RBCs partitioning in a bifurcation describes how the fractional flow of blood and the fractional RBC flux through bifurcations are related:

Table 5.2 Identifying the partitioning type based on Q^* and N^* [10].

	$Q^* > N^*$	$Q^* < N^*$
$Q^* > 0.5$	Reverse partitioning	Classical partitioning
$Q^* < 0.5$	Classical partitioning	Reverse partitioning

$$\mathrm{N}^* = \begin{cases} 0, & \text{if } Q^* < X_0, \\ 1, & \text{if } Q^* > 1 - X_0 \\ \frac{1,}{1+e^{-\left[A+B\,\mathrm{logit}\left(\frac{Q^*-X_0}{1-2X_0}\right)\right]}}, & \text{otherwise.} \end{cases} \tag{5.2}$$

Where $\mathrm{logit}\,(x) = \ln\left(\frac{x}{1-x}\right)$, A, B and X_0 are related to the geometry of bifurcation and hematocrit Ht:

$$A = \frac{-6.96}{D_M} \times \ln\left(\frac{D_{MD}}{D_{SD}}\right), B = 1 + 6.98\left(\frac{1-H_M}{D_M}\right), \quad X_0 = 0.4/D_M, \tag{5.3}$$

Where H denotes the measured Ht, the subscripts indicate the vessel in which the quantity is being considered.

To quantify the deviation from the Zweifach-Fung prediction, we calculated the deviation d_{ZF} from the theoretical prediction using Eq.(5.2) as the relative difference between this prediction and our simulation [97]:

$$d_{ZF} = |\Delta {N^*}_{SIM} - \Delta {N^*}_{ZF}| \tag{5.4}$$

We note that ΔN^* is the difference in fractional erythrocyte flow rates between the main daughter vessel (MD) and the secondary daughter vessel (SD), and the expressions SIM and ZF refer to the simulations and the empirical prediction (using Eq.(5.2)), respectively:

$$\Delta N^* = {N^*}_{MD} - {N^*}_{SD} \tag{5.5}$$

5.2.2 RBCs lingering

The calculation method to determine the lingering strength, as described in previous research [15], is briefly summarized here for completeness. To quantify lingering, a relative residence time, Pe_L, was defined as the normalized time an RBC spends at the intersection between the mother branch and the two daughter branches (highlighted in yellow in Fig. 5.1.b):

$$Pe_L = \frac{t_{r,RBC}}{t_{ref}}, \tag{5.6}$$

where $t_{r,RBC}$ is the residence time of a specific RBC at the yellow intersection, and $t_{ref} = \frac{L}{V_M}$ is the reference time required for an RBC to travel the reference length L (from the exit of the ROI of the mother branch (blue area) to the apex and then to the entry of the daughter branches; Fig. 5.1.b)) with a velocity equal to the mean velocity at the exit of the mother branch (V_M).

This definition is similar to the lingering Péclet number defined by Rashidi et al. [97], except that it is a cell-based definition rather than a statistical estimation based on the probability density function of RBC velocity. This approach was also tested in our simulations, yielding similar trends (See supplementary materials). As in [15], an RBC is considered to be lingering if $Pe_L \geq 2.0$.

5.2.3 Geometries

In this investigation, we used two different complex geometries (Fig. 5.2) with multiple bifurcation levels. In the first complex geometry extracted from a cat mesentery as depicted in Figure 5.2.a and adopted from [9], there are three levels of bifurcations in series from an arteriole to capillaries and then the confluence of the capillaries into a venule. In total, this network comprises 14 bifurcations and 22 vessels. The radii of the smallest capillary and feeding artery are $7\mu m$ and $20\mu m$, respectively.

The second network in Fig. 5.2.b that we generated consists of four levels of bifurcations, having approximately 15 bifurcations and 32 vessels in total. The width of all vessels is uniform, around $8.4\mu m$. Unlike the first network, which has asymmetric branching, the geometry of each bifurcation in the second network is symmetric. We note that the hematocrit is set to 20% and the capillary number to 25, while the viscosity contact for the RBCs is 6.

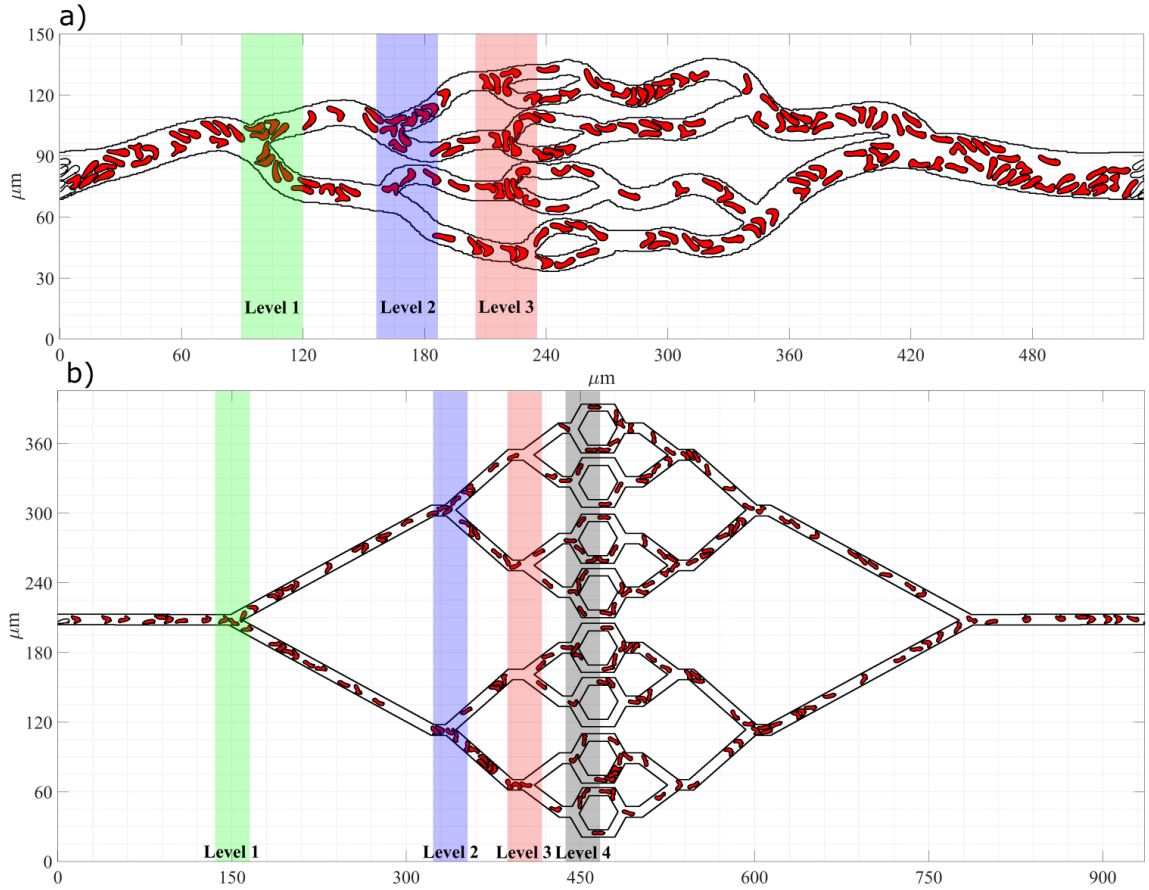

Fig. 5.2 a) Complex geometry extracted from cat mesentery with 3 bifurcation levels taken from [9]. b) Complex symmetric geometry with 4 bifurcation levels.

5.3 Results and discussion

5.3.1 Lingering and Deviation from Zweifach-Fung Across Network Levels for Normal Cells

Figure 5.3 presents boxplots of two key metrics—the lingering Péclet number, Pe_L, and the deviation from the Zweifach-Fung prediction, d_{ZF}—as functions of the bifurcation level in two different microvascular networks. Subfigures (a) and (b) correspond to the first network (three levels), while (c) and (d) correspond to the second, more symmetric network (four levels). The "bifurcation level" (Level 1, Level 2, etc.) indicates how far downstream (or upstream in case of confluence) a given branch is from the main feeding vessel.

A. Lingering Péclet Number (Pe_L)

In Figure 5.3(a), the average lingering Péclet number Pe_L increases notably from Level 1 to Level 3. Specifically, we observe median values around 1.7 at Level 1, increasing to ~ 1.9 at Level 2, and exceeding 2.2 at Level 3. This trend indicates that red blood cells (RBCs) tend to spend increasingly more time in the apex region of each bifurcation as they progress deeper into the network. A similar pattern emerges in Figure 5.3(c), where Pe_L rises from ≈ 1.8 at Level 1 to over 2.6 at Level 4 in the second, symmetric network. This systematic rise in lingering is consistent with the notion of an RBC "memory effect," wherein cells' past deformation and apex interactions at upstream bifurcations alter their dynamics in subsequent levels [96, 15].

B. Deviation from the Zweifach-Fung Law (d_{ZF})

Figures 5.3(b) and (d) show the boxplots of d_{ZF}, which quantifies the difference between the simulated RBC flux distribution and the classical Zweifach-Fung prediction [30]. In both networks, the deviation d_{ZF} grows with each additional bifurcation level. For the first network [Fig. 5.3(b)], d_{ZF} increases from around 0.05 (Level 1) to 0.15 (Level 2) and surpasses 0.20 at Level 3. In the second network [Fig. 5.3(d)], d_{ZF} increases substantially from nearly 0 at Level 1 to around 0.6 at Level 4. This indicates that standard partitioning laws become less accurate further into the microvascular network, likely due to the compounded effects of RBC lingering, altered flow rates, and RBC deformability [66, 10].

Overall, these boxplots show that both lingering and deviation from the classical Zweifach-Fung law are significantly amplified in deeper levels of branching.

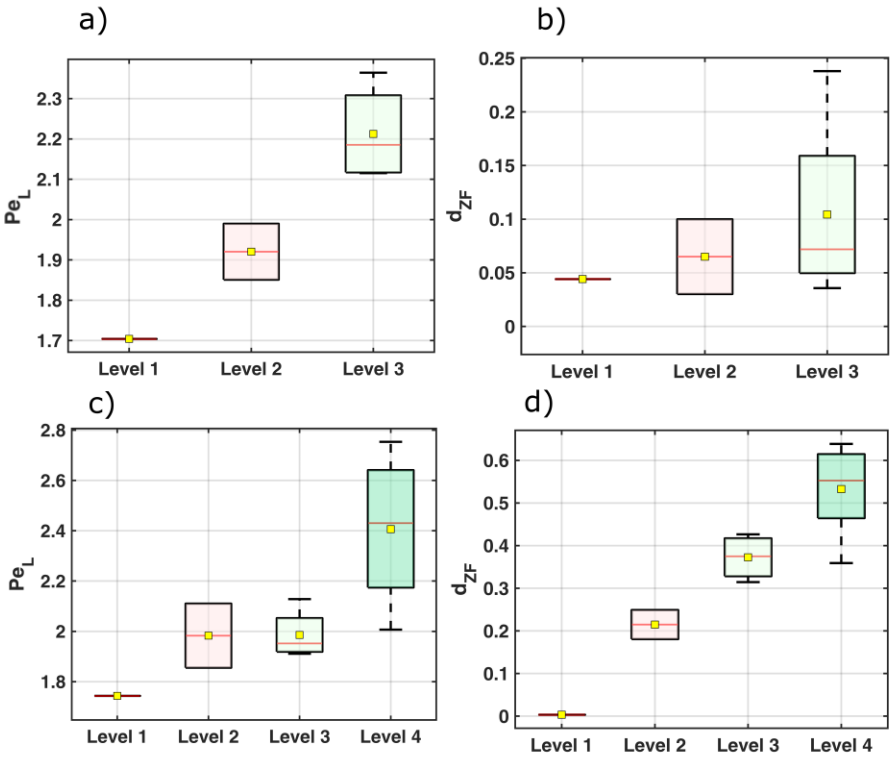

Fig. 5.3 Boxplots for normal cells ($\tau = 0.64$) of (a) Pe_λ (lingering Péclet number) and (b) d_{ZF} (deviation from Zweifach-Fung) in the asymmetric network with three levels, and (c) Pe_L and (d) d_{ZF} in the symmetric network with four levels. Boxes show the interquartile range (IQR), the red lines indicate the median, and the squares indicate the mean value at each level.

5.3.2 Symmetric Network Analysis and the Role of RBC Memory

In the previous section, we established that RBC lingering and deviations from the Zweifach-Fung prediction grow with each successive bifurcation. However, because the original mesenteric network in Fig. 5.2(a) includes both geometric asymmetry and vessel tapering (Halving vessel widths after each bifurcation), it remains unclear whether these trends stem primarily from the network's design or from an intrinsic "memory effect" of the RBCs. To disentangle these factors, we constructed a purely symmetric network with constant vessel width (Fig. 5.2(b)). By comparing RBC behavior in these two extreme cases (an asymmetric, tapering network vs. a fully symmetric, constant-width network), we can determine whether RBC memory alone is sufficient to produce the growing lingering and partitioning deviations observed at each successive bifurcation.

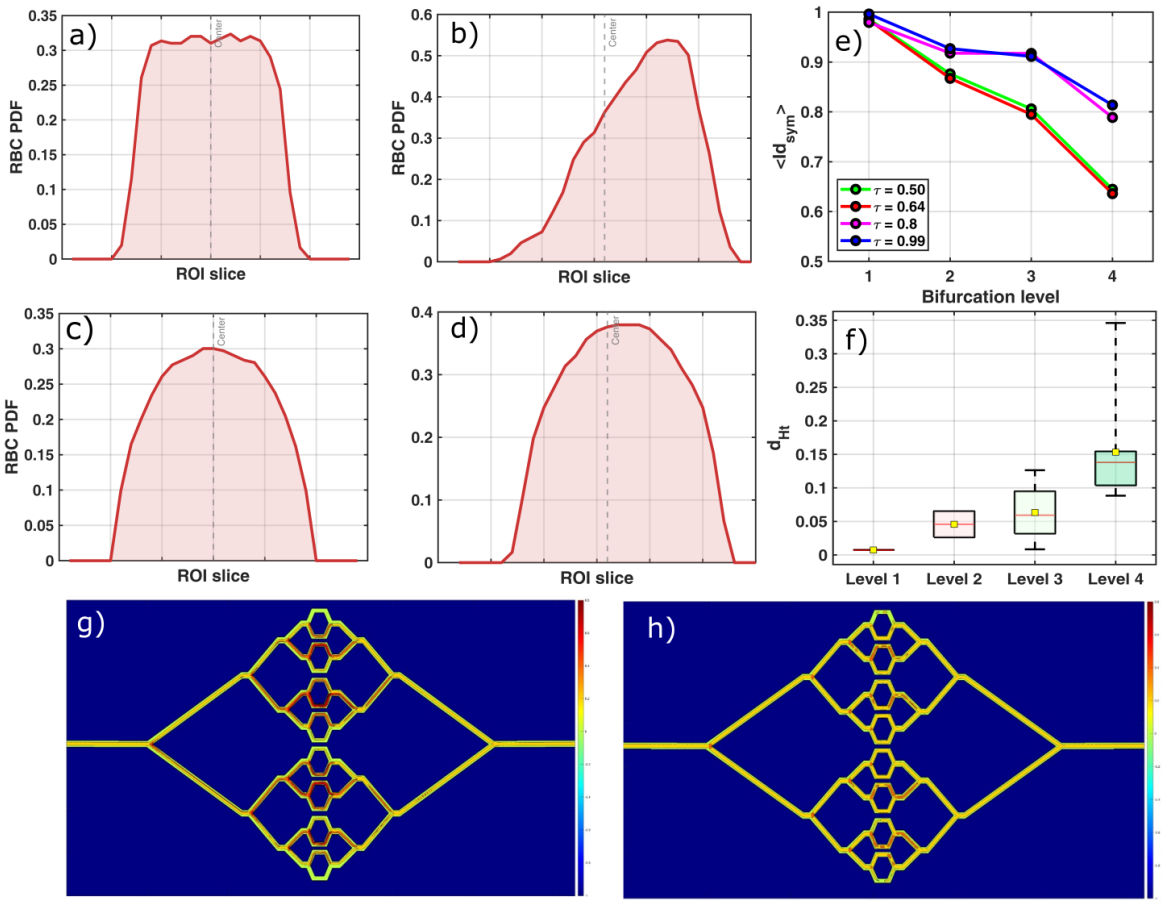

Fig. 5.4 (a) Probability density function (PDF) of RBCs across the width of the mother branch (ROI slice) in the *first* bifurcation level of the *symmetric network* for $\tau = 0.64$. (b) Same PDF measurement for the *fourth* level at $\tau = 0.64$. (c) PDF in the *first* level for $\tau = 0.99$. (d) PDF in the *fourth* level for $\tau = 0.99$. (e) Average symmetry index $\langle Id_{\text{sym}} \rangle$ of the RBC PDF versus bifurcation level for different reduced areas τ in the symmetric network. (f) Differences in hematocrit (d_{Ht}) between each pair of daughter vessels, also across the four bifurcation levels of the symmetric network. (g) Global distribution of RBCs ($\tau = 0.64$) in the entire symmetric network, with color indicating RBC concentration. (h) Same global distribution for $\tau = 0.99$.

A. RBC Probability Density and Symmetry Index

Figures 5.4(a)–(d) illustrate the RBC probability density function (PDF) measured in a transverse slice of the mother branch, just upstream of a bifurcation, for two different values of the reduced area τ (0.64 and 0.99) and at two different levels (1st vs. 4th). As τ decreases (i.e., the RBC becomes more elongated), the PDF becomes increasingly asymmetric near the channel centerline, suggesting that radial drift and apex interactions encountered in the previous bifurcations are actively biasing the

RBC distribution. Even in this purely *symmetric* geometry, RBCs exhibit gradually increasing asymmetry as the level number grows, pointing to a mechanical memory effect intrinsic to the RBCs rather than a mere byproduct of geometric asymmetry.

To quantify this effect, we define a spatial symmetry index,

$$Id_{sym} = 1 - \frac{\text{MAE}}{\text{Data Range}}, \tag{5.7}$$

where MAE is the mean absolute difference between the PDF values and their mirrored counterparts across the channel's centerline, and *Data Range* is the difference between the data minimum and maximum. As shown in Fig. 5.4(e), $\langle Id_{\text{sym}} \rangle$ decreases markedly with each subsequent bifurcation level for all examined reduced areas. This indicates that the RBC distribution becomes less symmetric as cells progress through the network. Elongated cells (e.g., $\tau = 0.50$ and $\tau = 0.64$) exhibit stronger asymmetry shifts than their more spherical counterparts (e.g., $\tau = 0.99$) orbut near-spherical RBCs (e.g., $\tau = 0.80$).

B. Hematocrit Differences and Deviations at Symmetric Bifurcations

In Fig. 5.4(f), we track the absolute difference in hematocrit, d_{Ht}, between each pair of daughter vessels at bifurcations. Similar to the findings in Fig. 5.3, the inter-branch hematocrit difference increases with the bifurcation level, further confirming that the RBC distribution is progressively altered by upstream events. Consequently, these differences persist and amplify in downstream vessels, contributing to increased lingering and deviations from Zweifach-Fung prediction.

C. Global RBC Distribution and Plasma Skimming

The overall RBC distributions for $\tau = 0.64$ and $\tau = 0.99$ are shown in Fig. 5.4(g) and 5.4(h), respectively. In both cases, the majority of RBCs concentrate around the channel center, while near-wall regions show reduced hematocrit—a form of plasma skimming. In addition, these plots reveal that RBCs with a lower reduced area (more elongated shape) develop pronounced localized aggregations or "hotspots" at successive bifurcation levels, likely from the cumulative radial drift and apex interactions. As a result, even in a perfectly symmetric geometry with constant vessel widths, RBC distributions become increasingly imbalanced downstream.

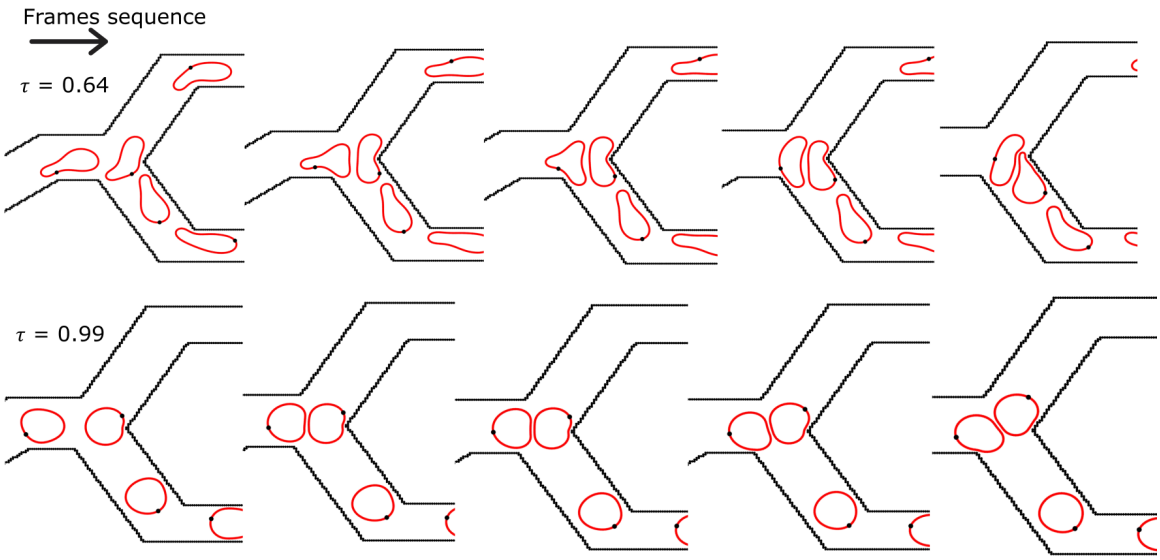

Fig. 5.5 Lingering snapshots for normal cells and spherical cells the bifurcation

D. Discussion: Geometry vs. Memory Effects

Comparing these results with the previous asymmetric geometry (Fig. 5.2(a)) makes it evident that the increasing lingering effects and deviations from Zweifach-Fung predictions are *not* solely the consequence of geometric asymmetry or vessel shrinking. Instead, these phenomena persist in the symmetric network and even intensify through successive bifurcation levels, strongly supporting an RBC "memory" mechanism. This memory stems from the repeated deformations and apex interactions that RBCs undergo, causing incremental shifts in their radial position and leading to asymmetric PDFs (Figs. 5.4(a)–(d)) and greater hematocrit imbalance between daughter branches (Fig. 5.4(f)).

Overall, we observed that, while local geometry can modulate RBC partitioning, the long-range memory effect (i.e trajectory history) is an essential driver of non-classical RBC distributions. Both elongated ($\tau = 0.50$) and spherical ($\tau = 0.99$) cells exhibit these cumulative deviations, but the effect is notably more pronounced for deformable, elongated RBCs. This observation supports the hypothesis that higher lingering and deviation observed in experimental data, particularly in in-vivo studies [96], are due to the fact that the region of interest (ROI) is part of a larger network where the flowing RBCs have already traversed many bifurcations, accumulating more memory. As RBCs navigate through the complex network of bifurcations, they experience various mechanical forces and shear stresses that can induce lasting deformations, impacting their ability to transport oxygen and navigate capillaries effectively.

5.3.3 Lingering Trends in Asymmetric and Symmetric Networks

Figure 5.6 compares lingering behavior in both the asymmetric and symmetric networks. Subfigures 5.6(a)–(d) show bin-scatter plots of the lingering Péclet number Pe_L (vertical axis) as a function of D_L, the minimum distance of an RBC to the apex region (horizontal axis), for various reduced areas (τ) in the *asymmetric* network. Analogous data for the *symmetric* network appear in subfigures 5.6(e)–(h). In each bin, the color scale indicates the fraction of RBCs that exhibit a particular (D_L, Pe_L) pairing.

A. Impact of Apex Proximity on Lingering. In both networks, cells closer to the bifurcation apex ($D_L \lesssim 2\,\mu$m) have a higher probability of lingering ($Pe_L \geq 2$). This trend is especially pronounced for cells with smaller reduced areas ($\tau \leq 0.64$), which are more elongated and can more easily "hook" onto the apex boundary. Even spherical RBCs ($\tau = 0.99$) show elevated Pe_L values when D_L is very small, but as discussed in Sec. 5.3.4, their main lingering mechanism is blockage events rather than strong apex hooking.

B. Proportion of Lingering RBCs vs. Bifurcation Level. In Figs. 5.6(i)–(j), we plot the fraction of RBCs with $Pe_L \geq 2$ (i.e., those classified as lingering cells) as a function of bifurcation level for the asymmetric and symmetric networks, respectively. Across all reduced areas τ, the proportion of lingering cells rises with each subsequent level, consistent with the cumulative "memory" effect reported earlier [97, 15]. Notably, even in the symmetric network [Fig. 5.6(j)], where geometric biases are minimized, the fraction of lingering cells still increases level by level. This underscores that apex interactions and progressive radial drift—rather than strictly geometry—are key drivers of lingering.

C. Average Lingering Intensity. Figures 5.6(k)–(l) display the average lingering $\langle Pe_L \rangle$ in each network as a function of bifurcation level. In both networks, $\langle Pe_L \rangle$ increases with level, confirming that RBCs not only linger more frequently, but also remain longer in downstream bifurcations. This finding is aligned with previous experimental findings that highlight how red blood cells can accumulate deformations and positional biases over multiple branching events [66, 92, 15, 78].

D. Comparison Between Asymmetric and Symmetric Networks. Although the baseline lingering is somewhat higher in the symmetric network [Figs. 5.6(e)–

(h)]—likely due to there are more bifurcation levels, vessel diameter, and branching angles—the overall trend of increasing Pe_L and rising proportion of lingerers is qualitatively similar in the symmetric network. This corroborates the idea that local geometry is not the sole factor. Instead, RBC memory and repeated interactions with the apex appear to be the dominant mechanism driving sustained lingering effects.

In summary, Fig. 5.6 reinforces that RBCs with lower reduced areas linger more often and more intensely, but *all* RBCs, including near-spherical ones, exhibit increasing lingering over successive bifurcations. The memory-driven accumulation of slight apex interactions emerges as a robust factor influencing microcirculatory blood flow, even in anatomically idealized (symmetric) networks.

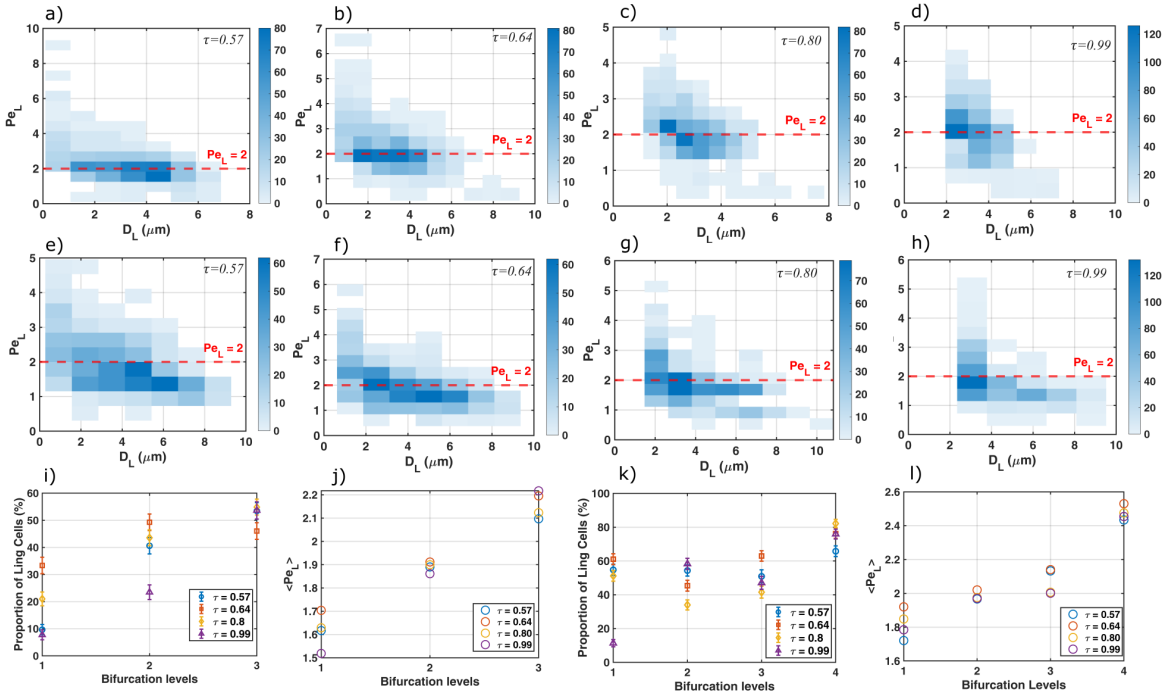

Fig. 5.6 Binscatter plots of the RBC lingering Péclet number (Pe_L) versus the minimal distance from the bifurcation apex (D_L) for various reduced areas: (a)–(d) show results in the asymmetric network, while (e)–(h) show results in the symmetric network. Panels (i) and (k) present the proportion of RBCs classified as lingerers ($Pe_L \geq 2$) at each bifurcation level in the asymmetric and symmetric networks, respectively. Finally, (j) and (l) depict the mean lingering $\langle Pe_L \rangle$ across bifurcation levels for the asymmetric and symmetric networks, respectively.

5.3.4 Lingering Behavior of Spherical RBCs

Although one might expect spherical RBCs (e.g., $\tau = 0.99$) to traverse bifurcations without lingering, our simulations reveal that these cells can still experience prolonged residence times in the apex region. Two main factors explain this phenomenon:

A. Mild Deformation Due to Flexibility. Even "spherical" RBCs in our model retain a certain degree of flexibility because the capillary number $Ca = 25$ corresponds to flexible cells. Figures 5.7(e)–(h) illustrate that, despite having an equilibrium (relaxation) diameter of about $6\,\mu$m, the RBCs' *minimum* diameter can decrease to $\sim 5.5\,\mu$m and their *maximum* diameter can rise to $\sim 6.5\,\mu$m by the fourth bifurcation level. This slight but non-negligible deformation implies that the RBC membrane still interacts strongly with the bifurcation apex, imparting sufficient friction or tethering to increase the cells' local residence time.

B. Apex Geometry and Multi-Cell Blockage. In addition to membrane flexibility, the local geometry of the bifurcation apex (the "lingering triangle" shown in Figs. 5.7(b) and 5.7(f)) shrinks significantly in higher levels. As seen in Table 5.3, the triangle side lengths (e.g., "Side 2" and "Side 3") decrease from $11\,\mu$m at Level 1 to $7.5\,\mu$m at Level 4, reducing the available cross-section through which RBCs can pass. Even when considering a spherical RBC with a maximum diameter of $\sim 6.5\,\mu$m, the proximity in size can result in transient blockages. Moreover, when *two* such cells attempt to cross simultaneously (Fig. 5.7(f) snapshot), their combined "footprint" can exceed $12\,\mu$m, effectively halting flow and prolonging the residence of any RBCs upstream (See Fig. 5.5 for spherical RBCs). Consequently, local RBC concentration increases and self-organized blockage events become more probable, leading to higher lingering times.

For elongated RBCs (Figs. 5.7(a)–(d)), the minimal diameter can drop to 3–4 μm, providing an alternative reason for lingering: cell edges can temporarily "hook" onto the apex, but overall geometric blockage is less likely because their narrow dimension slips around the bifurcation more easily. In contrast, spherical RBCs rely less on physical hooking and more on crowding/blockage events, though both cell types display some degree of apex interaction and resulting residence.

Overall, these show that apex lingering is not limited to elongated RBCs; spherical cells also exhibit measurable lingering when sufficiently flexible and when apex dimensions are restrictive. The interplay between slight shape deformation and tight

apex geometry can slow or block local flow, resulting that a higher RBC "memory" and apex interactions remain relevant across a range of reduced areas τ.

Table 5.3 Bifurcation triangle areas and side lengths at each level.

	Level 1	**Level 2**	**Level 3**	**Level 4**
Side 1 (μm)	8.4	8.4	8.4	8.4
Side 2 (μm)	11	9.3	10	7.5
Side 3 (μm)	11	9.3	10	7.5
Triangle Area (μm^2)	42.70	34.85	38.12	26.10

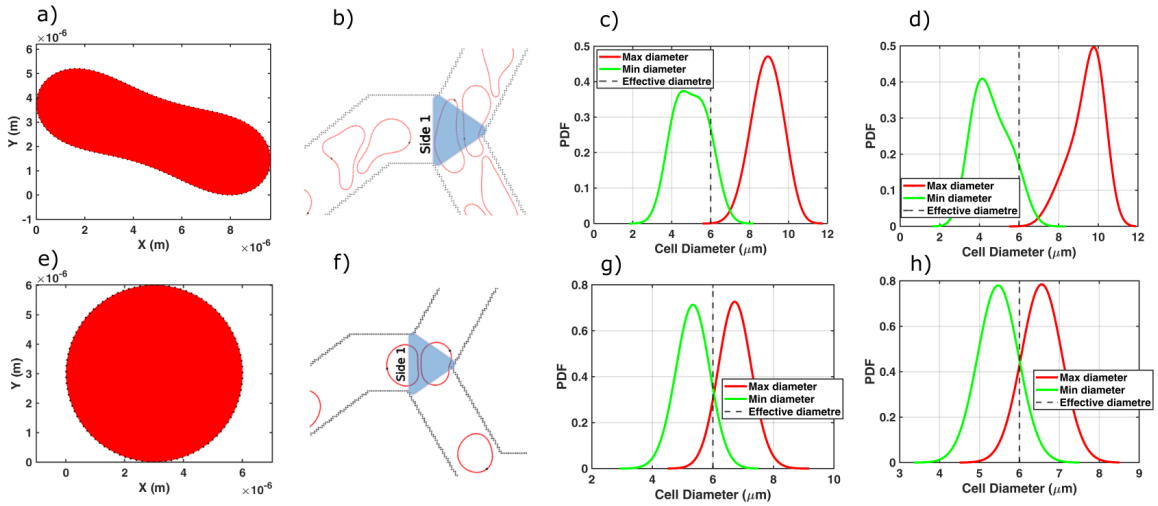

Fig. 5.7 (a) Relaxation shape of an RBC with $\tau = 0.64$. (b) The "lingering triangle" region, where the first side equals the vessel diameter, and a snapshot of two lingering RBCs with $\tau = 0.64$. (c) Probability density function (PDF) of the maximum and minimum cell diameters in the bifurcation region for $\tau = 0.64$ at the *first* bifurcation level. (d) The same PDF for $\tau = 0.64$ at the *fourth* bifurcation level. (e) Relaxation shape of an RBC with $\tau = 0.99$. (f) The lingering triangle region and a snapshot of two RBCs with $\tau = 0.99$. (g) PDF of the maximum and minimum cell diameters in the bifurcation region for $\tau = 0.99$ at the *first* bifurcation level. (h) The same PDF for $\tau = 0.99$ at the *fourth* bifurcation level.

5.3.5 Sphericity Effect on Lingering and RBC Partitioning

A key question is how the shape of RBCs—quantified here by the reduced area, τ—affects both their lingering (Pe_L) and their partitioning behavior relative to the classical Zweifach-Fung law. Figure 5.8 compares the lingering Péclet number (Pe_L) to the deviation d_{ZF} across a range of τ values in both the asymmetric and symmetric

networks. In each subplot, a linear regression line illustrates the general trend between Pe_L and d_{ZF}.

A. Correlation Between Lingering and Deviation. For highly elongated RBCs (lower τ, e.g., $\tau = 0.57$), we observe a noticeable positive correlation: increases in Pe_L tend to accompany larger values of d_{ZF}. That is, cells that linger more strongly at the bifurcation apex also deviate more from the classic Zweifach-Fung prediction, likely because their prolate shape enhances apex interactions and bias in downstream partitioning. As τ increases (e.g., $\tau = 0.64$ and $\tau = 0.80$), the correlation remains evident, indicating that near-spherical RBCs still exhibit a link between lingering and partitioning deviations, though the slope of the linear regression may be slightly different. Even at $\tau = 0.99$, where RBCs are spherical, there is a non-negligible rise in d_{ZF} with increasing Pe_L, underscoring that membrane flexibility and apex collisions, rather than pure elongation, drive these cumulative effects [92, 97], We should also note that this correlation may be influenced by other factors, such as the shape of the bifurcation, the angles, or previous interactions between the cells before crossing the bifurcation apex, or other mechanisms that are not discussed here or are still unclear to us. This can be observed at certain points, for example in Figure 5.8.a and Figure 5.8.b —especially for elongated cells in the asymmetric network—where we observe higher lingering but lower d_{ZF}.

B. Universality Across Geometries and Shapes. These observations dovetail with the results in Sec. 5.3.3, where we found that both lingering and d_{ZF} increase with bifurcation level regardless of whether the network is asymmetric or perfectly symmetric. Figures 5.6 and 5.7 further confirm that this rise is nearly universal across all tested reduced areas τ. In other words, while lower τ (more elongated cells) generally exhibit stronger apex hooking and higher d_{ZF} at each level, even RBCs close to spherical show incremental lingering and partitioning deviations after multiple bifurcations. Consequently, RBC "memory" appears to be robust to shape variations: once a cell begins to drift or deform at upstream bifurcations, its downstream distribution remains altered.

C. Implications for Microcirculatory Flow. These findings collectively suggest that sphericity modulates but does *not* eliminate memory-driven lingering and partitioning anomalies. In clinical or physiological contexts, mildly deformed RBCs (e.g., in certain pathologies) may still exhibit marked accumulations in apex regions,

reducing capillary perfusion efficiency and promoting localized oxygen delivery heterogeneities [109, 68]. Meanwhile, even near-spherical cells can form transient blockages, as discussed in Sec. 5.3.4, when the local geometry and cellular traffic conspire to slow flow in a confined apex region. Thus, understanding and predicting d_{ZF} in microvascular models requires accounting for RBC shape, but also for the repeated interactions that give rise to a persistent memory effect throughout multi-level bifurcations.

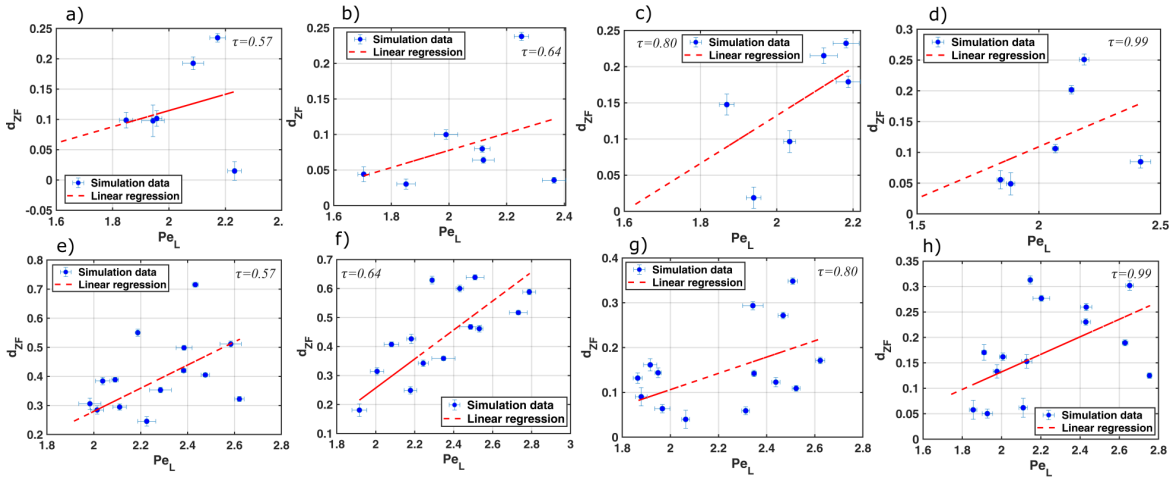

Fig. 5.8 Correlation between d_{ZF} and Pe_L for RBCs with various sphericities. Subfigures (a)–(d) display results for the asymmetric network, while (e)–(h) show results for the symmetric network.

5.3.6 Comparing Simulated RBC Partitioning to Pries' Law

Having investigated how RBC lingering and shape memory affect microcirculatory flow, we now compare our simulation data to the classical Pries law [93], which predicts the RBC flux fraction (N^*) as a function of the blood flow fraction (Q^*). Figure 5.9 shows N^* versus Q^* for various reduced areas (τ) and bifurcation levels in both the *asymmetric* (panel a) and *symmetric* (panel b) networks. The teal curve and shaded region indicate the Pries law prediction and its associated uncertainty, while the insets display boxplots of the deviation between simulation results and the model (i.e., $N^* - N^*_{\text{pred}}$) stratified by bifurcation level.

A. Overall Agreement and Deviations. At the first bifurcation level in both networks, RBC flux fractions generally cluster near the Pries law curve, indicating a relatively modest deviation ($< 5\%$) for most τ. However, with each subsequent bifurcation level, points increasingly deviate from the classical relationship, consistent

with the growing memory effects reported earlier (Sec. 5.3.5). By the third or fourth level, deviation can exceed 10%–15%, as seen in the insets' boxplots.

B. Influence of RBC Shape. Although larger deviations appear with every level, the degree of sphericity also plays a role. Elongated RBCs ($\tau \leq 0.64$) tend to lie slightly below the Pries law prediction at moderate Q^* values, suggesting stronger apex interactions that reduce net flux in one daughter vessel [66, 68]. Near-spherical RBCs ($\tau \geq 0.8$), on the other hand, show somewhat less deviation in early levels but eventually exhibit comparably high deviations at higher bifurcation levels, indicating that cumulative apex encounters (Sec. 5.3.3) overcome any initial geometric advantages.

C. Asymmetric vs. Symmetric Networks. In the *asymmetric* network [Fig. 5.9(a)], certain data points scatter further below the Pries law curve, reflecting local vessel-diameter variations and branching angles. The *symmetric* network [Fig. 5.9(b)] reduces such geometric biases up to level 3, yet the general trend of increasing deviation with increasing level persists, reinforcing that RBC history and apex lingering are the primary drivers of partitioning anomalies rather than geometry alone, where from the level 4 we see a huge deviation.

D. Implications. These results illustrate that while the Pries law provides a solid baseline for predicting RBC distribution, its accuracy diminishes at deeper bifurcations where RBC memory, lingering, and shape-dependent effects compound. As such, microcirculatory models that rely solely on classical partitioning laws may systematically underestimate RBC flux deviations in highly branched or pathological vessels. Incorporating RBC deformability, apex interactions, and multi-level memory effects (Sec. 5.3.3) is therefore crucial for accurate hemodynamic predictions in realistic networks.

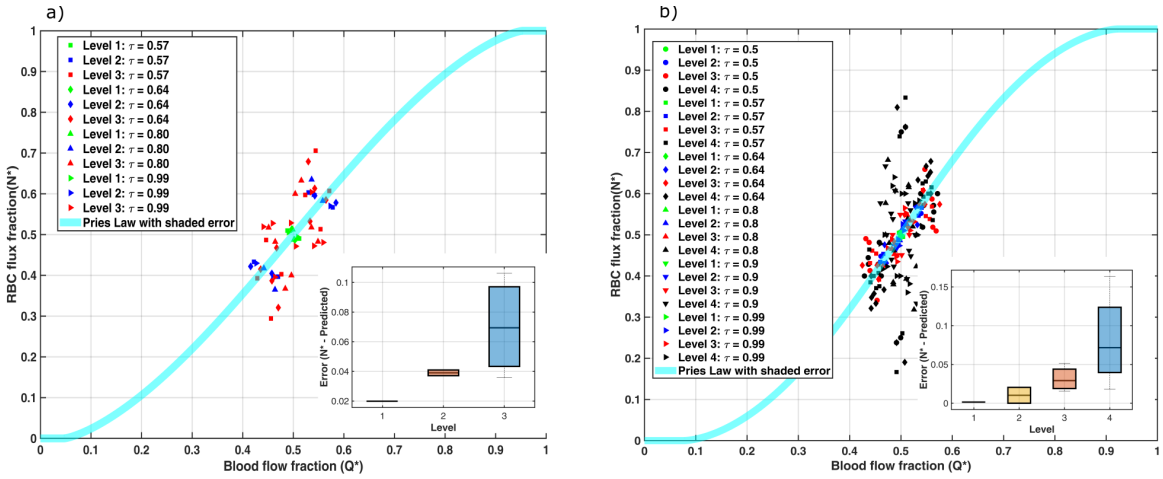

Fig. 5.9 Blood flow fraction vs. RBC flux fraction for various reduced areas across multiple bifurcation levels. Error bars plots indicate the deviation from the Pries model prediction. (a) Results for the asymmetric network; (b) results for the symmetric network.

5.4 Conclusion

In this work, we have numerically investigated how red blood cells (RBCs) distribute and linger across multiple bifurcations in microvascular networks, focusing on both asymmetric geometries (representative of real mesenteric vasculature) and artificially constructed symmetric networks. By combining a Lattice Boltzmann fluid solver with an immersed boundary approach for RBC membranes, we demonstrated the following key findings:

- **Memory Effect:** RBCs exhibit cumulative "memory" as they traverse successive bifurcation levels. Even when geometric asymmetry or vessel tapering is minimized, lingering and deviations from the Zweifach-Fung law grow significantly with each additional bifurcation. This highlights the primacy of RBC history—repeated apex interactions, radial drifts, and collective effects—in driving non-classical microcirculatory phenomena.

- **Lingering Across Shapes:** Although elongated (lower reduced area) RBCs tend to linger more strongly, spherical cells ($\tau \approx 0.99$) also experience substantial residence times when encountering tight apex geometries or multi-cell blockage events. Thus, membrane flexibility and local crowding—not just cell elongation—are critical to lingering behavior.

- **Partitioning Deviations:** Deviations from the classical Zweifach-Fung or Pries laws increase substantially over multiple bifurcations, suggesting that RBC "memory" can overwhelm simple flow-based models at deeper levels. Our results underscore that both local geometry and RBC shape must be accounted for to accurately predict RBC flux fractions in highly branched or pathological microvascular networks, and also the asymmetric flow at the bifurcation boosts these observations further because of the non-symmetric partitioning of RBCs.

- **Universality vs. Geometry:** While geometric features (vessel width, branching angle asymmetry) can amplify or moderate these effects, the fundamental trend of rising lingering and partitioning deviation persists even in perfectly symmetric designs. Consequently, RBC memory is a robust factor that can impact perfusion and oxygen delivery in capillary beds across various physiological and engineering contexts.

Collectively, these findings emphasize the importance of incorporating RBC deformability and memory effects when modeling microcirculatory flows. Future research

could address three-dimensional simulations and explore even more realistic vascular architectures (including Adhesion, dynamic vessel constriction or endothelium-mediated interactions) to further quantify and exploit RBC lingering and partitioning phenomena. In biomedical applications—such as tissue engineering, drug delivery, and artificial microfluidic systems—designs must acknowledge that RBCs do not simply follow the instantaneous flow field but instead bear the imprint of their prior encounters, thus impacting transport efficiency and potentially clinical outcomes.

Chapter 6

Hysteresis of a Single vesicle in a confined Poiseuille flow

Note: This work presents preliminary results.

6.1 Introduction

Vesicle dynamics in microfluidic flows are an active area of research interest relating to the understanding of cellular behaviour within the circulatory system and potential applications in biomedical engineering [29]. Among the most common vesicles in the bloodstream are RBCs. These particles undergo complex deformations and migration patterns when exposed to external flow fields. Because these dynamics are very important in the diagnosis and treatment of various blood disorders and in designing microfluidic devices efficiently for blood analysis and drug delivery [91], it is very important to understand. In this work, we concentrate on the dynamics of a single RBC in confined Poiseuille flow, which is driven by a pressure gradient between two parallel plates. It allows one to compensate for the effects of the capillary number, Ca, W and other RBC behavior-associated flow parameters. The capillary number, Ca, is a dimensionless number that captures the ratio between viscous forces and the elasticity of the membrane of the RBC. The channel width dictates confinement level of the RBC. Dynamics of vesicles in Poiseuille flows have been the topic of research before and large varieties of different behaviors were observed to be dependent on the flow parameters and the properties of the vesicle [47, 87]. For example, the deformability of vesicles into a number of different shapes like slippers, parachutes, and multi-lobed structures has been observed (Fig. 6.1). They also migrate far from the centerline of the channel under certain conditions [122]. However, a detailed understanding of

these mechanisms, which lie at the heart of such behaviors, remains elusive. In this work, with the help of numerical simulations and in a systematic manner, we study the dynamics of a single RBC in a confined Poiseuille flow. The study is conducted with the main objective of understanding the effects of Ca and W on the shape and position of the RBC and the related blood viscosity. In the simulations, we will look for a new bifurcation phenomenon distinguishing between stable and unstable RBC behavior. We also consider the role of the initial conditions and hysteresis in the dynamics of RBC and study relations of its position.

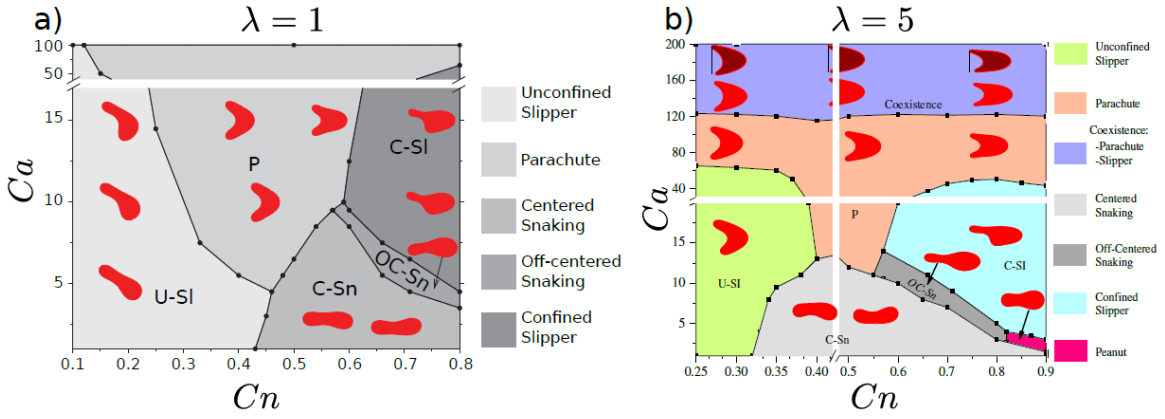

Fig. 6.1 (a) A phase diagram illustrating the stable shapes of vesicles in confined channel flow, depicting five distinguishable regions relative to the degree of confinement (Cn) and capillary number (Ca). Parameters are fixed at $\tau = 0.6$ and $\lambda = 1$. Image courtesy of [52]. (b) The corresponding phase diagram sourced from [112], utilizing identical parameters except for λ, which is set to 5. Image courtesy of [112].

6.2 Numerical inputs

Vesicle dynamics within this flow generally fall into the regime of Stokes flow, where viscous effects are much greater than inertial effects. This greatly simplifies the problem and allows for the capillary number to be a standard basis for comparison. For example, scientists working on vesicles in Poiseuille flow can use different channel widths, different vesicle diameters, or various bending moduli. Comparing the observations, the different studies show qualitative or quantitative agreement of those with the same capillary numbers [112, 52].

This characteristic of the capillary number is also leveraged in the nondimensionalization of numerical studies. In the investigation of red blood cells, with a diameter of approximately $3\mu m$, directly utilizing this value in simulations results in a very small floating-point number.

That, along with the restrictions of floating-point accuracy (usually 32 digits for single and 64 digits for double accuracy), introduces truncation errors in the calculations. The use of non-dimensionalized parameters, in this case, the cell diameter would be from 10 up to 20 lattices in our research; this greatly reduces the impact of the truncation errors.

For the present study, we will use the following inputs:

- Channel width: $W = 5\mu m$, $W = 10\mu m$, $W = 20\mu m$, $W = 30\mu m$ and $W = 45\mu m$
- Vesicle radius: $R = 3\mu m$
- Bending modulus: $\kappa = 3 \times 10^{-19}$ J
- Reduced area: $\tau = 0.65$
- Capillary number: from 5 to 300

The viscosity is set as $\mu = 0.001\, Pa \cdot s$, equivalent to saline or plasma, and for the cytosol, $\mu_{\text{cyt}} = 0.006\, Pa \cdot s$, resulting in a viscosity ratio of $\lambda = 6$. And simulations for the first case (Case 0) were initiated with a symmetric equilibrium shape, specifically the biconcave shape (In Fig. 2.3 for $\tau = 0.64$).

The normalized y position, denoted as Y, is calculated using the formula:

$$Y = \frac{y_{\text{c}}}{W} - 0.5$$

where y_{c} represents the mass center of the RBC, and the normalized upper wall is positioned at 0.5.

6.3 Single Cell Bifurcation

6.3.1 Width effect

The single-cell bifurcation in our study refers to the vesicle deviating from the channel center. Initially, the cell is symmetric, and its mass center is exactly at the channel center.

For the case of $W = 45\,\mu m$, we did not observe any bifurcation for capillary numbers below 73.24. The vesicle always flows in the center of the channel. However, when we increase Ca above 73.24 (even for $Ca = 70.23$, the cell maintains its movement close to the center), we observe a bifurcation to an unstable regime where the RBC moves away from the centerline and adopts random shapes (Fig. 6.2).

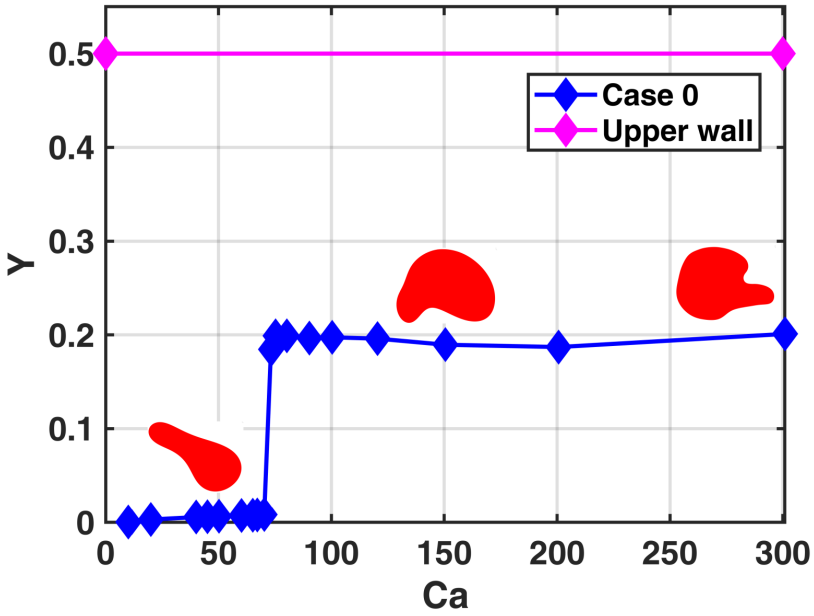

Fig. 6.2 Normalized Y position as a function of Ca, $W = 45\,\mu m$, $\lambda = 6$

We reduced the channel width from $W = 45\,\mu m$ to $W = 30\,\mu m$. These changes allow for some interesting insights into the behaviour of the vesicle.

Firstly, we observe in Fig.6.3 that slipper shapes appear at lower capillary numbers compared to parachute shapes. This suggests that a narrower channel facilitates the transition to slipper-shaped vesicles at reduced flow strengths, while the formation of parachute shapes requires higher capillary numbers.

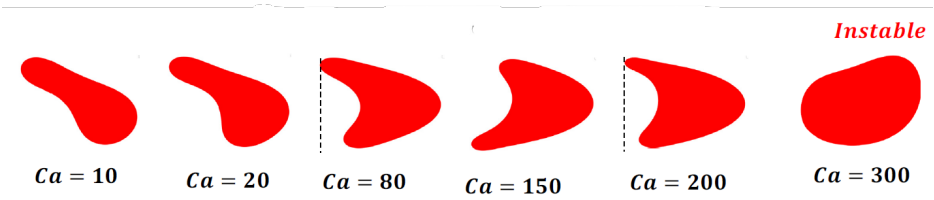

Fig. 6.3 RBC shape for different Ca and for $W = 30\,\mu m$

Secondly, in Fig. 6.4 we observe that the bifurcation behavior changes significantly with the reduced channel width. While previously, bifurcation was observed at $Ca = 73.24$ for a channel width of $45\,\mu m$, in the narrower channel of $30\,\mu m$, bifurcation occurs at a much higher capillary number of $Ca = 300$. This means that the vesicle stays in a centralized and stable position over a larger range of the flow strength in a small channel before transiting to the unstable regime.

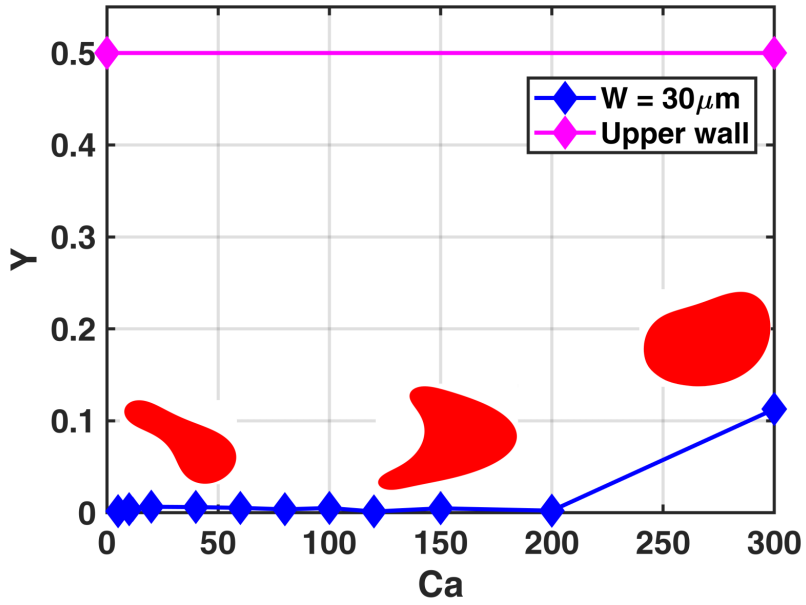

Fig. 6.4 Normalized Y position as a function of Ca, $W = 30\,\mu m$, $\lambda = 6$

The channel width for the $W = 20\mu m$ was also tested. This gave us a little more insight into the behavior of vesicles in even smaller channels.

For the channel width of $20\mu m$, no bifurcation happens (Fig. 6.5). All RBCs go and stay at the middle of the channel for the whole range of Ca that was applied. This shows that the vesicles still maintain their centered and stable position in narrower channels even with higher flow strengths. Previously, for a channel width of $45\mu m$ bifurcation was observed at $Ca = 73.24$, and for $30\mu m$, bifurcation occurred at $Ca = 300$. However, in further reduction of the width to $20\mu m$, RBCs remain unbifurcated for the entire range of Ca under study. Thus, narrow channels have a stabilizing effect on the vesicle, so it does not deviate from the centerline.

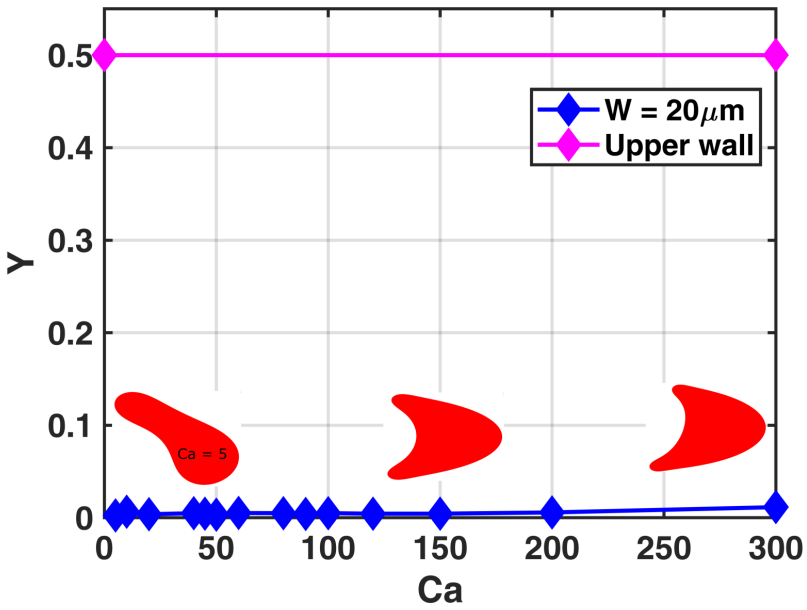

Fig. 6.5 Normalized Y position as a function of Ca, $W = 20\,\mu m$, $\lambda = 6$

We also examined narrower channel widths of $W = 10$ $(Fig.6.6), \mu m$ and $W = 5\,\mu m$ (Fig. 6.7), which provided further insights into the behavior of vesicles in highly confined channels.

For the channel width of $10\,\mu m$, there is no bifurcation observed. All shapes are parachute-like even at high capillary numbers (Fig. 6.6). An exception was found at $Ca = 5$, where the vesicles adopted a snicking shape. This indicates that in a 10-micron channel, the vesicles predominantly maintain parachute shapes across a wide range of capillary numbers, with only minor deviations at low Ca values.

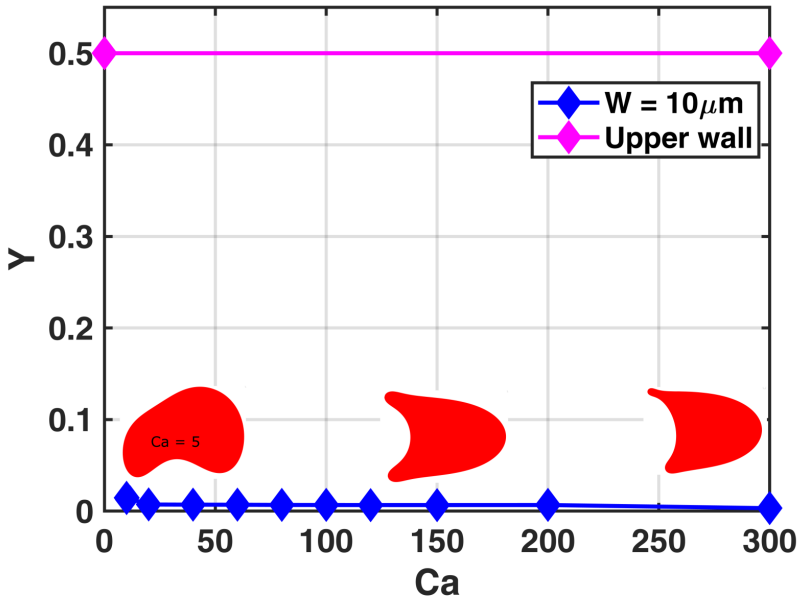

Fig. 6.6 Normalized Y position as a function of Ca, $W = 10\,\mu m$, $\lambda = 6$

For the very narrow channel width of $5\,\mu m$, we did not find any particular behaviors. The RBCs are significantly squeezed and adopt squeezed slipper shapes due to the extreme confinement.

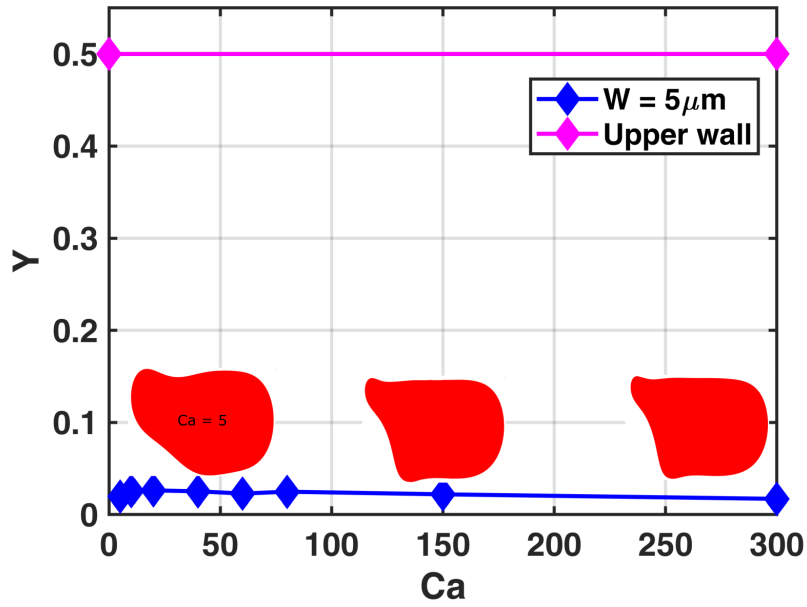

Fig. 6.7 Normalized Y position as a function of Ca, $W = 5\,\mu m$, $\lambda = 6$

To summarize the findings across all simulated widths, we plotted the normalized Y position as a function of Ca in Fig. 6.8. From this plot, we can observe that the

RBCs remained close to the centerline before bifurcation occurred in channels with widths of $45\,\mu m$ and $30\,\mu m$. This plot clearly demonstrates how varying the channel width can significantly influence the behavior of RBCs. In wider channels, RBCs exhibit bifurcation at certain Ca thresholds, whereas in narrower channels (10 microns and below), the RBCs maintain stable, centered positions and adopt specific shapes determined by the degree of confinement.

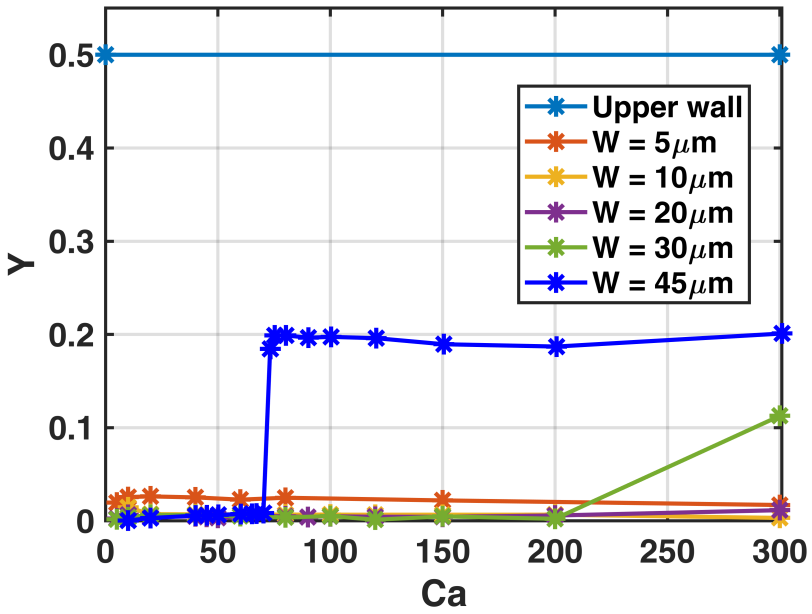

Fig. 6.8 Normalized Y position as a function of Ca for different channel widths, $\lambda = 6$

6.3.2 Rheology

The aim of the present study is to analyze the rheological properties of a suspension of a single RBC in a periodic channel with different levels of confinement, i.e., different channel widths. So we are mainly interested in calculating the effective viscosity for such a suspension.

To calculate the effective viscosity, we used formulas that relate the average flux of the vesicle suspension (2.12), the pure fluid, and the viscosity of the external fluid, which is $0.001\,\mathrm{Pa}\cdot\mathrm{s}$, the same as that of saline or plasma.

In the case of a channel width of $W = 45\,\mu m$, as previously seen, bifurcations occur after $Ca = 73$. This bifurcation has a notable impact which is reflected in the effective viscosity. In Figure 6.9, we observe a distinct jump in the effective viscosity after the bifurcation point. While the change is not dramatic, it is enough to be detected,

indicating that the presence of a single cell in the channel influences the rheological properties, although the hematocrit is very low (since there is only one cell in the channel), the change detected in effective viscosity may be attributed to the described sensitivity of rheological properties toward cellular dynamics.

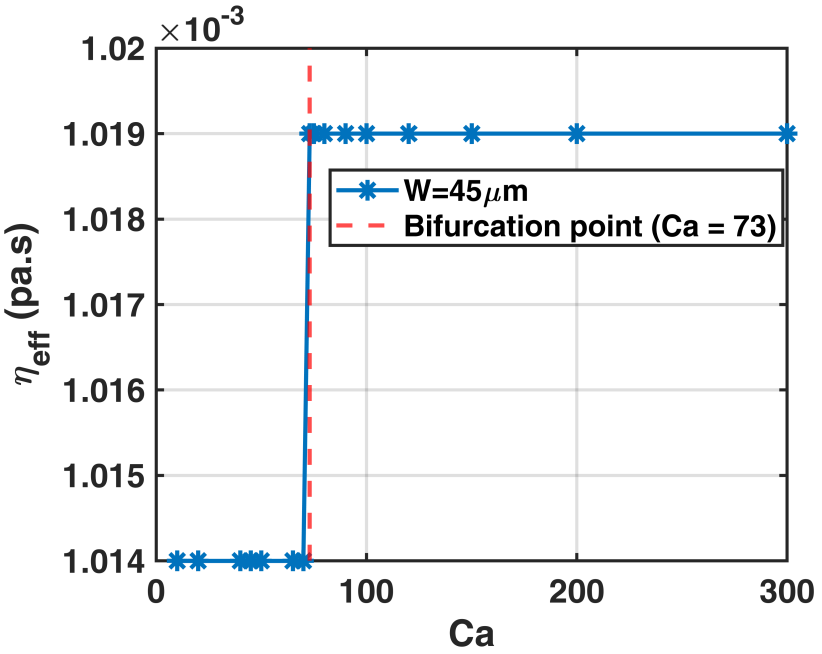

Fig. 6.9 Effective Viscosity as a function of Ca, $W = 45\,\mu m$, $\lambda = 6$

We show in Fig. 6.10 the normalized viscosity $\langle\eta\rangle$ as a function of the capillary number for different channel widths. The normalized viscosity is calculated using the formula:

$$\langle\eta\rangle = \frac{\eta_{\text{eff}} - \eta_{\text{out}}}{\eta_{\text{out}}}$$

where η_{eff} is the effective viscosity of the suspension and η_{out} is the viscosity of the external fluid, which is $0.001\,\text{Pa}\cdot\text{s}$ (same as saline or plasma).

The key observations from figure 6.10 are as follows:

1. Stability of Normalized Viscosity: The normalized viscosity $\langle\eta\rangle$ is fairly constant for all channel widths, with the exceptions of the two most narrow channels of $10, \mu m$ and $5, \mu m$. This implies that flow dynamics and, hence, effective viscosity do not vary significantly with varying capillary numbers for large channel widths unless a very low hematocrit is taken, except in case of a bifurcation to the unstable regime.

2. Effect of Channel Width on Normalized Viscosity: This is shown in the dependence of normalized viscosity on decreasing channel width. Such trend suggests that

the vesicle tends to experience stronger constraints within narrower channels, thus resulting in a higher effective viscosity. Finally, the higher viscosity for smaller channel widths is attributed to the higher concentration of hematocrit in a narrowed channel. It is well established that increasing hematocrit yields an increase in blood viscosity. In smaller channels, the relative volume of the RBC in space is larger, resulting in locally increased hematocrit and, consequently, higher viscosity.

3. Significant Increase in Very Narrow Channels: The increase in effective viscosity is by orders of magnitude for the very narrow channels. This sharp rise points out extreme confinement effects to which the RBCs are subjected: there is intense deformation and squeezing of RBC, leading to an increased resistance of flow.

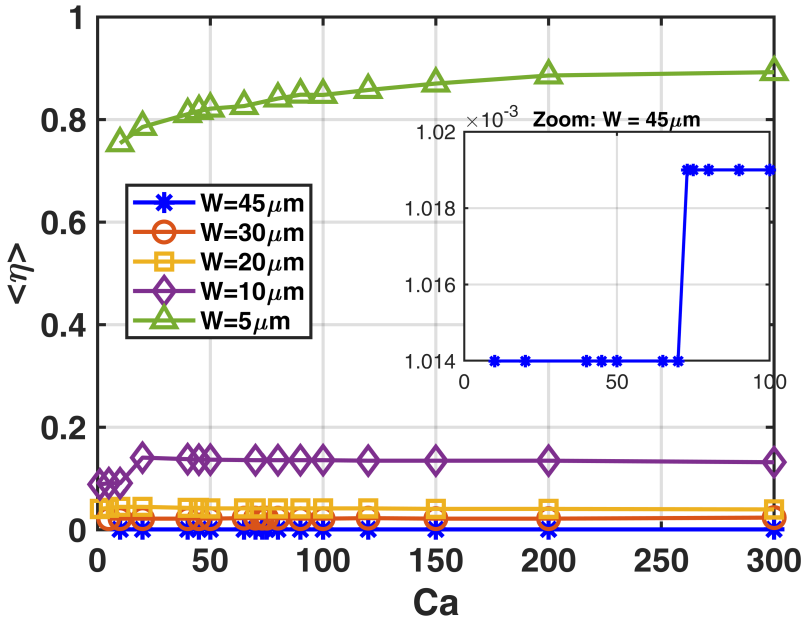

Fig. 6.10 Normalized Viscosity as a function of Ca for different channel widths, $\lambda = 6$

6.4 Hysteresis and RBCs

In this section, we fixed the channel width at $W = 45\,\mu m$ and investigated the presence of hysteresis in RBCs. To this end, we conducted simulations under two different initial conditions to observe whether previous bifurcation states would influence the behavior of the RBCs at Ca below the bifurcation threshold of 73.24.

Case 1: Bifurcated Asymmetric Shape Initialization: In the first case, we initiated the simulations using the bifurcated asymmetric shape obtained from the last

time iteration at $Ca = 73.24$. This means that instead of starting with the equilibrium shape (shape a in Fig. 6.11), we began with the bifurcated shape (shape b in Fig. 6.11). The RBC was placed in the bifurcated position ($y = 8.40\,\mu m$) as the initial position, as approximately shown in Figure 6.12.

Case 2: Centerline Initialization with Bifurcated Shape: In the second case, we again initialized the simulations with the bifurcated shape (shape b in Fig. 6.11), but this time, the RBC was positioned exactly on the centerline (Fig. 6.12).

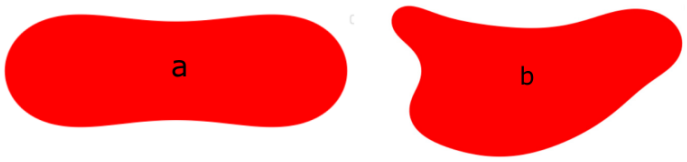

Fig. 6.11 a) Symmetric equilibrium shape (biconcave shape), b) Asymmetric shape taken from the bifurcated simulation

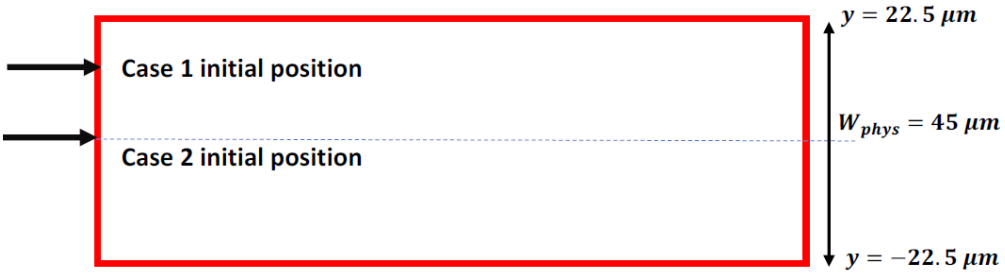

Fig. 6.12 Approximate initial position for case 1 and case 2

Simulation Procedure: After setting up the initial conditions for both cases, we restarted the simulations and observed the RBC behavior in the stable regime, specifically for capillary numbers below 73.24 (Before the RBC bifurcation). Our objective was to determine if the RBCs would exhibit bifurcation behavior due to the changes in their initial conditions.

Observations: In Case 1, we observed that the RBCs remained closely located in their bifurcation positions, as shown in Figure 6.13, with a very small turning toward the bifurcation position. This would indicate quite an important hysteresis behavior, where RBCs keep their non-centralized positions after reversing the reduction of capillary number below the bifurcation threshold. Specifically, we observed a clear pattern in

the shapes of RBCs: they remained stable—defined by the absence of random shape changes—when the capillary number remained under 45 (we also observed the trilobed shapes in this case which are shown in Fig. 6.14). Above this number, however, all RBCs of each subject became erratic in their shape transformation, suggesting the transition to an unstable regime governed by some fluid-flow dynamics of blood within a channel.

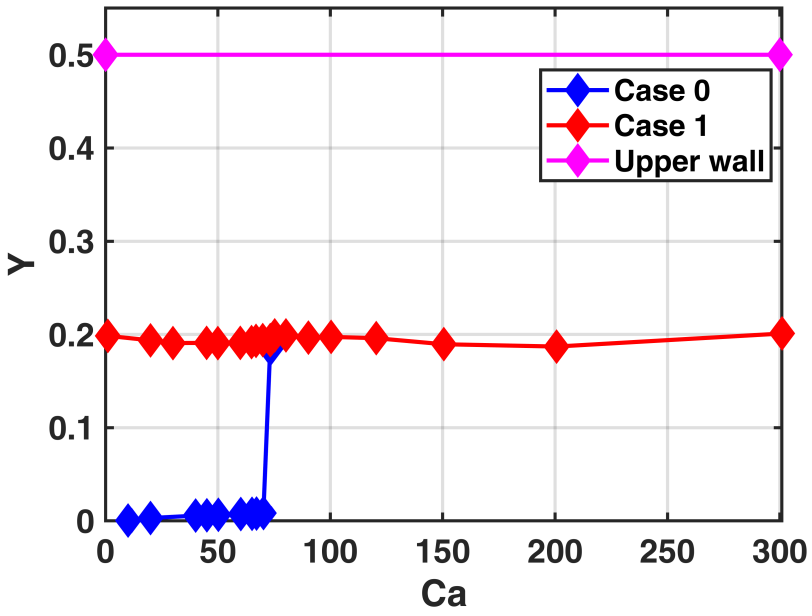

Fig. 6.13 The normalized Y position as a function of Capillary number, Blue line: Simulation without changes. Red line: Simulation of case 1.

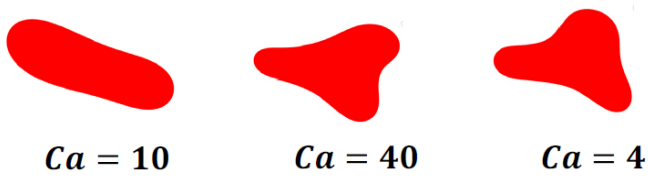

Fig. 6.14 RBCs shapes for different Capillary numbers in case 1

For Case 2, the simulations did return some interesting output. In spite of the initialization of asymmetric shapes, stabilization of the RBCs occurred as illustrated in Figure 6.15. The most important fact that can be derived from the result is that the initial shape of the RBCs does not significantly influence their final configuration. Instead, regardless of the initial asymmetry, the RBCs consistently have shapes closely aligned with the centerline.

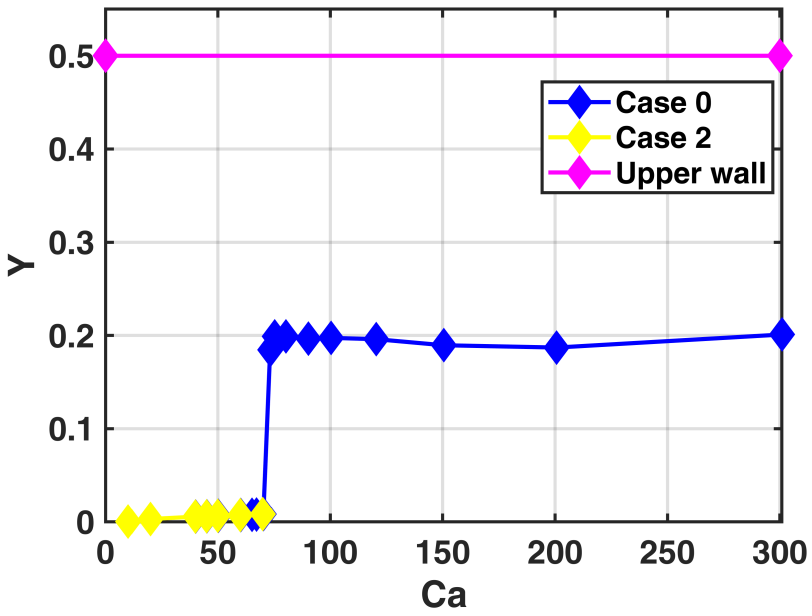

Fig. 6.15 The normalized Y position as a function of Capillary number, identical results between case 2 and case 0

6.5 Rigid cells Bifurcation

In our RBC behavior study at low Capillary Numbers, particularly below 5, we realized something quite interesting. Assuming a channel width of 45 µm constant, under different circumstances we conducted a series of simulations to see the dynamics in shape behavior of RBC.

In our methodology, we first positioned the RBC directly on the centerline of the microfluidic channel. Then, at each run of the simulation, the RBC was gradually offset from the central position by a distance of 0.015 microns, as shown in Figure 6.16). This slow movement was done very cautiously to study the very slight variations in RBC behavior while it is positioned off the centerline.

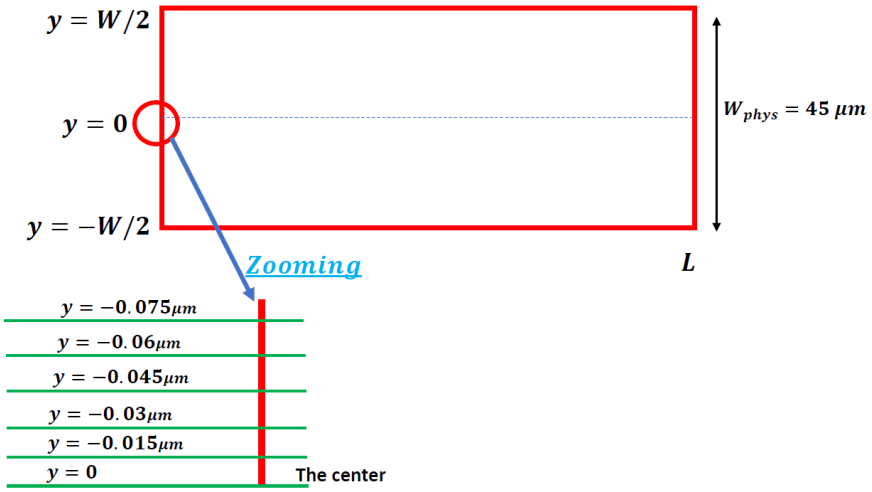

Fig. 6.16 Simulated positions for slight displacement

Our investigations have shown some very interesting phenomena with regard to the behavior of rigid RBCs for low capillary numbers, especially less than 5. The channel width is taken as 45 µm for all cases, and we further look into the response of RBCs towards the spatial heterogeneities within the microfluidic domain.

Initially, when the RBC was centered at the centerline, we observed that it remained centered (see Fig. 6.17). However, with the displacement of 0.015 µm from the centerline, the RBC could not come back and re-aligned at the centerline again (as shown in Fig. 6.18). Remarkably, this off-center behavior was consistently observed across all simulated cases, highlighting that this observation was not found at higher capillary numbers.

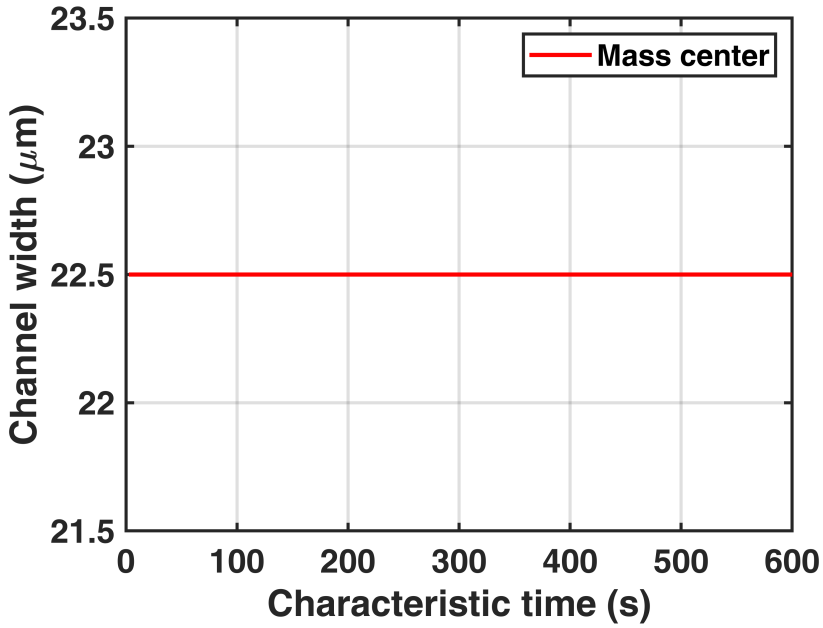

Fig. 6.17 Mass center position (in Lattice units) as a function of the characteristic time (s), the initial position in the centreline, Ca = 1

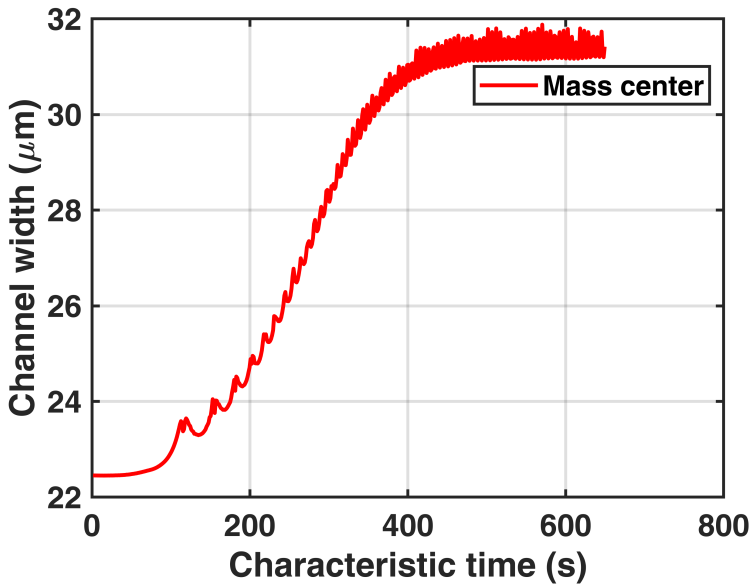

Fig. 6.18 Mass center position (in Lattice units) as a function of the characteristic time (s), the initial position with displacement of 0.015 microns from centreline, Ca = 1

The observation of RBCs exhibiting off-center behavior with minimal displacement from the centerline suggests the presence of a bifurcation phenomenon. Small deviation

of spatial positioning therefore produces a large effect on RBC behavior as it moves out of the stable central position it occupies. The result is very striking in the sense that it shows sensitivity of rigid RBCs to a small changes of their initial position, thereby indicative of a bifurcation event happening with truly small perturbations.

6.6 Conclusion

In this study, we have investigated the complex dynamics of a single RBC in confined Poiseuille flow through systematic numerical simulations. By varying key parameters such as the capillary number and channel width, we have demonstrated how confinement and flow strength influence the shape, migration behavior, and rheological properties of the RBC.

Our results reveal a bifurcation phenomenon that separates stable and unstable RBC dynamics, with the critical Ca for bifurcation strongly dependent on channel width. Wider channels promote off-center migration and shape instability at higher Ca, while narrower channels stabilize the RBC along the centerline and limit shape transitions. Additionally, we observed that extreme confinement leads to increased effective viscosity, highlighting the significant impact of RBC deformation on microfluidic flow resistance.

We also explored the role of initial conditions and hysteresis, showing that the final RBC position and shape are influenced by both the flow regime and prior states. At low Ca, even slight positional perturbations can lead to bifurcation-like behavior in otherwise rigid cells, indicating heightened sensitivity to initial symmetry-breaking.

Together, these findings advance our understanding of RBC behavior in microfluidic environments and have important implications for the design of lab-on-a-chip devices, biomedical diagnostics, and the study of blood rheology at the microscale.

Chapter 7

Conclusions and perspectives

7.1 Summary of Chapter 3 and related prospects

We investigated how sphericity of RBC affects the efficiency of microvascular flow. The computational analyses involving different cell shapes and their effect on the microfluidic system have been demonstrated and discussed. The study presented here has put special emphasis on the identification of the cell shape sensitivity; this is important because it shows that optimal flow efficiencies are different depending on channel dimensions. Future research is most likely going to incorporate three-dimensional modeling in order to capture more complex physiological scenarios and thus include biochemical cell properties in an attempt to further understand this interplay between RBC mechanics and endothelial cells.

7.2 Summary of Chapter 4 and related prospects

In this chapter, the dynamics of microvascular flow within suspensions of heterogeneously shaped red blood cells are analyzed. The study reveals significant alterations in flow patterns, flow rates, and effective blood viscosity, highlighting the sensitivity of blood flow to cellular composition. Additionally, the study aims to mimic the effects of spherocytosis by introducing a mixture of normal RBCs and spherical cells, which demonstrates a marked impact on both blood flow dynamics and viscosity. Future work may involve incorporating the biochemical signaling of RBCs through ATP in our simulations to examine how the heterogeneous suspension may affect such signaling with endothelial cells.

7.3 Summary of Chapter 5 and related prospects

This chapter explores how red blood cells distribute and linger across multiple bifurcations in microvascular networks, revealing that RBCs exhibit a cumulative "memory" effect that influences their partitioning beyond classical flow-based models. Using a Lattice Boltzmann fluid solver with an immersed boundary approach, the results show that lingering increases with successive bifurcations, even in symmetric geometries, and that both cell shape and local crowding play critical roles. Deviations from the Zweifach-Fung law grow deeper in the network, highlighting the necessity of incorporating RBC deformability and history in predictive models. These findings have implications for tissue engineering, drug delivery, and microfluidic designs, where RBC transport efficiency is crucial for optimizing perfusion and oxygen delivery.

7.4 Summary of Chapter 6 and related prospects

This study represents preliminary results that investigate the dynamics of a single RBC in confined Poiseuille flow. By examining how RBCs deform and migrate under different flow conditions, it aims to clarify the impact of key parameters, such as the capillary number, which relates viscous forces to membrane elasticity, and channel width. We analyze the shape, position, and viscosity of the RBC with the goal of identifying new bifurcation phenomena related to the deformation and shape of the cells.

7.5 Further perspectives

We are currently extending the studies presented in this thesis by including the adhesion between RBCs and their interaction with the vessel wall. Preliminary results from these ongoing analyses have shown a significant effect of the adhesion energy on the aggregation of RBC. This finding therefore opens new perspectives for the understanding of microcirculatory dynamics. We will also expand these studies to consider lingering effects with respect to ATP release from RBCs by taking into account the combined and isolated influences of RBC aggregation in different microvascular networks. This will deepen our understanding of biochemical and mechanical interactions within microcirculation.

References

[1] Abbasi, M., Farutin, A., Ez-Zahraouy, H., Benyoussef, A., and Misbah, C. (2021). Erythrocyte-erythrocyte aggregation dynamics under shear flow. *Physical Review Fluids*, 6(2):023602.

[2] Abkarian, M., Faivre, M., and Viallat, A. (2007). Swinging of red blood cells under shear flow. *Physical review letters*, 98(18):188302.

[3] Akrimi, J. A., Al-Jashamy, K., George, L. E., Suliman, A., and Ahmad, A. (2013). Frequency rate of abnormal morphologic shapes of the erythrocytes upon the different types of anemia. *Int J Scient & Eng Res*, 4(7):2476–2482.

[4] Alafzadeh, M., Yaghoubi, S., Shirani, E., and Rahmani, M. (2023). Simulation of rbc dynamics using combined low dimension, immersed boundary and lattice boltzmann methods. *Molecular simulation*, 49(12):1179–1184.

[5] Alberts, B. (2017). *Molecular biology of the cell*. Garland science.

[6] Altmayer, P. and Garrett, E. R. (1983). Plasmolysis, red blood cell partitioning, and plasma protein binding of etofibrate, clofibrate, and their degradation products. *Journal of pharmaceutical sciences*, 72(11):1309–1318.

[7] An, X. and Mohandas, N. (2011). Erythroblastic islands, terminal erythroid differentiation and reticulocyte maturation. *International journal of hematology*, 93:139–143.

[8] Bain, B. J. (2008). Irregularly contracted cells. *American journal of hematology*, 83(7):592–592.

[9] Balogh, P. and Bagchi, P. (2017). Direct numerical simulation of cellular-scale blood flow in 3d microvascular networks. *Biophysical journal*, 113(12):2815–2826.

[10] Balogh, P. and Bagchi, P. (2018). Analysis of red blood cell partitioning at bifurcations in simulated microvascular networks. *Physics of Fluids*, 30(5).

[11] Bendaoud, M., Abbasi, M., Darras, A., Ez-Zahraouy, H., Wagner, C., and Misbah, C. (2024a). Blood flow efficiency in response to red blood cell sphericity. *Phys. Rev. Fluids*, 9:053603.

[12] Bendaoud, M., Abbasi, M., Darras, A., Ez-Zahraouy, H., Wagner, C., and Misbah, C. (2024b). Blood flow efficiency in response to red blood cell sphericity. *Physical Review Fluids*, 9(5):053603.

[13] Bernabeu, M. O., Köry, J., Grogan, J. A., Markelc, B., Beardo, A., d'Avezac, M., Enjalbert, R., Kaeppler, J., Daly, N., Hetherington, J., et al. (2020). Abnormal morphology biases hematocrit distribution in tumor vasculature and contributes to heterogeneity in tissue oxygenation. *Proceedings of the National Academy of Sciences*, 117(45):27811–27819.

[14] Boyle, J. (1988). Microcirculatory hematocrit and blood flow. *Journal of Theoretical Biology*, 131(2):223–229.

[15] Bucciarelli, A., Mantegazza, A., Haeberlin, A., and Obrist, D. (2024). Relation between hematocrit partitioning and red blood cell lingering in a microfluidic network. *Biophysical journal*, 123(19):3355–3365.

[16] Casale, M. and Perrotta, S. (2011). Splenectomy for hereditary spherocytosis: complete, partial or not at all? *Expert review of hematology*, 4(6):627–635.

[17] Chen, S., Fu, B., Yuan, X., Zhang, H., Chen, W., and Yu, K. (2012). Lattice boltzmann method for simulation of solutal interfacial convection in gas–liquid system. *Industrial & engineering chemistry research*, 51(33):10955–10967.

[18] Chien, S. (1987). Red cell deformability and its relevance to blood flow. *Annual review of physiology*, 49(1):177–192.

[19] Cordasco, D. and Bagchi, P. (2017). On the shape memory of red blood cells. *Physics of Fluids*, 29(4):041901.

[20] Cordasco, D., Yazdani, A., and Bagchi, P. (2014). Comparison of erythrocyte dynamics in shear flow under different stress-free configurations. *Physics of Fluids*, 26(4):041902.

[21] Da Costa, L., Galimand, J., Fenneteau, O., and Mohandas, N. (2013). Hereditary spherocytosis, elliptocytosis, and other red cell membrane disorders. *Blood reviews*, 27(4):167–178.

[22] Da Costa, L., Galimand, J., Fenneteau, O., and Mohandas, N. (2013). Hereditary spherocytosis, elliptocytosis, and other red cell membrane disorders. *Blood Reviews*, 27(4):167–178.

[23] Dienstmann, G., Santos, V. B. d., and Comar, S. R. (2022). Mushroom-shaped red blood cells (pincer cells): a brief update. *Hematology, Transfusion and Cell Therapy*, 44:462–463.

[24] Farutin, A., Shen, Z., Prado, G., Audemar, V., Ez-Zahraouy, H., Benyoussef, A., Polack, B., Harting, J., Vlahovska, P. M., Podgorski, T., et al. (2018). Optimal cell transport in straight channels and networks. *Physical review fluids*, 3(10):103603.

[25] Fedosov, D. A., Caswell, B., and Karniadakis, G. E. (2010). A multiscale red blood cell model with accurate mechanics, rheology, and dynamics. *Biophysical journal*, 98(10):2215–2225.

[26] Fedosov, D. A., Peltomäki, M., and Gompper, G. (2014). Deformation and dynamics of red blood cells in flow through cylindrical microchannels. *Soft matter*, 10(24):4258–4267.

[27] Fischer, T. M. (2004). Shape memory of human red blood cells. *Biophysical journal*, 86(5):3304–3313.

[28] Fischer, T. M. (2022). The shape of human red blood cells suspended in autologous plasma and serum. *Cells*, 11(12):1941.

[29] Freund, J. B. (2014). Numerical simulation of flowing blood cells. *Annual review of fluid mechanics*, 46:67–95.

[30] Fung, Y. and Zweifach, B. (1971). Microcirculation: mechanics of blood flow in capillaries. *Annual Review of Fluid Mechanics*, 3(1):189–210.

[31] Gallagher, P. G. (2006). Red cell membrane abnormalities. *Pediatric Hematology*, pages 255–280.

[32] Gallagher, P. G. (2012). 164 - hemolytic anemias: Red cell membrane and metabolic defects. In Goldman, L. and Schafer, A. I., editors, *Goldman's Cecil Medicine (Twenty Fourth Edition)*, pages 1052–1060. W.B. Saunders, Philadelphia, twenty fourth edition edition.

[33] Gallagher, P. G. and Forget, B. G. (1998). Hematologically important mutations: spectrin and ankyrin variants in hereditary spherocytosis. *Blood Cells, Molecules, and Diseases*, 24(4):539–543.

[34] Geekiyanage, N. M., Balanant, M. A., Sauret, E., Saha, S., Flower, R., Lim, C. T., and Gu, Y. (2019). A coarse-grained red blood cell membrane model to study stomatocyte-discocyte-echinocyte morphologies. *PLoS One*, 14(4):e0215447.

[35] Gillian, P. and Christopher, D. (2003). Human physiology: the basis of medicine. *Oxford University Press, Oxford*, pages 286–287.

[36] Goodhead, L. K. and MacMillan, F. M. (2017). Measuring osmosis and hemolysis of red blood cells. *Advances in physiology education*, 41(2):298–305.

[37] Guckenberger, A., Kihm, A., John, T., Wagner, C., and Gekle, S. (2018). Numerical–experimental observation of shape bistability of red blood cells flowing in a microchannel. *Soft Matter*, 14(11):2032–2043.

[38] GW, M. (1966). Marsh.

[39] Hall, J. E. (2016). *Guyton and Hall Textbook of Medical Physiology, Jordanian Edition E-Book*. Elsevier Health Sciences.

[40] Halterman, J. S. and Segel, G. B. (2007). Spherocytosis. In Garfunkel, L. C., Kaczorowski, J. M., and Christy, C., editors, *Pediatric Clinical Advisor (Second Edition)*, page 534. Mosby, Philadelphia, second edition edition.

[41] Han, H., Rim, Y. A., and Ju, J. H. (2023). Recent updates of stem cell-based erythropoiesis. *Human Cell*, 36(3):894–907.

[42] Harvey, W. et al. (1928). Exercitatio anatomica de motu cordis et sanguinis in animalibus. *Frankfurt am Main*, 1628:17.

[43] Hebbel, R. P. (1991). Beyond hemoglobin polymerization: the red blood cell membrane and sickle disease pathophysiology.

[44] Helfrich, W. (1973). Elastic properties of lipid bilayers: theory and possible experiments. *Zeitschrift für Naturforschung c*, 28(11-12):693–703.

[45] Jung, H. H., Danek, A., and Walker, R. H. (2011). Neuroacanthocytosis syndromes. *Orphanet journal of rare diseases*, 6(1):1–9.

[46] Kabacaoğlu, G. and Biros, G. (2019). Sorting same-size red blood cells in deep deterministic lateral displacement devices. *Journal of Fluid Mechanics*, 859:433–475.

[47] Kaoui, B., Biros, G., and Misbah, C. (2009). Why do red blood cells have asymmetric shapes even in a symmetric flow? *Physical review letters*, 103(18):188101.

[48] Kaoui, B. and Harting, J. (2016). Two-dimensional lattice boltzmann simulations of vesicles with viscosity contrast. *Rheologica Acta*, 55(6):465–475.

[49] Kaoui, B., Harting, J., and Misbah, C. (2011a). Two-dimensional vesicle dynamics under shear flow: Effect of confinement. *Physical Review E*, 83(6):066319.

[50] Kaoui, B., Jonk, R. J., and Harting, J. (2014). Interplay between microdynamics and macrorheology in vesicle suspensions. *Soft Matter*, 10(26):4735–4742.

[51] Kaoui, B., Ristow, G. H., Cantat, I., Misbah, C., and Zimmermann, W. (2008). Lateral migration of a two-dimensional vesicle in unbounded poiseuille flow. *Phys. Rev. E*, 77:021903.

[52] Kaoui, B., Tahiri, N., Biben, T., Ez-Zahraouy, H., Benyoussef, A., Biros, G., and Misbah, C. (2011b). Complexity of vesicle microcirculation. *Physical Review E*, 84(4):041906.

[53] Keller, S. R. and Skalak, R. (1982). Motion of a tank-treading ellipsoidal particle in a shear flow. *Journal of Fluid Mechanics*, 120:27–47.

[54] Kessler, S., Finken, R., and Seifert, U. (2009). Elastic capsules in shear flow: Analytical solutions for constant and time-dependent shear rates. *The European Physical Journal E*, 29:399–413.

[55] Khairy, K., Foo, J., and Howard, J. (2008). Shapes of red blood cells: comparison of 3d confocal images with the bilayer-couple model. *Cellular and molecular bioengineering*, 1:173–181.

[56] Khan, I. A., Daya, S. K., and Gowda, R. M. (2005). Evolution of the theory of circulation. *International Journal of Cardiology*, 98(3):519–521.

[57] Kihm, A., Quint, S., Laschke, M. W., Menger, M. D., John, T., Kaestner, L., and Wagner, C. (2021). Lingering dynamics in microvascular blood flow. *Biophysical journal*, 120(3):432–439.

[58] Kim, S., Ong, P. K., Yalcin, O., Intaglietta, M., and Johnson, P. C. (2009). The cell-free layer in microvascular blood flow. *Biorheology*, 46(3):181–189.

[59] Klei, T. R., Meinderts, S. M., van den Berg, T. K., and van Bruggen, R. (2017). From the cradle to the grave: the role of macrophages in erythropoiesis and erythrophagocytosis. *Frontiers in immunology*, 8:73.

[60] Koga, T., ENGINEERING, P. I. O. B. N. D. O. A., and HANICS, A. M. (1966). *The Bhatnagar-Gross-Krook Equation as an Approximation of the Boltzmann Equation*. Polytechnic Institute of Brooklyn, Department of Aerospace Engineering and ....

[61] Krüger, T., Frijters, S., Günther, F., Kaoui, B., and Harting, J. (2013a). Numerical simulations of complex fluid-fluid interface dynamics. *The European Physical Journal Special Topics*, 222(1):177–198.

[62] Krüger, T., Gross, M., Raabe, D., and Varnik, F. (2013b). Crossover from tumbling to tank-treading-like motion in dense simulated suspensions of red blood cells. *Soft Matter*, 9(37):9008–9015.

[63] Krüger, T., Kusumaatmaja, H., Kuzmin, A., Shardt, O., Silva, G., and Viggen, E. M. (2017). The lattice boltzmann method, graduate texts in physics.

[64] Krüger, T., Varnik, F., and Raabe, D. (2011). Efficient and accurate simulations of deformable particles immersed in a fluid using a combined immersed boundary lattice boltzmann finite element method. *Computers & Mathematics with Applications*, 61(12):3485–3505.

[65] Krüger, T., Varnik, F., and Raabe, D. (2011). Efficient and accurate simulations of deformable particles immersed in a fluid using a combined immersed boundary lattice boltzmann finite element method. *Computers & Mathematics with Applications*, 61(12):3485–3505. Mesoscopic Methods for Engineering and Science — Proceedings of ICMMES-09.

[66] Kumar, A. and Graham, M. D. (2012). Mechanism of margination in confined flows of blood and other multicomponent suspensions. *Physical review letters*, 109(10):108102.

[67] Kumar, A., Rivera, R. G. H., and Graham, M. D. (2014). Flow-induced segregation in confined multicomponent suspensions: effects of particle size and rigidity. *Journal of Fluid Mechanics*, 738:423–462.

[68] Lanotte, L., Mauer, J., Mendez, S., Fedosov, D. A., Fromental, J.-M., Claveria, V., Nicoud, F., Gompper, G., and Abkarian, M. (2016). Red cells' dynamic morphologies govern blood shear thinning under microcirculatory flow conditions. *Proceedings of the National Academy of Sciences*, 113(47):13289–13294.

[69] Lesesve, J. F., Garçon, L., and Lecompte, T. (2012). Finding knizocytes in a peripheral blood smear. *American journal of hematology*, 87(1):105–106.

[70] Li, G., Ye, T., Xia, Z., Wang, S., and Zhu, Z. (2023). Analysis and prediction of hematocrit in microvascular networks. *International Journal of Engineering Science*, 191:103901.

[71] Li, J., Huang, Z., Xu, Y., Zhou, H., Han, F., Gong, S., and Wan, S. (2005). Compound heterozygote factor and clinical significance of hemolysis system analysis in the diagnosis of congenital hemolytic anemia: Etiological analysis of 506 cases of anemia and jaundice. *J Clin Hematol*, 18(4):204–6.

[72] Li, L., Mei, R., and Klausner, J. F. (2017). Lattice boltzmann models for the convection-diffusion equation: D2q5 vs d2q9. *International Journal of Heat and Mass Transfer*, 108:41–62.

[73] Lichtman, A. H. (2009). *Basic immunology: functions and disorders of the immune system*. Saunders/Elsevier.

[74] Lipowsky, H. H., Usami, S., and Chien, S. (1980). In vivo measurements of "apparent viscosity" and microvessel hematocrit in the mesentery of the cat. *Microvascular Research*, 19(3):297–319.

[75] Liu, Y., Zheng, J., Song, L., Fang, Y., Sun, C., Li, N., Liu, G., and Shu, J. (2020). A novel sptb gene mutation in neonatal hereditary spherocytosis: A case report. *Experimental and Therapeutic Medicine*, 20(4):3253–3259.

[76] Lux IV, S. E. (2016). Anatomy of the red cell membrane skeleton: unanswered questions. *Blood, The Journal of the American Society of Hematology*, 127(2):187–199.

[77] Malpighi, M. (1661). *De Pulmonibus*. Ex Typographia Haeredis Victorii Benatii, Bonn.

[78] Mantegazza, A., Ungari, M., Clavica, F., and Obrist, D. (2020). Local vs. global blood flow modulation in artificial microvascular networks: effects on red blood cell distribution and partitioning. *Frontiers in physiology*, 11:566273.

[79] Marieb, E. N. and Hoehn, K. (2007). *Human anatomy & physiology*. Pearson education.

[80] Mauer, J., Mendez, S., Lanotte, L., Nicoud, F., Abkarian, M., Gompper, G., and Fedosov, D. A. (2018). Flow-induced transitions of red blood cell shapes under shear. *Physical review letters*, 121(11):118103.

[81] Mchedlishvili, G. (1998). Disturbed blood flow structuring as critical factor of hemorheological disorders in microcirculation. *Clinical hemorheology and microcirculation*, 19(4):315–325.

[82] Mendez, S. and Abkarian, M. (2019). Single red blood cell dynamics in shear flow and its role in hemorheology. In *Dynamics of Blood Cell Suspensions in Microflows*, pages 125–182. CRC Press.

[83] Misbah, C. (2006). Vacillating breathing and tumbling of vesicles under shear flow. *Physical review letters*, 96(2):028104.

[84] Mohandas, N. and Gallagher, P. G. (2008). Red cell membrane: past, present, and future. *Blood, The Journal of the American Society of Hematology*, 112(10):3939–3948.

[85] Mokken, F. C., Kedaria, M., Henny, C. P., Hardeman, M., and Gelb, A. (1992). The clinical importance of erythrocyte deformability, a hemorrheological parameter. *Annals of hematology*, 64:113–122.

[86] Nait-Ouhra, A., Guckenberger, A., Farutin, A., Ez-Zahraouy, H., Benyoussef, A., Gekle, S., and Misbah, C. (2018). Lateral vesicle migration in a bounded shear flow: Viscosity contrast leads to off-centered solutions. *Physical review fluids*, 3(12):123601.

[87] Noguchi, H. and Gompper, G. (2005). Shape transitions of fluid vesicles and red blood cells in capillary flows. *Proceedings of the National Academy of Sciences*, 102(40):14159–14164.

[88] Nouaman, M., Darras, A., John, T., Simionato, G., Rab, M. A., van Wijk, R., Laschke, M. W., Kaestner, L., Wagner, C., and Recktenwald, S. M. (2023). Effect of cell age and membrane rigidity on red blood cell shape in capillary flow. *Cells*, 12(11):1529.

[89] Peng, Z., Pak, O. S., Feng, Z., Liu, A. P., and Young, Y.-N. (2016). On the gating of mechanosensitive channels by fluid shear stress. *Acta Mechanica Sinica*, 32:1012–1022.

[90] Peskin, C. S. (1972). Flow patterns around heart valves: a numerical method. *Journal of computational physics*, 10(2):252–271.

[91] Peskin, C. S. (2002). The immersed boundary method. *Acta numerica*, 11:479–517.

[92] Popel, A. S. and Johnson, P. C. (2005). Microcirculation and hemorheology. *Annu. Rev. Fluid Mech.*, 37:43–69.

[93] Pries, A., Ley, K., Claassen, M., and Gaehtgens, P. (1989). Red cell distribution at microvascular bifurcations. *Microvascular research*, 38(1):81–101.

[94] Pries, A. R. and Secomb, T. W. (2008). Blood flow in microvascular networks. In *Microcirculation*, pages 3–36. Elsevier.

[95] Quint, S., Christ, A., Guckenberger, A., Himbert, S., Kaestner, L., Gekle, S., and Wagner, C. (2017). 3d tomography of cells in micro-channels. *Applied Physics Letters*, 111(10):103701.

[96] Rashidi, Y., Aouane, O., Darras, A., John, T., Harting, J., Wagner, C., and Recktenwald, S. M. (2023a). Cell-free layer development and spatial organization of healthy and rigid red blood cells in a microfluidic bifurcation. *Soft Matter*, 19(33):6255–6266.

[97] Rashidi, Y., Simionato, G., Zhou, Q., John, T., Kihm, A., Bendaoud, M., Krüger, T., Bernabeu, M. O., Kaestner, L., Laschke, M. W., et al. (2023b). Red blood cell lingering modulates hematocrit distribution in the microcirculation. *Biophysical Journal*, 122(8):1526–1537.

[98] Reasor Jr, D. A., Clausen, J. R., and Aidun, C. K. (2012). Coupling the lattice-boltzmann and spectrin-link methods for the direct numerical simulation of cellular blood flow. *International Journal for Numerical Methods in Fluids*, 68(6):767–781.

[99] Recktenwald, S. M., Graessel, K., Maurer, F. M., John, T., Gekle, S., and Wagner, C. (2022). Red blood cell shape transitions and dynamics in time-dependent capillary flows. *Biophysical Journal*, 121(1):23–36.

[100] Recktenwald, S. M., Graessel, K., Rashidi, Y., Steuer, J. N., John, T., Gekle, S., and Wagner, C. (2023). Cell-free layer of red blood cells in a constricted microfluidic channel under steady and time-dependent flow conditions. *arXiv preprint arXiv:2304.02919*.

[101] Robier, C., Klescher, D., Reicht, G., Amouzadeh-Ghadikolai, O., Quehenberger, F., and Neubauer, M. (2015). Dacryocytes are a common morphologic feature of autoimmune and microangiopathic haemolytic anaemia. *Clinical Chemistry and Laboratory Medicine (CCLM)*, 53(7):1073–1076.

[102] Sankaran, V. G. and Weiss, M. J. (2015). Anemia: progress in molecular mechanisms and therapies. *Nature medicine*, 21(3):221–230.

[103] Schapkaitz, E. and Mezgebe, M. H. (2017). The clinical significance of schistocytes: a prospective evaluation of the international council for standardization in hematology schistocyte guidelines. *Turkish Journal of Hematology*, 34(1):59.

[104] Secomb, T. W. (2017). Blood flow in the microcirculation. *Annual Review of Fluid Mechanics*, 49:443–461.

[105] Seifert, U. (1999). Fluid membranes in hydrodynamic flow fields: Formalism and an application to fluctuating quasispherical vesicles in shear flow. *The European Physical Journal B-Condensed Matter and Complex Systems*, 8:405–415.

[106] Shen, Z., Coupier, G., Kaoui, B., Polack, B., Harting, J., Misbah, C., and Podgorski, T. (2016). Inversion of hematocrit partition at microfluidic bifurcations. *Microvascular research*, 105:40–46.

[107] Shen, Z., Farutin, A., Thiébaud, M., and Misbah, C. (2017). Interaction and rheology of vesicle suspensions in confined shear flow. *Physical Review Fluids*, 2(10):103101.

[108] Sills, M. R. and Zinkham, W. H. (1994). Methylene blue–induced heinz body hemolytic anemia. *Archives of pediatrics & adolescent medicine*, 148(3):306–310.

[109] Sofroniew, M. V. (2024). Astrocyte cells in the brain have immune memory.

[110] Sotiropoulos, F., Aidun, C., Borazjani, I., and MacMeccan, R. (2011). Computational techniques for biological fluids: from blood vessel scale to blood cells. *Image-Based Computational Modeling of the Human Circulatory and Pulmonary Systems: Methods and Applications*, pages 105–155.

[111] Succi, S. (2001). *The lattice Boltzmann equation: for fluid dynamics and beyond*. Oxford university press.

[112] Tahiri, N., Biben, T., Ez-Zahraouy, H., Benyoussef, A., and Misbah, C. (2013). On the problem of slipper shapes of red blood cells in the microvasculature. *Microvascular research*, 85:40–45.

[113] Takeishi, N., Rosti, M. E., Imai, Y., Wada, S., and Brandt, L. (2019). Haemorheology in dilute, semi-dilute and dense suspensions of red blood cells. *Journal of Fluid Mechanics*, 872:818–848.

[114] Thiébaud, M. and Misbah, C. (2013). Rheology of a vesicle suspension with finite concentration: A numerical study. *Physical Review E*, 88(6):062707.

[115] Thiébaud, M., Shen, Z., Harting, J., and Misbah, C. (2014). Prediction of anomalous blood viscosity in confined shear flow. *Phys. Rev. Lett.*, 112:238304.

[116] Timm, K., Kusumaatmaja, H., Kuzmin, A., Shardt, O., Silva, G., and Viggen, E. (2016). The lattice boltzmann method: principles and practice. *Cham, Switzerland: Springer International Publishing AG*.

[117] Tomaiuolo, G. (2014). Biomechanical properties of red blood cells in health and disease towards microfluidics. *Biomicrofluidics*, 8(5):051501.

[118] Van Leeuwenhoek, A. (1722). *Opera Omnia, Seu Arcana Naturae: Ope Exactissimorum Microscoporum Detecta, experimentis variis comprobata, Epistolis, Ad varios illustris Viros, Ut Et Ad integram,... datis, Comprehensa, & Quatour Tomis distincta. Antonii A Leeuwenhoek, Regiae Societatis Anglicanae Socii, Arcana Naturae Detecta*, volume 3. Langerak.

[119] Veerapaneni, S. K., Young, Y.-N., Vlahovska, P. M., and Bławzdziewicz, J. (2011). Dynamics of a compound vesicle in shear flow. *Physical review letters*, 106(15):158103.

[120] Yawata, Y., Kanzaki, A., Yawata, A., Doerfler, W., Ozcan, R., and Eber, S. (2000). Characteristic features of the genotype and phenotype of hereditary spherocytosis in the japanese population. *International journal of hematology*, 71(2):118–135.

[121] Zhang, H., Shen, Z., Hogan, B., Barakat, A. I., and Misbah, C. (2018). Atp release by red blood cells under flow: model and simulations. *Biophysical journal*, 115(11):2218–2229.

[122] Zhao, H. and Shaqfeh, E. S. (2011). The dynamics of a vesicle in simple shear flow. *Journal of Fluid Mechanics*, 674:578–604.